

Copyright  
by  
Kevin Richard Jackman  
2007

**The Dissertation Committee for Kevin Richard Jackman Certifies that this is the approved version of the following dissertation:**

**KMESS: An Open Source Software Package Using a Semi-empirical  
Mesh-Grid Method for the Modeling of Germanium Detector  
Efficiencies**

**Committee:**

---

Steven Biegalski, Supervisor

---

Sheldon Landsberger

---

Malcolm Fowler

---

John Howell

---

Erich Schneider

**KMESS: An Open Source Software Package Using a Semi-empirical  
Mesh-Grid Method for the Modeling of Germanium Detector  
Efficiencies**

**by**

**Kevin Richard Jackman, M.S. B.S. B.A.**

**Dissertation**

Presented to the Faculty of the Graduate School of

The University of Texas at Austin

in Partial Fulfillment

of the Requirements

for the Degree of

**Doctor of Philosophy**

**The University of Texas at Austin**

**August, 2007**

## **Dedication**

I dedicate this document to my parents, John and Linda Jackman, for their uncompromised love and support throughout my life.

## **Acknowledgements**

I would like to thank my supervisor, Steven Biegalski, for his guidance and wisdom, without whom, this research would not have been possible. I would like to thank Sheldon Landsberger for taking me under his wing and sparking my interest in gamma-ray spectroscopy. I would also like to thank Malcolm Fowler and Russ Gritzko for always being there to answer my questions and to point me in the right direction. Also, many thanks to Joe Artnak for his amazing help with meshing software. Funding for this research was provided by a collaborative agreement between Los Alamos National Laboratory and The University of Texas at Austin.

# **KMESS: An Open Source Software Package Using a Semi-empirical Mesh-Grid Method for the Modeling of Germanium Detector Efficiencies**

Publication No. \_\_\_\_\_

Kevin Richard Jackman, Ph.D.

The University of Texas at Austin, 2007

Supervisor: Steven Biegalski

Traditional approaches in gamma-ray spectroscopy for determining the absolute full-energy peak efficiencies of germanium detectors are primarily either too time consuming or not economically viable. In addition, these approaches are difficult to use for arbitrary source shapes and counting geometries. An open source software package, KMESS (Kevin's Mesh Efficiency Simulator Software), was developed to address these problems. KMESS uses a new semi-empirical mesh-grid method to predict the absolute full-energy peak efficiencies of *n*- and *p*-type germanium detectors in both coaxial and closed-ended configurations. The model assumes that any gamma-ray source shape can be treated as a collection of point sources. The code was written in a modular form, making it easy to adapt for other detector configurations and materials. A suite of web-based graphical front-end tools was also developed to make the execution of KMESS user-friendly. KMESS can predict most full-energy peak efficiencies to within 10% accuracy for the energy range 100–1800 keV in less than 10 minutes.

## Table of Contents

List of Tables .....	x
List of Figures .....	xiv
List of Figures .....	xiv
<b>AN OPEN SOURCE SOFTWARE PACKAGE FOR THE MODELING OF GERMANIUM DETECTOR EFFICIENCIES .....</b>	<b>1</b>
Chapter 1: Introduction .....	1
1.1 Introduction.....	1
1.2 Gamma-ray Detection.....	2
1.2.1 History of Gamma-rays.....	2
1.2.2 History of Gamma-ray Detectors.....	2
1.3 Kevin’s Mesh Efficiency Simulator Software (KMESS) Package.....	3
1.3.1 Code Justification.....	3
1.3.2 Brief Description of KMESS.....	4
Chapter 2: Background .....	6
2.1 History of Gamma-ray Detector Efficiency Calculations.....	6
2.1.1 Introduction.....	6
2.1.2 History.....	7
2.2 Traditional Methods to Calculate Detector Efficiencies.....	9
2.2.1 Relative Method.....	9
2.2.2 Monte Carlo Method.....	10
2.2.3 Semi-empirical Method .....	11
2.3 Computer Codes.....	12
2.3.1 Introduction to Computer Codes.....	12
2.3.2 Monte Carlo Method Codes.....	12
2.3.3 Semi-empirical Method Codes .....	13
Chapter 3: Theory .....	17
3.1 Gamma-ray Interactions.....	17

3.1.1	Introduction to Gamma-ray Interactions.....	17
3.1.2	Photoelectric Absorption .....	19
3.1.3	Compton Scattering .....	19
3.1.4	Pair Production.....	20
3.1.5	Rayleigh Scattering.....	20
3.2	Germanium Detectors .....	21
3.2.1	Semiconductors.....	21
3.2.2	Detector Characteristics .....	24
3.2.3	Detector Use and Corrections .....	26
3.3	Traditional and Moens Efficiency Calculations .....	27
3.3.1	Traditional Method .....	27
3.3.1.1	Remarks on the “Efficiency” .....	27
3.3.1.2	Traditional Geometric Solid Angle.....	29
3.3.2	Moens Method .....	31
3.3.2.1	Moens Geometric Solid Angle.....	31
3.3.2.2	Effective Solid Angle.....	34
3.4	Mesh-grid Method Efficiency Calculations.....	40
3.4.1	Assumptions.....	40
3.4.2	Mathematical Form.....	41
3.4.3	Additional Derivations.....	50
3.4.4	Uncertainties .....	58
3.5	Monte Carlo .....	61
Chapter 4:	KMESS Code Description .....	63
4.1	KMESS Code Format .....	63
4.1.1	Overview of the Code .....	63
4.1.2	Code Defaults and Limitations .....	66
4.2	KMESS Features.....	67
4.2.1	Currently Included .....	67
4.2.2	Future Additions .....	68



Chapter 5: Results and Discussion.....	70
5.1 Validation of Model Assumptions.....	70
5.1.1 Invariance of Virtual Peak-to-Total Ratio .....	70
5.1.2 Detector Approximated as a Cylinder.....	75
5.1.3 Coaxial Hole Considerations .....	81
5.1.4 Weighting Factors and Homogeneity .....	82
5.2 Validation of Code Calculations.....	82
5.2.1 KMESS vs. Experimental .....	82
5.2.2 KMESS vs. Other Codes.....	92
5.2.3 Grid Sensitivity Tests.....	99
Chapter 6: Conclusions.....	103
Appendix.....	105
A.1 Additional KMESS Documentation.....	105
A.1.1 KMESS README FILE.....	105
A.1.2 KMESS Absorber File (KAF) README.....	108
A.1.3 KMESS Cross-section File (KCF) README.....	112
A.1.4 KMESS Detector File (KDF) README.....	116
A.1.5 KMESS Reference File (KRF) REAME .....	125
A.1.6 KMESS Source File (KSF) README.....	126
A.2 Procedure For Using KMESS to Determine Efficiencies.....	131
A.2.1 Determination of an Experimental Reference Curve.....	131
A.2.2 Setting up and Running KMESS .....	133
References.....	135

Vita 140

## List of Tables

Table 5.1: Results of Peak-to-Total Ratio Simulations for a Source-to-Detector Distance of 0 cm for Three Different Angular Source Placements. ....	71
Table 5.2: Results of Peak-to-Total Ratio Simulations for a Source-to-Detector Distance of 5 cm for Three Different Angular Source Placements. ....	72
Table 5.3: Results of Peak-to-Total Ratio Simulations for a Source-to-Detector Distance of 10 cm for Three Different Angular Source Placements. ....	72
Table 5.4: Variation of Peak-to-Total Ratio Simulations for Three Fixed Angular Source Placements and Source-to-Detector Distances Varying as 0, 5, and 10 cm. ....	73
Table 5.5: Experimentally Measured Peak-to-Total Ratios for On-axis Sources at Distances of 0, 1, 4, and 10 cm. ....	75
Table 5.6: Percent Differences Between the Cylinder and Bullet MCNP5 Models at Source-to-Detector Distances of 0, 1, 2, and 3 inches. ....	79
Table 5.7: Percent Differences Between the Cylinder and Bullet MCNP5 Models at Source-to-Detector Distances of 4, 5, 6, and 12 inches. ....	79
Table 5.8: Shelf Height Distances (in cm) for Point Source and Vial Source Counting Geometries for Counter 76. ....	83
Table 5.9: Experimentally Measured Efficiencies and KMESS Effective Solid Angle Calculated Efficiencies for a Point Source on Shelf 1 of Counter 76. ....	84
Table 5.10: Experimentally Measured Efficiencies and KMESS Effective Solid Angle Calculated Efficiencies for a Point Source on Shelf 2 of Counter 76. ....	85

Table 5.11: Experimentally Measured Efficiencies and KMESS Effective Solid Angle Calculated Efficiencies for a Point Source on Shelf 5 of Counter 76.....	85
Table 5.12: Experimentally Measured Efficiencies and KMESS Effective Solid Angle Calculated Efficiencies for a Point Source on Shelf 12 of Counter 76.....	86
Table 5.13: Experimentally Measured Efficiencies and KMESS Effective Solid Angle Calculated Efficiencies for a Point Source on Shelf 22 of Counter 76.....	86
Table 5.14: Experimentally Measured Efficiencies and KMESS Effective Solid Angle Calculated Efficiencies for a Vial Source on Shelf 1 of Counter 76.....	88
Table 5.15: Experimentally Measured Efficiencies and KMESS Effective Solid Angle Calculated Efficiencies for a Vial Source on Shelf 5 of Counter 76.....	88
Table 5.16: Experimentally Measured Efficiencies and KMESS Effective Solid Angle Calculated Efficiencies for a Vial Source on Shelf 12 of Counter 76.....	89
Table 5.17: Experimentally Measured Efficiencies and KMESS Effective Solid Angle Calculated Efficiencies for a Vial Source on Shelf 13 of Counter 76.....	89
Table 5.18: Experimentally Measured Efficiencies and KMESS Effective Solid Angle Calculated Efficiencies for a Vial Source on Shelf 22 of Counter 76.....	90

Table 5.19: Experimentally Measured Efficiencies and KMESS Effective Solid Angle Calculated Efficiencies for a Vial Source on Shelf 1 of Counter 76 Using a Point Source on Shelf 10 as the Reference Curve.....	91
Table 5.20: Experimentally Measured Efficiencies and KMESS Effective Solid Angle Calculated Efficiencies for a Vial Source on Shelf 22 of Counter 76 Using a Point Source on Shelf 10 as the Reference Curve.....	91
Table 5.21: Experimentally Measured, SYNTH, and EFFIC Efficiencies for a Point Source on Shelf 1 of Counter 76.....	93
Table 5.22: Experimentally Measured, SYNTH, and EFFIC Efficiencies for a Point Source on Shelf 2 of Counter 76.....	93
Table 5.23: Experimentally Measured, SYNTH, and EFFIC Efficiencies for a Point Source on Shelf 5 of Counter 76.....	94
Table 5.24: Experimentally Measured, SYNTH, and EFFIC Efficiencies for a Point Source on Shelf 12 of Counter 76.....	94
Table 5.25: Experimentally Measured, SYNTH, and EFFIC Efficiencies for a Point Source on Shelf 22 of Counter 76.....	95
Table 5.26: Experimentally Measured, SYNTH, and EFFIC Efficiencies for a Vial Source on Shelf 1 of Counter 76.....	96
Table 5.27: Experimentally Measured, SYNTH, and EFFIC Efficiencies for a Vial Source on Shelf 5 of Counter 76.....	96
Table 5.28: Experimentally Measured, SYNTH, and EFFIC Efficiencies for a Vial Source on Shelf 12 of Counter 76.....	97
Table 5.29: Experimentally Measured, SYNTH, and EFFIC Efficiencies for a Vial Source on Shelf 13 of Counter 76.....	97

Table 5.30: Experimentally Measured, SYNTH, and EFFIC Efficiencies for a Vial  
Source on Shelf 22 of Counter 76.....98

## List of Figures

Figure 3.1: Total Linear Attenuation Coefficient for Germanium and Processes that Contribute to it as a Function of Gamma-ray Energy (Berger <i>et al.</i> , 2007). .....	18
Figure 3.2: Three Common Coaxial Detector Designs and the Placement of Contact Layers (Knoll, 2000). .....	25
Figure 3.3: Graphical Representation of Cartesian Coordinate System Established for Geometrical Solid Angle Calculations When Source is Located Above the Detector. ....	32
Figure 3.4: Paths <i>a</i> Through <i>h</i> Show Possible Paths to be Followed by a Photon Impinging upon the Detector Top Surface (Moens <i>et al.</i> , 1981). ....	39
Figure 3.5: Paths <i>i</i> Through <i>l</i> Show the Four Additional Possible Paths to be Followed by a Photon Impinging Upon the Detector Side Surface (modified from Moens <i>et al.</i> , 1981). ....	42
Figure 3.6: Graphical Representation of Cartesian Coordinate System Established for Geometrical Solid Angle Calculations When Source to the Side of the Detector. ....	43
Figure 3.7: Photons From a Point Within a Source <i>T</i> , as Shown, Can Interact With the Detector Top Surface at Points Like <i>P</i> or the Side Surface at Points Like <i>P'</i> . ....	46
Figure 3.8: Attenuation of Gamma-rays Following Path <i>TP</i> Through Absorbing Materials Above the Detector Surface. ....	51
Figure 3.9: Attenuation of Gamma-rays with a Fluence, $I_0$ , Passing Through Three Different Materials. ....	54

Figure 4.1: Flow Chart for KMESS Code Execution. ....	64
Figure 4.2: How KMESS Fits Into the Current NGWeb Analysis System. ....	65
Figure 5.1: Picture of MCNP5 Model with the Detector Crystal and Coaxial Hole Approximated as Cylinders.....	77
Figure 5.2: Picture of MCNP5 Model that Includes the Detector Crystal and Coaxial Hole Bulletization. ....	78
Figure 5.3: Average Effective Solid Angle, as a Function of the Number of Points on the Line, for Two Line Sources Pointing in the $X$ -direction.....	100
Figure 5.4: Average Effective Solid Angle, as a Function of the Number of Points on the Line, for Four Line Sources Pointing in the $Z$ -direction.....	101
Figure 5.5: Average Effective Solid Angle, as a Function of the Number of Points in the $R$ and $\theta$ Directions, for a Disc Source.....	102

# **AN OPEN SOURCE SOFTWARE PACKAGE FOR THE MODELING OF GERMANIUM DETECTOR EFFICIENCIES**

## **Chapter 1: Introduction**

### **1.1 INTRODUCTION**

The discovery of radioactivity by Henri Becquerel in 1896 revolutionized the fields of physics and chemistry, and forever changed the world in which we live. His discovery invoked the basic human desire to understand the fundamental nature of the universe by delving deeper into the structure of the atom. The study of radioactivity was essential in showing the world the benefits of nuclear power and the horrors of nuclear weapons. It has also led to the ability to treat certain cancers, sterilize food, and control insect populations. Even the social and political climates of society have been shaped by its discovery, ranging from the Cold War to the current nuclear situations with Iran and North Korea. There is no doubt that the study of radioactivity will continue to amaze and revolutionize generations to come.

The desire to quantify the amount of radioactivity in a substance has led to the invention of various forms of radiation detectors. A study is performed here on the efficiencies of one type of radiation detector, namely the germanium detector. Furthermore, the result of this study has been to produce an open source software package that can quickly and accurately predict the efficiencies of germanium detectors.



## **1.2 GAMMA-RAY DETECTION**

### **1.2.1 History of Gamma-rays**

Radioactivity is the process in which an unstable atomic nucleus releases energy, or decays, in order to reach a more stable nuclear configuration. The energy released by the nucleus during its decay is typically in the form of either particles or electromagnetic waves. One possible product of radioactive decay is a gamma-ray, a form of electromagnetic radiation. Gamma-rays are the most energetic class, highest frequency and shortest wavelength, of the electromagnetic spectrum.

Paul Ulrich Villard is generally regarded as the discoverer of the gamma-ray, and also as the one who coined the name (Debertin *et al.*, 1988). Villard discovered them in Paris in 1900 while noticing that rays emanating from Uranium were not deflected by a magnetic field (Debertin *et al.*, 1988). Gamma-rays were soon realized, like X-rays, to be electromagnetic waves. For a long time there was no distinction between X-rays and gamma-rays, primarily because they were both electromagnetic radiations that interacted in matter similarly. The distinction was eventually made that gamma-rays were a characteristic of nuclear decay, whereas X-rays were the result of electrons changing their orbital shells (Friedlander and Kennedy, 1957).

### **1.2.2 History of Gamma-ray Detectors**

In order to quantify the radioactivity of a substance using a detector, one needs to know the efficiency of that detector. The efficiency is a measure of how many decay events are observed by the detector relative to the number of decay events produced by a sample. If the radioactive source happens to give off a non-trivial quantity of gamma-rays, a gamma-ray detector is often employed to measure its radioactivity. Early forms of

gamma-ray detectors were either gas chambers or sodium-iodide (NaI) crystals. In the 1960's, the first semiconductor gamma-ray detectors became commercially available (Knoll, 2000). Semiconductor detectors soon became widely used because of their superior energy resolution. The primary semiconductor materials used in these detectors were either germanium or silicon. Germanium became the preferred choice for gamma-ray spectroscopy because, having a higher atomic number, it yielded higher efficiencies for a given crystal size (Knoll, 2000). Germanium was also easier to manufacture in a pure form. Silicon detectors are still used, but primarily for X-ray spectroscopy. Since that time, the manufacturing processes of germanium detectors have changed, but their basic functionality remains the same.

### **1.3 KEVIN'S MESH EFFICIENCY SIMULATOR SOFTWARE (KMESS) PACKAGE**

#### **1.3.1 Code Justification**

Knowledge of the absolute detector efficiency is necessary for radioactivity determination and helps with nuclide identification. Traditional approaches to find the absolute efficiency of germanium detectors are primarily either overtly time consuming or not economically viable. The Chemistry division's Nuclear and Radiochemistry group (C-NR) at Los Alamos National Laboratory currently has a counting room that employs a large number of germanium detectors (~40), routine source shapes (~10), and available counting geometries (~20). The amount of time and cost to experimentally calibrate the efficiencies for all the possible combinations of detectors, source types, and counting geometries is significant. These measurements would also only be valid for the source shape and counting geometry used in the calibration. Therefore, the ability to predict

efficiencies, to within a fair degree of accuracy, <10% but not >20%, for any detector, source shape, and counting geometry in a timely manner, ~minutes, was needed.

A new semi-empirical mesh-grid method that quickly (~minutes) and accurately (~10%) models the absolute full-energy peak efficiencies (FEPE) of germanium detectors for arbitrary gamma-ray source shapes and counting geometries was developed to address this need. An open source software package, called KMESS (Kevin's Mesh Efficiency Simulator Software), was written that utilizes this method. The current version of the code is being prepared for open source distribution under the GNU (GNU's Not Unix) Public License (GPL). A suite of user-friendly web-based tools to control and execute KMESS was also developed. There is no software package currently available, either commercially or open source, that performs as diverse, quick, and accurate calculations of germanium detector efficiencies.

### **1.3.2 Brief Description of KMESS**

KMESS is a software package written in the C language to predict the full-energy peak efficiencies of *n*- and *p*-type germanium detectors in both true and closed-ended coaxial configurations. The base KMESS code was written in C in order to achieve fast computational times and to provide easy debugging for future users. It uses a new semi-empirical mesh-grid method to predict the full-energy peak efficiencies of arbitrary gamma-ray source shapes and counting geometries. The mesh-grid method is based on the effective solid angle concept, and needs only one experimentally measured reference efficiency curve to predict the efficiencies of other counting geometries. The primary assumption of the method is that any gamma-ray source shape can be approximated as a collection of point sources. The source is input into KMESS as a mesh of points, thus making the code handle arbitrary gamma-ray source shapes.

The base KMESS code is run from the command line and controlled with arguments and flags. KMESS was designed to be modular, meaning that it can be easily altered to run in different ways. This allows future users to easily modify the code and change the way that KMESS makes calculations. For instance, the code could be adapted to handle well or planar detector configurations. Compiling and building KMESS is done using the GNU Make tools, so that running it on different platforms is straightforward.

A suite of web-based graphical front-end tools, written in a combination of the PHP (PHP: Hypertext Preprocessor) and JavaScript programming languages, were also developed to facilitate a more user-friendly interaction with KMESS. The programming languages for the front-end were chosen so that KMESS could be easily incorporated into the current counting room software. For more information regarding the code design and usage, see Chapter 4 or the README files included in Appendix A.1.

## **Chapter 2: Background**

### **2.1 HISTORY OF GAMMA-RAY DETECTOR EFFICIENCY CALCULATIONS**

#### **2.1.1 Introduction**

Semiconductor detectors, primarily high-purity germanium, have become an industry standard for gamma-ray spectroscopy. These detectors allow one to study gamma-rays in the energy range from a few keV up to several MeV. When used properly, the detectors produce pulses whose amplitudes are proportional to the energy deposited by incident gamma-rays. If these pulses are binned based on amplitude using a multi-channel analyzer, an energy spectrum is produced. Typically encountered spectra have a continuum rich in features and peaks. The individual peaks appear to have a shape like a typical normal distribution, or a normal distribution with an exponential tail. As seen in the spectra, each peak corresponds to a specific photon energy. If the peak is at the same energy as a known gamma-ray, then the area under this peak is called the area under the full-energy peak.

The determination of the activity of a sample from the observed area under a full-energy peak requires knowledge of the detector's absolute full-energy peak efficiency. A comparative standard is typically used to determine this efficiency because it depends upon both photon energy and counting geometry. Thus, for non-standard counting geometries and sample shapes, it is often difficult to obtain the absolute full-energy peak efficiency experimentally, computationally, or even theoretically. Therefore, many assumptions and approximations must often be made. The word "efficiency" from henceforth is used to imply absolute efficiency at a specific energy, rather than relative efficiency, unless otherwise noted.

All of the traditional approaches to determine the absolute full-energy peak efficiencies of a gamma-ray detector can be categorized into one of three methods. The three traditional methods are called relative, Monte Carlo, and semi-empirical. These methods are described further in Section 2.2.

### 2.1.2 History

The available work on gamma-ray detector efficiencies dates back to the early 1950's. The Mathematics Panel at Oak Ridge National Laboratory initially computed a simple equation describing the total detection efficiency of NaI detectors, as a function of geometry and interaction probability (Kahn, 1953). The extensions to total detection efficiency of a point, line, and disk sources were calculated analytically at the Idaho Operations Office of the Atomic Energy Commission (Vegors *et al.*, 1958; Heath, 1957).

Eventually these integrals were extended to planar Ge(Li) detectors and intrinsic Ge detectors for both point and disk shaped sources (Grosjean *et al.*, 1962; Heath, 1964; Graduynya *et al.*, 1971; Kaplanis, 1978). Total efficiencies for large coaxial Ge(Li) detectors, both closed and open, were found for point sources with respect to point sources on the detector primary axis (Camp *et al.*, 1969; Griffiths, 1971). These landmark papers on cylindrical radiation detector efficiencies were, however restricted only to finding the total detector efficiency. To convert to absolute full-energy peak efficiency, one needs the so-called peak-to-total ratio at the energy of interest (Vegors *et al.*, 1958). Some of the older literature strongly suggested using Monte Carlo methods to find the absolute full-energy peak detector efficiency (Griffiths, 1971; Waino *et al.*, 1966).

Other methods were developed to find the absolute full-energy peak efficiency of coaxial Ge(Li) detectors for points, disks, cylinders, and spheres, but were based on

approximations that represent the detector and source as physical points (Cline, 1979; Gunnink, 1972). This is called the single point-to-point detector or the effective interaction depth model (Gunnink, 1972). The model reduces the detector volume to an equivalent point, where all gamma-ray interactions are considered to occur. Several other people have studied the point-to-point detector model experimentally and computationally to measure the effective interaction depth in germanium detectors (Yucel *et al.*, 1996; Notea, 1971; Crisler *et al.*, 1971; Cline, 1979; Baba *et al.*, 1991). A modern form of this method was developed that uses primarily the manufacturers' detector specifications to predict absolute full-energy peak efficiencies to within a few percent (Gunnink, 1990; Gunnink *et al.*, 1992).

A method of calculating the absolute full-energy peak efficiency that treats bulk sources as a collection of point sources was developed (Kushelevski *et al.*, 1975). This method demonstrated that displacing a point source off the detector's primary axis caused the detection efficiency to decrease. Furthermore, as the source was displaced, the efficiency dropped off like a Gaussian distribution whose width depended upon the energy of the gamma-ray and the height of the source above the detector (Kushelevski *et al.*, 1975; Chatani, 1999; Noguchi *et al.*, 1980). Another group showed how to correct this method for source self-absorption (Noguchi *et al.*, 1980). In addition, another group showed that a volumetric source inside a NaI well detector could be modeled as a collection of disc sources (Cejnar *et al.*, 1979). However, all of these groups fit their model to rigorously obtained experimental data from calibrated sources in order to reconstruct their volumetric efficiencies. All of the models appear to be only valid for points with a displacement from the detector's primary axis less than the radius of the detector. It was also important for this method to use single-line emitting gamma-ray sources in order to reduce coincidence-summing effects.

In the early 1980's, a new method was suggested to find the absolute full-energy peak detector efficiency, using the concept of the effective solid angle (Moens *et al.*, 1981). Afterwards, a few highly successful codes utilizing this “Moens” method were developed, but then quickly disappeared (Ugletveit *et al.*, 1989; Vukotic *et al.*, 1997; Jovanovic *et al.*, 1997). Hybrid Moens methods using Monte Carlo integration, rather than typical numerical integration, were also investigated (Jiang *et al.*, 1998; Vidmar, 2005). It was found that the hybrid Monte Carlo method gives results that are the same as numerical integration, but that Monte Carlo integration facilitates calculations when the source is placed off-axis (Jiang *et al.*, 1998). However, much of the current literature is still preoccupied with using Monte Carlo methods to produce absolute full-energy peak efficiencies (Jackman, 2004; Hurtado *et al.*, 2004; Ewa *et al.*, 2001; Rodenas *et al.*, 2003; Karamanis, 2003).

## **2.2 TRADITIONAL METHODS TO CALCULATE DETECTOR EFFICIENCIES**

### **2.2.1 Relative Method**

The relative method is where one tries “to imitate as well as possible” the sample with a comparative standard (Jovanovic *et al.*, 1997). For this method to be sufficiently accurate, the standard must be similar to the sample in both geometry and composition, and the counting conditions must be the same for both samples. If “enough care” is taken, the results of this method are often sufficiently accurate that they cannot be surpassed by any other method (Jovanovic *et al.*, 1997). However, the lack of “similar enough” standards, combined with the difficulty of varying counting and source geometries, restricts this method to special circumstances.



### 2.2.2 Monte Carlo Method

Calculations using a stochastic, or Monte Carlo, method may be employed to yield absolute full-energy peak efficiencies for any arbitrary sample shape and counting conditions. This method statistically models the interactions of each photon emitted from the source, until the photon either leaves the “world” or deposits all of its energy within the active detector volume (Jovanovic *et al.*, 1997; Jackman, 2004). It must also contain a treatment of all secondarily produced electrons, positrons, and photons. Because it is a statistical method, the primary errors that arise are themselves statistical in nature (Jackman, 2004). For this method to be exact, one needs to model a sufficiently large number of source particles, know precise details about the compositions of detector and intercepting layers, their corresponding energy dependent cross sections, and parameters characterizing electron, positron, and photon behavior in the model (Jovanovic *et al.*, 1997).

The primary limiting factors to this method are the temporal requirements of computation necessary for a “sufficiently large” number of source photons, unsatisfactory knowledge of detector specifications, lack of understanding of the exact physics, and poor knowledge of other physical parameters aforementioned (Jovanovic *et al.*, 1997; Jackman, 2004). One Monte Carlo study revealed that a few millimeter variations in fundamental detector parameters like detector diameter, end cap distance, and well diameter can produce large variations, ~15%, in simulated full-energy peak efficiencies (Vargas *et al.*, 2002). At present, the accuracy of this method is difficult to reduce much below 10% because of the uncertainties in these detector parameters (Jackman, 2004). In addition, the amount of computation time necessary to yield good statistics using a code such as MCNP is on the order of days for a modern desktop PC (Jackman, 2004).

### 2.2.3 Semi-empirical Method

A semi-empirical method can be employed that uses a combination of experimental measurements and theoretical detector response. This is typically done using an experimentally measured reference efficiency curve where, relative to this, calculations of the desired efficiencies can be made (Moens *et al.*, 1981; Jovanovic *et al.*, 1997; Gunnink *et al.*, 1992). There are many different treatments of the semi-empirical method, but only the simultaneous treatment of photon attenuation, geometry, and detector response is justified (Moens *et al.*, 1981). The two primary methods that have arisen are called the effective interaction depth and effective solid angle methods.

The effective interaction depth method defines the efficiency as the product of terms that describe photon attenuation, geometry, and detector response (Gunnink *et al.*, 1992). It makes the assumption that all of the gamma-ray interactions occur at a single point in the detector. Efficiency curves are created from semi-empirical functions describing three different regions of the photon energy spectrum. These functions were generated from fitting data across a wide range of detector sizes and manufacturers' specifications (Gunnink, 1990; Gunnink *et al.*, 1992).

The effective solid angle method analytically calculates, using vector calculus, a mathematical integral that simultaneously treats photon attenuation, geometry, and detector response. The computation time in this method is trivial, because it is primarily limited only by how fast one can numerically integrate. The accuracy is often better than that obtained with the stochastic method (Ugletveit *et al.*, 1989; Jovanovic *et al.*, 1997; Ewa *et al.*, 2001).

One limitation to the current semi-empirical methods is that they have only been solved for simple source shapes, such as the point, disk, cylindrical, and Marinelli geometries. The Marinelli geometry is a large plastic beaker with an annular bottom that

slips over the detector. Another limitation is that uncertainties in the experimentally measured reference efficiency curves permeate throughout subsequent calculations. However, because the semi-empirical methods calculate the absolute full-energy peak efficiency using a reference curve, they should be less sensitive than Monte Carlo methods to the uncertainties in fundamental detector parameters.

## **2.3 COMPUTER CODES**

### **2.3.1 Introduction to Computer Codes**

Computer codes to perform absolute full-energy peak efficiency calculations have been developed many times over. Most typical gamma-ray analysis codes have a feature to perform relative method efficiency calibrations. Thus, more attention will be paid here to the codes that utilize Monte Carlo and semi-empirical methods.

### **2.3.2 Monte Carlo Method Codes**

The industry standard Monte Carlo based codes are MCNP and GEANT. Both of these codes were originally coded in FORTRAN. Since then, GEANT has been ported to C++ and a version of MCNP is currently being ported to the C language (Hurtado *et al.*, 2004). Both codes are difficult to use, install, and setup for different sample shapes and counting geometries. In addition, modeling of exotic source shapes is very difficult in both codes. Furthermore, MCNP and GEANT both lack proper handling of important low-energy gamma-ray physics. In fact, MCNP has been shown to do a poor job of modeling low-energy gamma-ray source self absorption (Venkataraman *et al.*, 2005). Also, the low-energy GEANT extension libraries correct Compton cross-sections for bound electron momentum, but do not account for resulting changes in the scattered

particle energies (Kippen, 2004). In addition, the low-energy GEANT extension libraries have errors in the treatment of Rayleigh scattering (Kippen, 2004).

One group has developed a new Monte Carlo based code called GESPECOR specifically for absolute full-energy peak efficiency calculations (Sima *et al.*, 2001). Though the code has a nice graphical front-end, the restrictions that GESPECOR is only Monte Carlo based, and only a WINDOWS based program are inherent downsides. Another group developed their own Monte Carlo code called DETEFF (Cornejo Diaz *et al.*, 1998). This code tracks only photons that deposit all of their energy in the detector, and contribute to full-energy peaks. It also neglects Bremsstrahlung from secondary electrons. As a result, the calculations are only good for photons less than 2 MeV (Cornejo Diaz *et al.*, 1998). On the commercial market, Canberra has its LABSOCS/ISOCS software which is relatively inexpensive. However, Canberra must characterize the detector in order to use LABSOCS/ISOCS, which is an expensive process. LABSOCS/ISOCS also only works on WINDOWS. Though it looks promising from the outside, the inside reveals that the code is basically just using a polynomial or “grid” fit to MCNP data (Venkataraman *et al.*, 2005). Furthermore, one group found that the Canberra LABSOCS/ISOCS software was only accurate to about 8%, and therefore was not good enough to be used for their quantitative analyses (Bossus *et al.*, 2006).

### **2.3.3 Semi-empirical Method Codes**

Several semi-empirical method based codes have been developed. The earliest, SOLANG, was coded for VAX 11/780 in FORTRAN 77, and eventually ported in FORTRAN to PC (Moens *et al.*, 1981). This code restricted volume and disc sources to be centered on the detector’s primary axis. The source code for SOLANG is not available, as the program was commercialized, and has since been incorporated into a

package called KAYZERO/SOLCOI. The other codes based on SOLANG had names like EXTSANGLE, MARSANGLE, and WELLSANGLE. These codes performed effective solid angle calculations for cylindrical, Marinelli, and well geometries respectively.

Another group used the same method, but developed a separate code that used Romberg integration, rather than Moens choice of Gauss-Legendre quadrature (Ugletveit *et al.*, 1989). Also, instead of integrating the detector only once with the coaxial hole included, this code integrated the detector as a true cylinder and then subtracted out the effect of the “coaxial hole” detector. This produced results within 2-3% of experimental data (Ugletveit *et al.*, 1989). Different groups have used Monte Carlo integration and produced results equivalent to numerical integration, as in the code EFFTRAN (Vidmar, 2005; Jiang *et al.*, 1998).

Another group, from the former Yugoslavia, wrote a PASCAL code called ANGLE-PC, which used the same algorithms as the Moens old FORTRAN codes, but with a nicer menu driven front-end (Jovanovic *et al.*, 1997). ANGLE-PC allowed for volume and disc sources to be placed off the primary detector axis. However, despite the stunning accuracy (~3%) and quick run time (~seconds), ANGLE was still designed only to use under WINDOWS and for standard geometric source shapes.

Another code called DETEFF, which has nothing to do with the Monte Carlo code of the same name, was developed (Lippert, 1983). This code does not restrict the source to be on the detector’s primary axis. It uses a simple model of treating the source and detector as collections of point sources. However, the code neglects the central hole in true coaxial, closed-end coaxial, and well detectors. It shows fairly good results for point sources, but the results for sources of other geometrical shapes, appear to be poor

(Lippert, 1983). The source code is unavailable for all of these packages, except possibly EFFTRAN.

Another commercially available program, called SYNTH, allows for the generation of synthetic gamma-ray spectra. This program was developed at Pacific Northwest National Laboratory under WINDOWS and uses Visual Basic combined with old FORTRAN routines. Efficiency curves can be generated based on simple detector parameters, specified in the manufacturers' data sheets. The efficiencies are generated using a version of the single point-to-point detector model (Gunnink, 1972). The most modern version of Gunnink's code, called EFFIC, is incorporated into the GAMANAL and GRPANAL codes. EFFIC allows for several or even no reference points to be used to calculate theoretical efficiency curves (Gunnink, 1990). EFFIC has produced results that agree within an accuracy of a few percent for small or typically encountered sources placed on the detector's primary axis (Gunnink *et al.*, 1992). In addition, the typical run times for the code are fractions of a second. The accuracy of Gunnink's model for arbitrary source shapes and counting geometries is unknown. As will also be shown, the latest version of SYNTH differs dramatically from the latest version of EFFIC.

KMESS combines most of the better features found in the other semi-empirical codes. For example, it allows for arbitrary source shapes, counting geometries, source self-absorption corrections, and absorbers. Because it is also modular, KMESS offers more versatility than the other codes. This means that each of the features in KMESS can be independently improved upon without making major changes to the code. The computational algorithms used in EFFIC, for example, could therefore be easily incorporated into KMESS. KMESS also allows for inhomogeneous radionuclide distributions within the source. In addition, many of the codes aforementioned are either

expensive or no longer available. KMESS eliminates those problems by being open-source and freely distributed.

## **Chapter 3: Theory**

### **3.1 GAMMA-RAY INTERACTIONS**

#### **3.1.1 Introduction to Gamma-ray Interactions**

All radiation detectors should, in principle, produce an output pulse for each quantum of radiation that interacts within its sensitive volume. However, because gamma-rays lack charge, detection is only possible if they first undergo a significant interaction in the detector. There are a large number of interaction mechanisms possible for gamma-rays, but only three play a major role in X-ray and gamma-ray measurements with germanium detectors. These are photoelectric absorption, Compton scattering, and pair production. All of these processes lead to the partial or complete loss of gamma-ray energy in the detector (Knoll, 2000). Each of these processes has a specific gamma-ray energy range in which it is dominant over the other processes. Photoelectric absorption tends to dominate the low energy gamma-ray interactions. Compton, or incoherent, scattering dominates the middle energy gamma-ray interactions. Pair production in the material dominates the higher energy gamma-ray interactions. Figure 3.1 shows the linear attenuation coefficients for germanium as a function of gamma-ray energy. This plot serves to illustrate the effects that each of these processes have on the total linear attenuation coefficient.



# Germanium

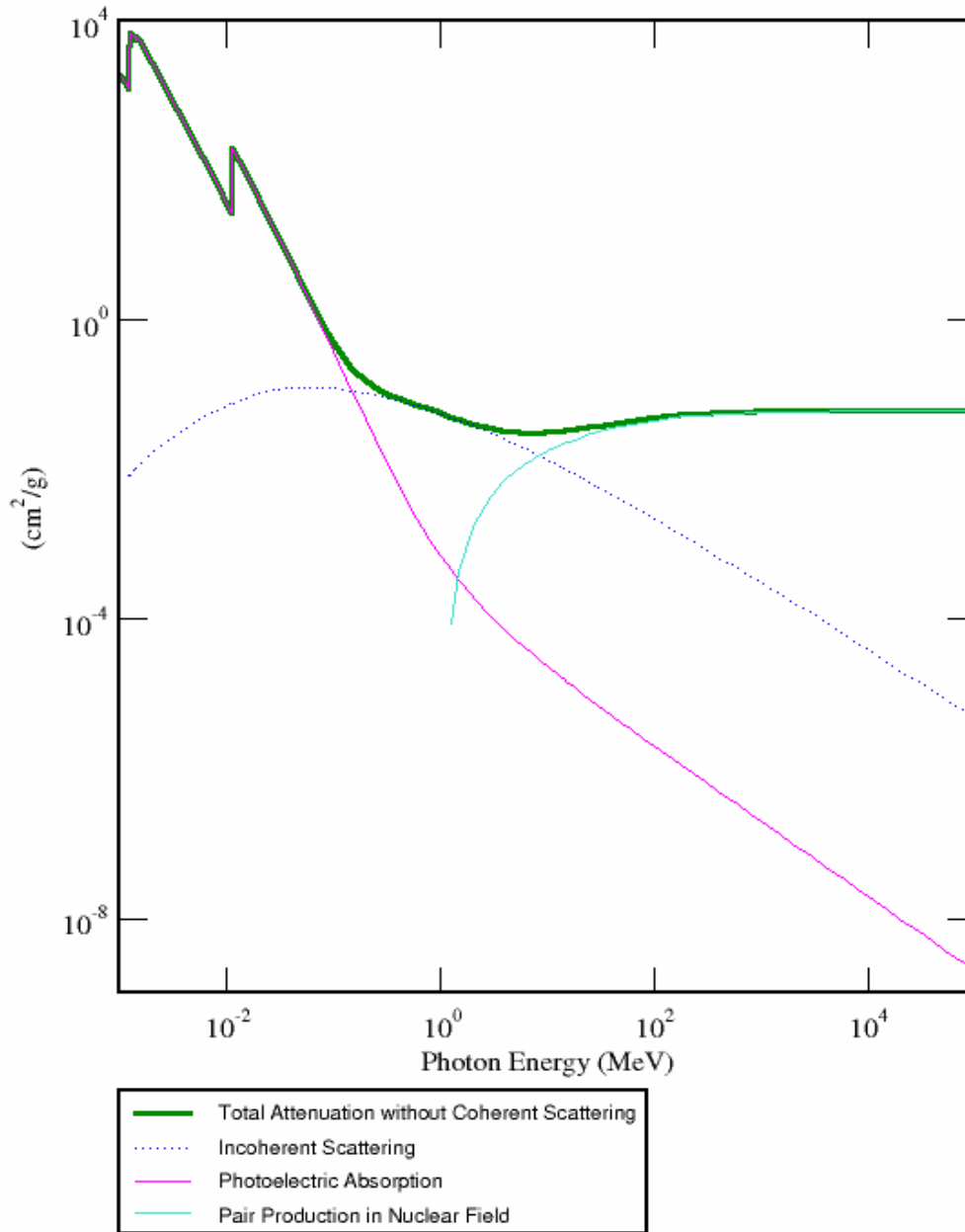


Figure 3.1: Total Linear Attenuation Coefficient for Germanium and Processes that Contribute to it as a Function of Gamma-ray Energy (Berger *et al.*, 2007).

### **3.1.2 Photoelectric Absorption**

When a photon is incident upon the surface of a metal, it is observed that electrons may be ejected (Rohlf, 1994). This phenomenon is known as the photoelectric effect. In photoelectric absorption, a photon interacts with a bound electron in such a way that the photon completely disappears and the atom ejects an energetic photo-electron from one of its bound shells (Knoll, 2000). For this to happen, the energy of the gamma-ray must be greater than the binding energy of the electron. Gamma-rays of sufficient energy will typically eject a photo-electron from the tightly bound K shell of the atom (Knoll, 2000). The ejection of the photo-electron leaves behind a vacancy in one of the atomic shells. This vacancy is filled by the capture of a free electron and/or by the shifting of electrons in other shells. Thus, the production of one or more characteristic X-rays typically accompanies this process.

### **3.1.3 Compton Scattering**

The process by which a photon scatters with a free electron is called Compton, or incoherent, scattering. It is named after Arthur Compton, who first made measurements of photo-electron scattering in 1922 (Rohlf, 1994). In Compton scattering, a photon encounters a free electron, seemingly at rest. The photon imparts some of its energy to the electron, and then deflects through some angle. The electron, having gained some momentum from the collision, then goes off at some other angle. As most electrons encountered in nature are bound in atomic shells, the free electron assumption is not always true. If the binding energy of the electron is taken into account, the energy of the scattered photon spreads into a distribution (Knoll, 2000). However, except for low initial gamma-ray energies, the momentum transferred to the atom in the collision can generally be neglected (Kippen, 2004).

### **3.1.4 Pair Production**

If the energy of the incident gamma-ray energy exceeds twice the rest-mass energy of an electron, 1.022 MeV, the process of pair production becomes possible (Knoll, 2000). The probability for pair production remains very low until the gamma-ray energy approaches several MeV (Knoll, 2000). The interaction typically takes place in the Coulomb field of the nucleus. In pair production, the incident gamma-ray disappears and an electron-positron pair is created. Excess initial gamma-ray energy, above 1.022 MeV, goes into the kinetic energy shared by the positron and electron. The positron is inherently unstable and annihilates on the order of 1 ns after slowing down in the medium (Knoll, 2000). The annihilation of the positron produces two photons of energies 0.511 MeV. Compared with the response time of detectors, 100 to 700 ns, the annihilation of the positron occurs almost instantaneously (Gilmore and Hemingway, 1995). Because of this, the creation of secondary annihilation photons is generally considered to be part of the entire pair production interaction. If one of the annihilation photons escapes, it produces a single escape peak that is seen in the spectrum at 0.511 MeV below the full-energy gamma-ray peak. If both of the annihilation photons escape, it produces a double escape peak that is seen in the spectrum at 1.022 MeV below the full-energy gamma-ray peak.

### **3.1.5 Rayleigh Scattering**

Another gamma-ray interaction mechanism is called Rayleigh, or coherent, scattering. In this case, a photon scatters elastically with all of the electrons in the atom, coherently, and leaves the electrons' energies unchanged (Rohlf, 1994). The gamma-ray

neither excites nor ionizes electrons in the atom and retains most of its original energy after the scattering event. Thus, virtually no energy is exchanged in this reaction, and scattering events do not contribute to detector response (Knoll, 2000). This type of interaction is also strongly forward peaked, so that the gamma-ray is not significantly deflected from its original path (Moens *et al.*, 1981). The probability for Rayleigh scattering is significant only for low photon energies and absorbers with high atomic numbers (Knoll, 2000).

## **3.2 GERMANIUM DETECTORS**

### **3.2.1 Semiconductors**

In order to have a good understanding of the functionality of germanium detectors, it is essential to be familiar with some of the properties of semiconductors. Much of the discussion here will primarily focus on germanium as the semiconductor of interest. However, the properties of other semiconductor materials are similar.

Modern techniques for purifying germanium, such as zone refining, can typically reduce the amount of impurities to less than  $10^9 \text{ atoms} \cdot \text{cm}^{-3}$  (Knoll, 2000). Germanium is therefore a prime candidate for semiconductor studies because of this high level of purity. When atoms of germanium are combined, they bind together to form into a crystalline solid. When this happens, the energy levels of the electron shells broaden into bands that contain a fixed number of electrons (Knoll, 2000). Between these bands are energy regions, also called gaps, which are forbidden to electrons. The lower band that results is called the valence band, which corresponds to the outer-shell electrons being bound to specific lattice sites within the crystal (Knoll, 2000). The upper band is

called the conduction band, in which electrons are free to move about the crystal (Knoll, 2000).

In order for an electron to move between the valence and conduction bands, it must gain or lose an amount of energy equal to the energy of the band gap. Semiconductors typically have a band gap energy of about 1 eV. When an electron is promoted to the conduction band it leaves behind a vacancy in the valence band. This vacancy is effectively positively charged and is called a hole (Gilmore and Hemingway, 1995). The electrons and holes then tend to redistribute themselves until the holes lie at the top of the valence band and the electrons at the bottom of the conduction band.

The electrons and holes can be made to move in the presence of an electric field (Knoll, 2000). Thus, they are often referred to as charge carriers. In the absence of an electric field, the electrons excited to the conduction band would be expected to return back to the valence band. In the presence of an electric field the electrons and holes will migrate against or with the electric field vector respectively (Knoll, 2000). The mobility of these charge carriers contributes to the overall conductivity of the material.

The mobility of charge carriers in a semiconductor material is also highly dependent upon the material temperature. At temperatures above absolute zero, charge carriers can be made to move between the valence and conduction bands simply by thermal excitation from the surroundings. Germanium detectors are typically operated at low temperatures in order to reduce the number of charge carriers arising from thermal excitation. Gamma-rays can also be used to cause the mobility of electron and hole charge carriers. A gamma-ray interaction a semiconductor can often produce primary electrons with energies considerably above the energies of thermally excited charge carriers (Gilmore and Hemingway, 1995).

In general, the discussion above is only valid for pure semiconductor materials. Due to the limitations of modern refining techniques, there will always be a certain amount of impurities leftover. These impurities disturb the electronic balance of the crystal lattice. If the impurity valence state is too low, there will be an absence of electrons at that lattice site, and it will tend to accept electrons. These are called acceptor impurities. A germanium lattice with an overall net acceptor impurity is called *p*-type germanium. On the other hand, if the impurity valence state is too high, there will be an excess of electrons at that lattice site, and it will tend to donate electrons. These are called donor impurities. A germanium lattice with an overall net donor impurity is called *n*-type germanium. Thus, a *p*-type material has an excess of holes, and an *n*-type has an excess of electrons. The impurities effectively negate each other, but the net semiconductor material properties will depend upon which impurity is in excess (Gilmore and Hemingway, 1995). These impurities can be adjusted by adding small amounts of impurities of an appropriate type, a process called doping.

An interesting behavior occurs when two materials of dissimilar semiconductor type are placed in contact with each other, called a *p-n* junction. Under thermal influence the electrons and holes will diffuse from one band to the other, until they have effectively cancelled each other out (Gilmore and Hemingway, 1995). The result is that around the physical junction of the two materials, there will be a region where there are essentially no mobile charge carriers. This is typically called the depletion region because the mobile charge carriers have been depleted there (Simpson, 1987). A net charge will be leftover from the ionized acceptor and donor impurity atoms. This net charge creates an electric potential across the junction, called the contact or diffusion voltage.

An external voltage can be applied across the *p-n* junction, called biasing, to make the materials behave in interesting ways. If a positive voltage is applied to the *n*-type

side of the junction, and a negative to the  $p$ -type side, the effect is a widened depletion region. This is called reverse biasing the junction. If a negative voltage is applied to the  $n$ -type side of the junction, and a positive to the  $p$ -type side, the effect is a smaller depletion region. This is called forward biasing the junction. It is preferable to use a reverse bias for a germanium detector, because a larger depletion region translates into a larger sensitive detector volume.

### 3.2.2 Detector Characteristics

There are two main types of germanium detectors that result from the process of purifying germanium. The leftover impurities in the crystal determine whether the detector will become an  $n$ -type or  $p$ -type. Donor and acceptor atoms are typically added to the crystal surfaces in the form of contact layers. These layers create a reverse biased  $p$ - $n$  junction, and allow for the crystal region between the contacts to be fully depleted. The detector type determines how and where these contacts are applied.

One widely used crystal shape is called a coaxial design. Figure 3.2 shows the typical coaxial crystal designs, as well as the placement of the contact layers on the crystal surfaces. All of the germanium detectors used in experiments and simulations in this work were  $p$ -type and closed-end coaxial. The  $p$ -type contact is typically a layer 0.3  $\mu\text{m}$  thick of ion-implanted boron. The  $n$ -type contact is typically a layer 700  $\mu\text{m}$  thick of diffused lithium. However, the  $n$ -type contact thickness for a typical lithium-drifted detector is greater.

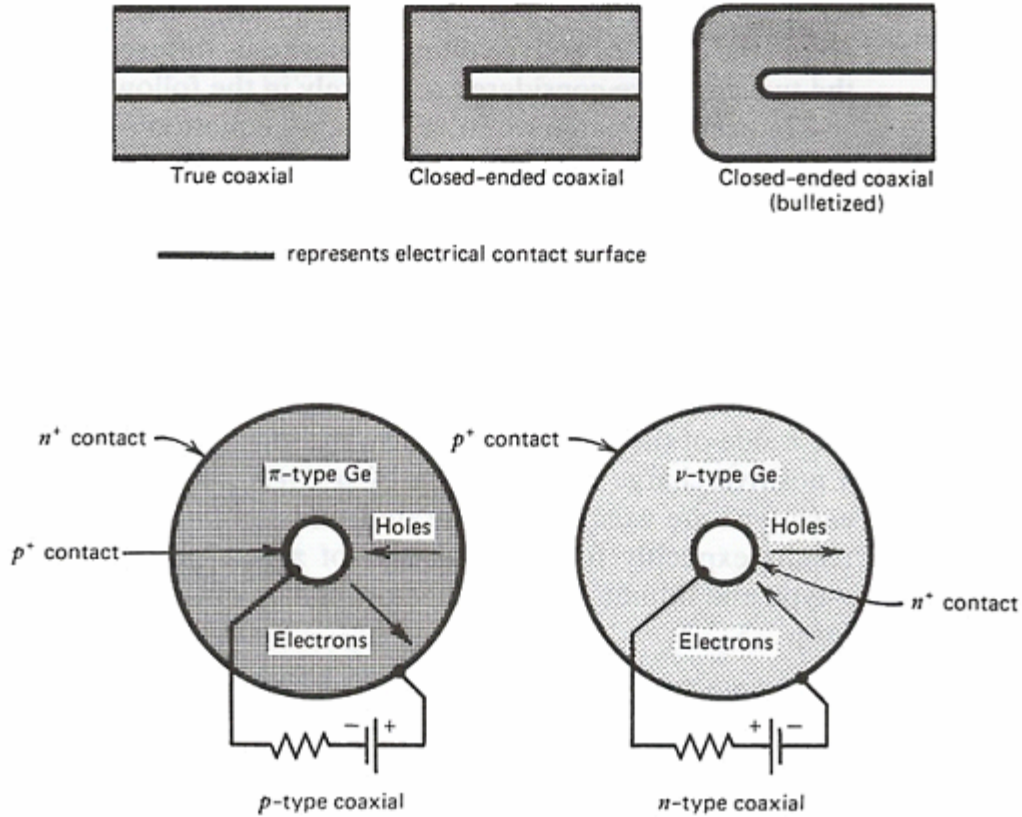


Figure 3.2: Three Common Coaxial Detector Designs and the Placement of Contact Layers (Knoll, 2000).

The sensitive detector region is in general, the region between the  $n$ -type and  $p$ -type contacts (Knoll, 2000). The region between the physical crystal surface and contact layer is therefore not considered a sensitive part of the detector. This region acts as a dead-layer of material to incident radiation, because the contacts generally have appreciable thicknesses. For instance,  $p$ -type detectors have the thicker  $n$ -type contact layer on their outer surface, and thus have a thicker outer dead-layer. This dead-layer will attenuate photons that pass through it. For gamma-ray energies over 200 keV, this attenuation is generally negligible. However, lower energy gamma-rays can be severely attenuated by this dead-layer. It has been shown that the dead-layer varies in time and



over the surface of the crystal (Knoll, 2000; Keyser, 2002). Thus, the dead-layer thickness quoted on a manufacturer specification sheet is more of an approximation to the average dead-layer thickness. However, several experimental measurements would allow one to quantify the dead-layer more accurately (Jackman, 2004).

### **3.2.3 Detector Use and Corrections**

Basic detector operation is obtained by applying a high voltage reverse bias to the detector contacts. This voltage fully depletes the region between the contacts and produces a sensitive detector volume of mobile charge carriers. The electrons and holes are swept out the sensitive detector volume by this voltage, along its electric field lines. The charges are collected by the preamplifier and turned into voltage pulses. The amplitude of these pulses is proportional to the energy deposited by the incident gamma-ray. The output of the preamplifier is generally fed into an amplifier to change the pulse shape and increase its magnitude. A multi-channel analyzer (MCA) is then used to sort the pulses based on their amplitudes. The result of the binning produces what is commonly seen as an energy spectrum.

To produce meaningful results, a semiconductor detector must be kept at very low temperatures. If the detector is operated at room temperature, there will be too large of a thermally-induced leakage current. This is because the band gap of germanium is only about 0.7 eV, and a large number of thermally excited charges will easily cross the band gap (Knoll, 2000). These thermally induced charges will tend to dominate the detector's signal in the form of noise, and degrade its energy resolution. In order to reduce the thermally induced leakage current, the detectors are typically cooled to around 77 K. Cooling is often done using liquid nitrogen in an insulated dewar that is kept in thermal

contact with the detector. The detector is also housed in a vacuum-tight cryostat to reduce thermal conductivity with the surroundings.

There are several corrections that often need to be made to detector observations. These are dead-time, pulse pile-up, and summing corrections. Dead-time is a measure of the minimum amount of time needed between pulses in order to record them as separate events. Dead-time is a function of count rate, so that higher activity samples produce higher dead-time losses. Corrections for this effect are usually made in the multi-channel analyzer. Another problem encountered is when two events are recorded as one pulse from the detector. If multiple radiations from the same nuclear decay event are observed this is called true coincidence summing. However, if multiple events are added together into a single pulse because of the inherent limited resolving time of the detector, this is called random coincidence summing or pulse pile-up. Pulse pile-up is proportional to the square of the counting rate, whereas true coincidence summing is linearly proportional to it (Knoll, 2000).

### **3.3 TRADITIONAL AND MOENS EFFICIENCY CALCULATIONS**

#### **3.3.1 Traditional Method**

##### ***3.3.1.1 Remarks on the “Efficiency”***

In the field of gamma-ray spectroscopy, it is common to hear someone talk about the “efficiency” of a detector. There are typically four efficiencies of interest in studying germanium detectors, namely the relative, geometric, absolute, and intrinsic efficiencies. The absolute and intrinsic efficiencies are typically split up into two distinct classes called the full-energy peak and total efficiencies.

The relative efficiency is commonly encountered when looking at detector manufacturer specifications. It is the general performance measure relating the efficiency of detection for a gamma-ray at 1332 keV of the detector to that of a standard sodium iodide scintillation detector (Gilmore and Hemingway, 1995). However, the relative efficiency is of little, if any, importance to this work, so nothing more about it will be mentioned.

The geometric efficiency is a measure of the geometric attenuation that results from the unique counting scheme. It is directly related to the solid angle of a source that is subtended by the detector. This is useful in determining the fraction of gamma-rays leaving a source that enter the detector. However, it does not take into account the different interaction types that can cause a gamma-ray to lose energy along its path.

There are often times when one needs to know the radioactivity of a source. This is generally done by using the absolute full-energy peak efficiency. In gamma-ray spectroscopy, the absolute full-energy peak efficiency is the ratio of pulses recorded under the photopeak to the total number of gamma-rays emitted by the source. This efficiency depends strongly on the geometrical counting arrangement and on the detector properties. The absolute total efficiency is the ratio of the total number of pulses recorded in the entire spectrum to the total number of gamma-rays emitted by the source. It is common in gamma-ray spectroscopy to use full-energy peak efficiencies, because the number of full-energy events is less influenced by noise in the system or effects like scattering from surrounding objects. The full-energy peak efficiency should not be confused with the peak efficiency, which describes the maximum efficiency of the detector.

The intrinsic full-energy peak efficiency is the ratio of the number of pulses recorded under the photopeak to the total number of gamma-rays incident on the detector.

Similarly, the intrinsic total efficiency is the ratio of the total number of pulses recorded in the whole spectrum to the total number of gamma-rays incident on the detector. The intrinsic efficiencies are based solely on the properties of the detector. The main difference between the intrinsic and absolute efficiency is that the absolute efficiency depends on this geometrical arrangement, whereas the intrinsic efficiency does not.

### ***3.3.1.2 Traditional Geometric Solid Angle***

One main principle of calculating the efficiency of a detector is the concept of the geometrical solid angle. The common definition for the geometrical solid angle for thin detectors, like surface barrier detectors, is shown in Equation 3.1 (Knoll, 2000).

$$\Omega = \int_A \frac{\cos \alpha}{r^2} dA. \quad (3.1)$$

Where:  $\Omega$  is the solid angle subtended by a thin detector of area A (in steradians).

$dA$  is a detector surface element.

$r$  is the distance between the source and surface element  $dA$ .

$\alpha$  is the angle between the normal to the surface element  $dA$  and the source direction.

It is more convenient to express the geometrical solid angle in vector form. This allows the expression to be generalized to arbitrary source and detector geometries. In order to do this a fundamental principle of vector calculus is necessary. Equation 3.2 is the typically encountered form for the dot product of two vectors.

$$\vec{A} \cdot \vec{B} = |A||B| \cos \alpha. \quad (3.2)$$

Where:  $\vec{A}$  is some vector with magnitude  $|A|$ .

$\vec{B}$  is some vector with magnitude  $|B|$ .

$\alpha$  is the angle between the vectors  $\vec{A}$  and  $\vec{B}$ .

In the case of the geometrical solid angle, the normal to the surface element is a unit normal and has a magnitude of 1 and some direction  $\hat{n}_u$ . Therefore the dot product of the source vector with the unit normal direction is just a projection of the source magnitude along the unit normal direction  $\hat{n}_u$ . Equation 3.2 can then be rewritten as Equation 3.3.

$$\vec{TP} \cdot \vec{n}_u = |TP||1| \cos \alpha = |TP| \cos \alpha. \quad (3.3)$$

Where:  $\vec{TP}$  is the vector from a point  $T$  in the source to a point  $P$  on the detector surface.

$\vec{n}_u$  is the unit vector normal to the detector at the surface element of interest.

$|TP|$  is the magnitude of vector  $\vec{TP}$ .

$|1|$  is the magnitude of unit vector  $\vec{n}_u$ , which is by definition unity.

$\alpha$  is the angle between the vectors  $\vec{TP}$  and  $\vec{n}_u$ .

The  $r$  in Equation 3.1 should be taken to mean  $|TP|$ , the magnitude of the vector  $\vec{TP}$ . This is the magnitude of the distance from a point  $T$  in the source to a variable point

$P$  on the detector surface,  $S$ . One can then express the geometrical solid angle in the vector form, by combining Equations 3.3 and 3.1 to yield Equation 3.4. This is the geometrical solid angle equation in a generic form.

$$\Omega = \iint_S \frac{\cos \alpha}{|TP|^2} d\sigma = \iint_S \frac{\vec{TP} \cdot \vec{n}_u}{|TP|^3} d\sigma. \quad (3.4)$$

Where:  $d\sigma$  is an infinitesimal area of surface  $S$ .

### 3.3.2 Moens Method

#### 3.3.2.1 Moens Geometric Solid Angle

The semi-empirical Moens method begins with the experimental determination of the absolute full-energy peak efficiency versus photon energy curve for a reference source shape and source-detector distance. This was typically done using a certified gamma-ray emitting source at a large source-detector distance to reduce summing effects. This was done for a large number of gamma-ray energies, to better characterize the absolute full-energy peak efficiency versus photon energy curve (Moens *et al.*, 1982). Next, the total efficiency was calculated for this reference configuration and calculated for any required source-detector distance and source geometry. The reference measured absolute full-energy peak efficiency, calculated reference total efficiency, and calculated total efficiency for the desired geometry were then used to predict the desired absolute full-energy peak efficiency.

Assume the detector of interest is a cylinder of radius  $R_0$  and height  $H$ . Also assume that the source is a point located above the detector surface, but at a radial distance from the  $z$ -axis less than the radius of the detector. Draw the three-dimensional

Cartesian coordinate axes such that the origin lies in the center of the top of the detector surface. Make the axes such that the  $z$ -axis points along the cylindrical detector's primary axis as shown in Figure 3.3. The unit normal vector  $\vec{n}_u$  then points in the minus  $z$ -direction.

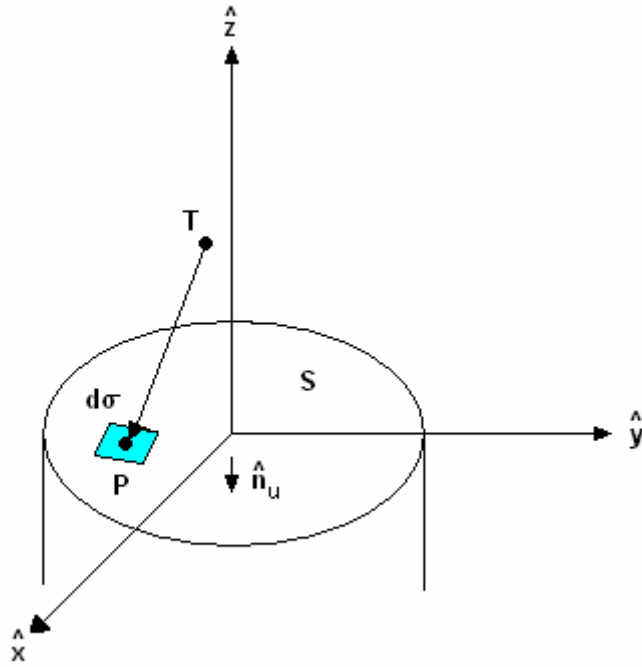


Figure 3.3: Graphical Representation of Cartesian Coordinate System Established for Geometrical Solid Angle Calculations When Source is Located Above the Detector.

Let the points  $T$  and  $P$  be expressed as three-dimensional sets in Cartesian coordinates such as  $T(x_T, y_T, z_T)$  and  $P(x_P, y_P, z_P)$ . Equation 3.4 can be evaluated for the case of Figure 3.3, and expressed as Equation 3.5.

$$\Omega = \iint_S \frac{\vec{TP} \cdot \vec{n}_u}{|TP|^3} d\sigma = \iint_S \frac{z_T}{\left[ (x_P - x_T)^2 + (y_P - y_T)^2 + (z_P - z_T)^2 \right]^{\frac{3}{2}}} dx dy. \quad (3.5)$$

The choice of coordinate system was such that the surface of the detector top was chosen to coincide with the  $z = 0$  plane and therefore  $z_p = 0$ . The dot product in the numerator is the projection of the vector  $\vec{TP}$  along the unit  $\vec{n}_u$  vector, pointing in the minus  $z$ -direction, which is just the  $z$ -coordinate of  $T$ , namely  $z_T$ . The magnitude of the vector  $\vec{TP}$ , also written as  $|TP|$ , is just the usual square root of the sum of squares of the distances from for the magnitude of a vector. Equation 3.5 can therefore be rewritten as Equation 3.6.

$$\Omega = \iint_S \frac{z_T}{\left[ (x_p - x_T)^2 + (y_p - y_T)^2 + z_T^2 \right]^{\frac{3}{2}}} dx dy. \quad (3.6)$$

It is furthermore convenient to formulate this problem in terms of cylindrical coordinates, due to the fact that we have cylindrical symmetry. Assume that in cylindrical coordinates the points  $T$  and  $P$  have coordinate sets  $T(r, \phi, z_T)$  and  $P(R, \phi, z_p)$  respectively. Because we are only performing one integral here, it is advantageous to choose the coordinate system cleverly. Assume that we choose the point  $T$  to lie in the  $x$ - $z$  plane. This makes the  $y$ -coordinate of  $T$  zero in Cartesian coordinates, but also makes  $\phi = 0$  in cylindrical coordinates. Introducing the resulting polar coordinates, in place of the Cartesian ones, produces Equation 3.7. This equation can be further simplified by our choice of coordinates to Equations 3.8 and 3.9.

$$\Omega = \iint_S \frac{z_T R}{\left[ (R \cos \phi - r \cos \phi)^2 + (R \sin \phi - r \sin \phi)^2 + z_T^2 \right]^{\frac{3}{2}}} dR d\phi. \quad (3.7)$$

$$\Omega = \iint_S \frac{z_T R}{\left[ (R \cos \phi - r)^2 + (R \sin \phi - 0)^2 + z_T^2 \right]^{\frac{3}{2}}} dR d\phi. \quad (3.8)$$



$$\Omega = \int \int_S \frac{z_T R}{\left[ R^2 - 2Rr \cos \phi + r^2 + z_T^2 \right]^{\frac{3}{2}}} dR d\phi. \quad (3.9)$$

Noticing the angular symmetry in the problem and introducing the correct limits of integration yields Equation 3.10.

$$\Omega = 2z_T \int_0^\pi d\phi \int_0^{R_0} \frac{R}{\left[ R^2 - 2Rr \cos \phi + r^2 + z_T^2 \right]^{\frac{3}{2}}} dR. \quad (3.10)$$

### 3.3.2.2 Effective Solid Angle

Knowing the geometrical solid angle is useful, but only solves for the geometrical relationship associated in determining the efficiency of a detector. It was shown that only the simultaneous treatment of geometry, gamma-ray attenuation, and detector response is justified (Moens *et al.*, 1981). Hence, the concept of effective solid angle was introduced.

The quantity of interest here is the absolute full-energy peak efficiency. The absolute full-energy peak efficiency can be found through any of the methods discussed in Chapter 2.2. The calculation of the total efficiency, the probability for an emitted photon to hit the detector and undergo inelastic interaction within the detector material, is a matter of mathematical analysis (Moens *et al.*, 1982). The conversion of the total efficiency to the full-energy peak efficiency can be done using the “virtual” peak-to-total ratio as shown in Equation 3.11.

$$\varepsilon_p = \frac{P}{T} \varepsilon_T \quad (3.11)$$

Where:  $\varepsilon_p$  is the absolute full-energy peak efficiency.

$\varepsilon_T$  is the absolute total efficiency.

$\frac{P}{T}$  is the “virtual” peak-to-total ratio.

The “virtual” peak-to-total ratio refers to a hypothetical bare and isolated detector crystal, assumes no photon scattering occurs on inactive parts of the setup, and is different from what would be measured in an actual counting experiment (Moens *et al.*, 1982). This is because, in experiments, gamma-rays undergo inelastic scattering in adjacent and surrounding materials and then contribute to the total area of the spectrum by reaching the detector with degraded energy (Moens *et al.*, 1982). The experimentally measured peak-to-total ratio is therefore dependent on sample counting geometry (Moens *et al.*, 1982). Historically, the “virtual” peak-to-total ratio was assumed to be a constant of the detector crystal, and independent of source geometry, source composition, and source-to-detector distance (Moens *et al.*, 1982). However, this assumption was made for sources confined to the region above the detector surface and at a radial distance from the  $z$ -axis less than the radius of the detector. If the source is moved out of this region, the “virtual” peak-to-total should be expected to change. This is primarily due to the fact that there would be a change in the amount of active detector material a photon would pass through before either complete absorption or escaping the sensitive region of the detector.

Any desired absolute full-energy peak efficiencies were calculated using experimentally measured reference absolute full-energy peak efficiencies and calculated absolute total efficiencies. The desired absolute full-energy peak efficiency curves were

then calculated using Equation 3.12. For computational purposes, an equivalent formula was used, Equation 3.14, which was obtained by combining Equations 3.12 and 3.13.

$$\varepsilon_{P,X} = \varepsilon_{P,ref} \frac{\varepsilon_{T,X}}{\varepsilon_{T,ref}}. \quad (3.12)$$

Where:  $\varepsilon_{P,X}$  is the absolute full-energy peak efficiency of the desired source geometry “X”.

$\varepsilon_{P,ref}$  is the absolute full-energy peak efficiency of the reference, experimentally measured, source geometry.

$\varepsilon_{T,X}$  is the total efficiency of the desired source geometry “X”.

$\varepsilon_{T,ref}$  is the total efficiency of the reference, experimentally measured, source geometry.

$$\varepsilon_T = \frac{\bar{\Omega}}{4\pi}. \quad (3.13)$$

Where:  $\bar{\Omega}$  is the effective solid angle subtended at the source by the detector.

$\varepsilon_T$  is the total efficiency.

$$\varepsilon_{P,X} = \varepsilon_{P,ref} \frac{\bar{\Omega}_{T,X}}{\bar{\Omega}_{T,ref}}. \quad (3.14)$$

Where:  $\bar{\Omega}_{T,X}$  is the effective solid angle subtended for the desired source geometry “X”.

$\bar{\Omega}_{T,ref}$  is the effective solid angle subtended for the reference geometry.

It has been mentioned several times that only the simultaneous solution of detector response, geometry, and photon attenuation was found to be valid (Moens *et al.*, 1981). Thus, until now only geometry has been taken into account. The next factor considered was the photon attenuation of the source by any materials situated between the source and detector. Examples include the source itself, source container, air, detector end-cap, and the germanium crystal dead layer. To correct for this effect, the inner integrand of Equation 3.10 is multiplied by Equation 3.15. Rayleigh scattering is ignored in this calculation because it has a negligible effect on the incident gamma-ray's energy and path (Moens *et al.*, 1981).

$$F_{att} = \exp\left(-\sum_{i=1}^m \mu_i \delta_i\right). \quad (3.15)$$

Where:  $F_{att}$  is the attenuation factor.

$\mu_i$  is the linear, total narrow beam absorption coefficient, of a given energy, of the  $i$ th absorber, excluding Rayleigh scattering.

$\delta_i$  is the undisturbed path length of the photon through the  $i$ th absorber.

$m$  is the total number of absorbers.

The next factor of interest involved a characterization of the detector response, called the intrinsic efficiency factor. This was a measure of the probability that a photon impinging on the active zone of the detector would interact within the detector material before leaving. It was decided to multiply the inner integrand of Equation 3.10 by Equation 3.16. Notice that for photons not passing through the coaxial hole, sometimes called the  $p$ -core,  $\Delta_2 = 0$ , and therefore  $\Delta_1$  is the undisturbed distance traveled in the

crystal. The same conditions arise for a detector crystal with no coaxial hole. Rayleigh scattering is ignored in this calculation because it does not contribute to detector events (Moens *et al.*, 1981).

$$F_{eff} = 1 - \exp(-\mu_d \Delta_1) + ((1 - \exp(-\mu_d \Delta_2)) * \exp(-\mu_h \eta - \mu_d \Delta_1)). \quad (3.16)$$

Where:  $F_{eff}$  is the intrinsic efficiency factor.

$\mu_d$  is the linear, total narrow beam absorption coefficient, of a given energy, of the detector, excluding Rayleigh scattering.

$\mu_h$  is the linear, total narrow beam absorption coefficient, of a given energy, of the coaxial hole, excluding Rayleigh scattering.

$\Delta_1$  is the undisturbed distance traveled in the detector active zone before entering the coaxial hole along a path  $\vec{TP}$ .

$\Delta_2$  is the undisturbed distance traveled in the detector active zone after leaving the coaxial hole along a path  $\vec{TP}$ .

$\eta$  is the undisturbed distance traveled along a path  $\vec{TP}$  inside the coaxial hole.

All three of these necessary factors can be combined to yield Equation 3.17. This is the cylindrical coordinate Moens solution for the effective solid angle of a point source situated at a radial distance from the  $z$ -axis less than the radius of the detector.

$$\bar{\Omega} = 2z_T \int_0^\pi d\phi \int_0^{R_0} \frac{F_{att} F_{eff} R}{[R^2 - 2Rr \cos \phi + r^2 + z_T^2]^{\frac{3}{2}}} dR. \quad (3.17)$$

The calculation of several parameters in both the attenuation and intrinsic efficiency factors is non-trivially dependent upon the path that a photon takes from the source to detector before interaction. However, all of the necessary path lengths in both can be determined either analytically or from intersections of the photon path with important planes and cylinders. Equation 3.17 is typically integrated numerically, as analytical solutions for this integral form are not readily available. A photon can only travel one of eight paths, when the source is located above the detector and at a radial distance from the  $z$ -axis less than the radius of the detector (Moens *et al.*, 1981). These eight paths are depicted in Figure 3.4. Logical testing of the photon path traveled at every piece-wise step during numerical integration of Equation 3.17 was performed to determine the effective solid angle. The necessary logical test conditions were determined from intersections of the photon path traveled with important detector, and absorber, planes and cylinders (Moens *et al.*, 1981).

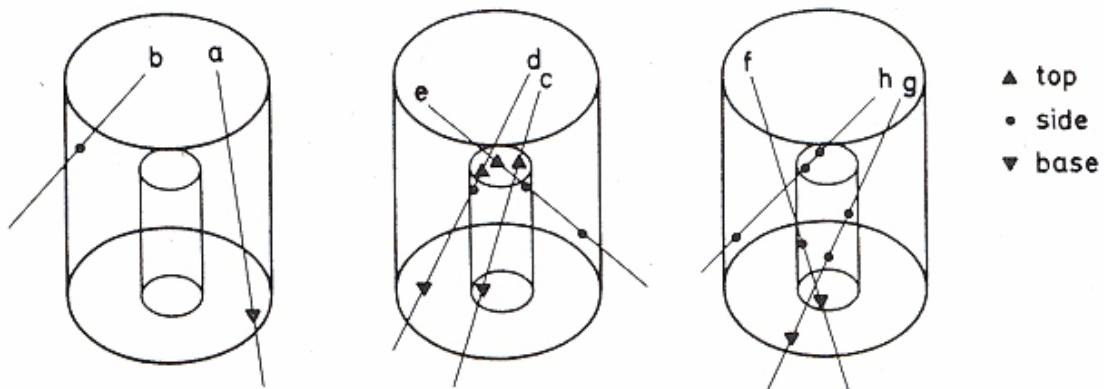


Figure 3.4: Paths  $a$  Through  $h$  Show Possible Paths to be Followed by a Photon Impinging upon the Detector Top Surface (Moens *et al.*, 1981).

This same method has been applied to yield the effective solid angles for cylindrical detectors with disc and cylindrical sources (Moens *et al.*, 1981). However, the solutions derived there are only valid when the entire source remains completely within radial distances from the  $z$ -axis less than the radius of the detector. The effective solid angle for a cylindrical source and cylindrical detector valid for any radial distance or source radius has been determined (Jovanovic *et al.*, 1997). This has also been determined for Marinelli and well geometries (Jovanovic *et al.*, 1997).

### **3.4 MESH-GRID METHOD EFFICIENCY CALCULATIONS**

#### **3.4.1 Assumptions**

In the Moens method, the sample shapes were geometrically restricted to standard geometric shapes (point, disk, cylinder, Marinelli, or well). If one desired to solve those integrals for some arbitrary sample shape, the resulting mathematical equations could become extremely complicated. Many approximations to the standard geometric shapes would then be necessary. Thus, a new method must be employed that simplifies the whole approach.

Suppose that instead of modeling a cylindrical sample as a cylinder, and solving for some complicated integral, the cylinder is chopped into a bunch of tiny pieces and then each piece is approximated as a point source. Then the source geometry becomes trivial, because any geometry could then be approximated as a collection of point sources. This process is hereby called meshing or the mesh-grid method. In the event that the grid size, or mesh order, becomes large enough, the point source grid approximation should approach the true continuous solution. One should also expect that

there will be a trade-off in the mesh order between accuracy and computational time. This is because choosing a higher mesh order will mean modeling more point sources and hence, performing more effective solid angle integral calculations.

Several other assumptions in the mesh-grid method are made, and the validity of each is addressed further in Chapter 5. One assumption is the invariance of the “virtual” peak-to-total ratio on sample position. Another is that the detector is well approximated by a cylinder. If the coaxial detector had been treated as a solid crystal detector minus a “hole detector,” that assumption would need justification. However, the work here has chosen simply to use logical loops and avoid that assumption altogether. Lastly, the work performed here assumed that the radionuclides within the source were distributed homogeneously. This was necessary because the exact distribution of radionuclides within a source is rarely known. However, the mesh-grid method and KMESS code are generalized to include a weighting factor in the averaging calculations to allow correction for the source distribution. This weighting factor was set to 1 for all calculations made in this work.

### **3.4.2 Mathematical Form**

Suppose that we have a point source as mentioned above in the Moens method. The same coordinate system used in the Moens method will be employed here. As long as the point remains above the detector top surface and at a radial distance from the  $z$ -axis, no larger than the radius of the detector, Equation 3.17 will suffice. However, once the point source is moved to the detector side, or to a radial distance from the  $z$ -axis greater than the radius of the detector, new integrals must be employed. There are also four additional possible paths through the detector other than those shown in Figure 3.4. The additional possible paths are shown in Figure 3.5.



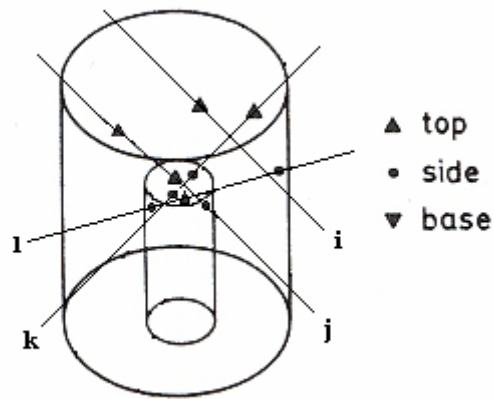


Figure 3.5: Paths *i* Through *l* Show the Four Additional Possible Paths to be Followed by a Photon Impinging Upon the Detector Side Surface (modified from Moens *et al.*, 1981).

Assume first, that the source is placed to the side of the detector, below the plane of the top detector surface, and above the plane of the bottom of the detector surface. This means that photons emitted will only enter the detector through the detector's side surface. The corresponding effective solid angle integral was derived analytically and is shown in Equation 3.18. Note that the origin is still placed on the detector's top surface centered on the detector's primary axis. Also note that the point source is still confined to the  $x$ - $z$  plane, hence and the  $y$ -coordinate of the source location at point  $T$  is zero in Cartesian coordinates. The setup for this case is shown in Figure 3.6.

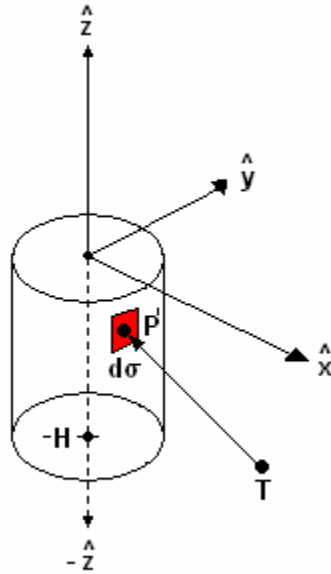


Figure 3.6: Graphical Representation of Cartesian Coordinate System Established for Geometrical Solid Angle Calculations When Source to the Side of the Detector.

$$\bar{\Omega} = 2 \int_{\phi_{MIN}}^{\phi_{MAX}} R_0 d\phi \int_{-H}^0 \frac{F_{att} F_{eff} (r \cos \phi - R_0)}{\left[ R_0^2 - 2R_0 r \cos \phi + r^2 + (z_p - z_T)^2 \right]^{\frac{3}{2}}} dz_p . \quad (3.18)$$

Where:  $R_0$  is the radius of the detector.

$H$  is the detector height.

$r$  is the perpendicular distance from the source to the  $z$ -axis.

$\phi$  is the angular polar coordinate of a point on the detector's side surface.

$F_{att}$  is the attenuation factor.

$F_{eff}$  is the intrinsic efficiency factor.

$z_p$  is the  $z$ -coordinate of a point on the detector's side surface.

$z_T$  is the  $z$ -coordinate of the point source.

$$\begin{aligned} \phi_{MIN} \text{ is minimum angular polar coordinate} & \begin{cases} 0, & \text{for } +x \\ \pi, & \text{for } -x \end{cases} \\ \phi_{MAX} \text{ is maximum angular polar coordinate} & \begin{cases} \cos^{-1}\left(\frac{R_0}{r}\right), & \text{for } +x \\ \pi + \cos^{-1}\left(\frac{R_0}{r}\right), & \text{for } -x \end{cases} \end{aligned}$$

Measurement of  $z_T$  is trivial; it is just the distance from the top of the detector surface to the point source in a plane parallel to the  $z$ -axis. Measurement of  $r$  is in principle possible, but may not be necessarily desired for this specific geometry. If we notice that we have still required the  $y$ -coordinate to be zero, by confining the point source to be in the  $x$ - $z$  plane, then by polar coordinate definition,  $x_T = r \cos \phi = r \cos 0 = r$ ; that is, the radial coordinate is the same as the Cartesian  $x$ -coordinate of the point source. It may be more convenient, however, to define a new variable  $d$  that measures the distance of the point source from the detector. Let  $d$  be the distance from the point source to the side surface of the detector, measured in a plane parallel to the  $x$ -axis and hence perpendicular to the  $y$ - and  $z$ -axes. This new variable can be written in terms of known quantities such that  $d = r - R_O = x_T - R_O$ . Using this identity, Equation 3.18 can be rewritten as Equation 3.19.

$$\bar{\Omega} = 2 \int_{\phi_{MIN}}^{\phi_{MAX}} R_O d\phi \int_{-H}^0 \frac{F_{att} F_{eff} (d \cos \phi + R_0 (\cos \phi - 1))}{\left[ R_O^2 - 2R_O (d + R_O) \cos \phi + (d + R_O)^2 + (z_P - z_T)^2 \right]^{\frac{3}{2}}} dz_P. \quad (3.19)$$

This can be further simplified to Equation 3.20.

$$\bar{\Omega} = 2 \int_{\phi_{MIN}}^{\phi_{MAX}} R_O d\phi \int_{-H}^0 \frac{F_{att} F_{eff} (d \cos \phi + R_0 (\cos \phi - 1))}{\left[ 2(1 - \cos \phi)(R_O^2 + R_O d) + d^2 + (z_P - z_T)^2 \right]^{\frac{3}{2}}} dz_P. \quad (3.20)$$

Equation 3.20 is the effective solid angle solution for a point source located along side the detector. Hence, this integral is good for the region below the plane of the top surface of the detector and above the plane of the bottom of the detector. It should be noted, that the point source only “sees” less than half of the curved side of the cylindrical detector. Hence, the detector surface area of the “dark-side,” the side facing away from the point source, is justifiably not included in the integration.

Up to now, we have confined the photons to only enter the detector through the either the top or the side surfaces. Now, suppose we have a point source located in the region above the detector top surface, but also at a radial distance from the  $z$ -axis greater than the radius of the detector, as shown in Figure 3.7. This means that the photons emitted from a point source will interact both in the detector’s top and side surfaces.



Where:  $\bar{\Omega}$  is the total effective solid angle.

$d\bar{\Omega}$  is the differential effective solid angle of any arbitrary surface.

$S_{top}$  is the detector's top surface.

$S_{side}$  is the detector's side surface.

The integral of Equation 3.21 is trivial to evaluate for a point source, now that it has been broken up. This is because the top and side surface integrals have already been separately solved for point sources displaced off the detector's primary axis. This means simply that the first integral in Equation 3.21 is just Equation 3.17 and the second integral is just Equation 3.18. Thus, combining of all three of these equations we can write Equation 3.22. It should be noted, that this integral is the "master mesh-grid formula" for a point source that reduces to Equations 3.17 or 3.18 under appropriate boundary conditions. This formula is also applicable, by symmetry, to points located below the detector's bottom surface at an arbitrary point, by simply requiring the  $z$ -axis point in the opposite direction. This assumption is even true if the detector is a closed-end coaxial detector, because the intrinsic efficiency factor,  $F_{eff}$ , takes the coaxial hole into account. It was shown, that in order to simplify the intrinsic efficiency factor,  $F_{eff}$ , that the effective solid angle of the "coaxial hole detector" could be simply be subtracted from the effective solid angle of a true cylindrical detector (Ugletveit *et al.*, 1989). However, this assumption was not made, because the correct photon path lengths were instead found using logical loops.

$$\begin{aligned}
\bar{\Omega} = & 2z_T \int_0^\pi d\phi \int_0^{R_0} \frac{F_{att} F_{eff} R}{\left[ R^2 - 2Rr \cos\phi + r^2 + z_T^2 \right]^{\frac{3}{2}}} dR + \\
& + 2 \int_{\phi_{MIN}}^{\phi_{MAX}} R_O d\phi \int_{-H}^0 \frac{F_{att} F_{eff} (r \cos\phi - R_O)}{\left[ R_O^2 - 2R_O r \cos\phi + r^2 + (z_P - z_T)^2 \right]^{\frac{3}{2}}} dz_P
\end{aligned} \tag{3.22}$$

Suppose now that one desires to model some arbitrary source shape using the mesh-grid method. The difficulty now arises as to how to take all these “grid-point” absolute full-energy peak efficiencies and add them up to yield the average absolute full-energy peak efficiency. If the radionuclides in the source are distributed within the source homogeneously, then every point could be weighted equally and Equation 3.23 would reduce to Equation 3.24. If the distribution of radionuclides in the source were distributed heterogeneously, it would be necessary to introduce weighting factors that correctly describe the distribution of radionuclides for the source, and use Equation 3.23. For the purposes of this work, all sources were assumed to have a homogenous radionuclide distribution within them.

$$\bar{\varepsilon} = \frac{\sum_{i=1}^N a_i \varepsilon_i}{\sum_{i=1}^N a_i} \tag{3.23}$$

Where:  $N$  is the mesh order, or number of grids (ie. the number of point source efficiencies).

$a_i$  is the  $i$ th weighting factor, all = 1 for a homogeneously distributed source.

$\varepsilon_i$  is the absolute full-energy peak efficiency of the  $i$ th point source within the grid.

$\bar{\varepsilon}$  is the calculated average absolute full-energy peak efficiency.

$$\bar{\varepsilon} = \frac{\sum_{i=1}^N \varepsilon_i}{N}. \quad (3.24)$$

For large sources, sample self-attenuation corrections would need to be included. This would be taken into account in the attenuation factor,  $F_{att}$ . For sources close to the detector, the experimentally obtained data may need coincidence summing corrections. However, the way in which experimental data are corrected for coincidence summing is beyond the scope of this work.

Performing effective solid angle calculations using a semi-empirical mesh-grid method only yields the total detector efficiency. A reference efficiency curve, as in the Moens method, or knowledge of the “virtual” peak-to-total ratio would be required to convert to full-energy peak efficiency as in Equations 3.11 or 3.12. The experimentally measured peak-to-total ratio was found to be counting geometry dependent (Moens *et al.*, 1982). Thus, experimentally obtained values of the peak-to-total ratio would not be able to convert to true full-energy peak efficiency using this method (Moens *et al.*, 1982). The conversion of total to full-energy peak efficiency should therefore be done through a meticulous measurement of a reference efficiency curve and counting geometry. Thus, the averaging of the finite number point sources, combined with calculations of effective solid angles, and a carefully measured reference curve, will yield the absolute full-energy peak efficiency for any source shape or counting geometry.



### 3.4.3 Additional Derivations

There are several equations above whose derivations are not entirely straightforward. This section is reserved for those derivations. One of these is the determination of the undisturbed path lengths through any absorbing materials necessary in the calculation of the  $F_{att}$  term shown in Equation 3.15. However, if one assumes each absorbing material has a uniform thickness, then these path lengths can be determined from the vector  $\vec{TP}$ .

First, consider the case where the point  $T$  is above the surface of the detector and the point  $P$  is on the top surface of the detector. All of the absorbing materials then, dead-layer, end-cap, etc..., exist above and at greater radii than the active detector volume. This means that each absorbing material can be treated as if it is bounded on the top and bottom by infinite planes parallel to the  $x$ - $y$  plane. Figure 3.8 shows the geometrical setup of this situation.

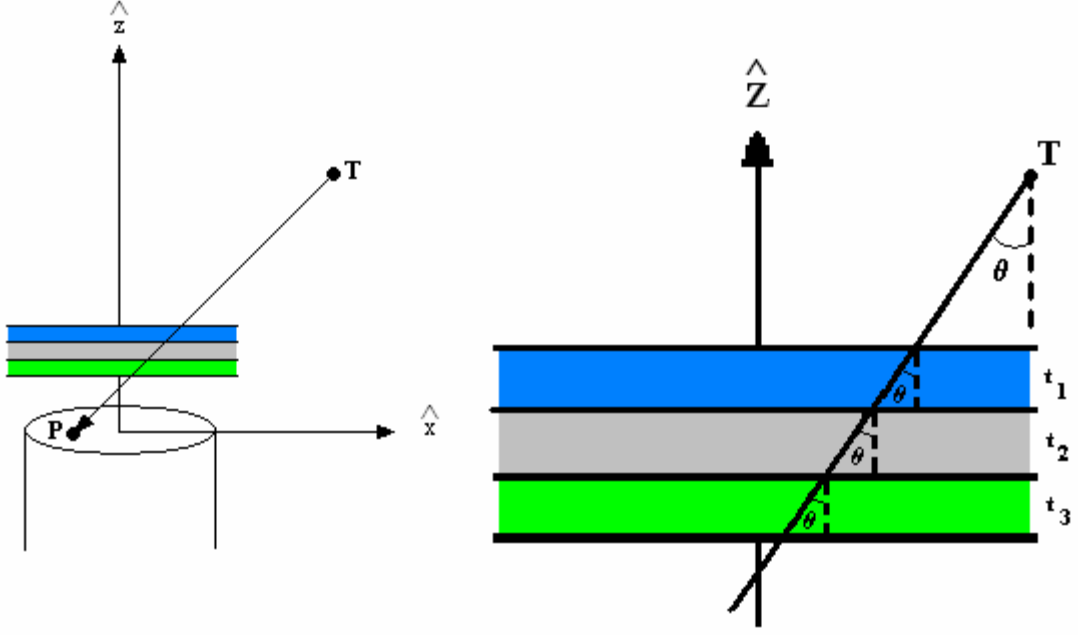


Figure 3.8: Attenuation of Gamma-rays Following Path  $TP$  Through Absorbing Materials Above the Detector Surface.

All of the bounding planes of the absorbing materials are all parallel to each other and the  $x$ - $y$  plane. Unit normals that point in the minus  $z$ -direction can also be constructed for each of the planes. Define an angle  $\theta$  as the angle that the vector  $\vec{TP}$  makes with respect to the minus  $z$ -direction. The angle  $\theta$  takes into account both the  $x$  and  $y$  components of the vector  $\vec{TP}$ . The vector  $\vec{TP}$  therefore makes the same angle  $\theta$  with respect to all of the absorbing surfaces, because the unit normals to the surfaces all point in the minus  $z$ -direction. The path length through the  $i$ th material can then be found using simple trigonometry as shown in Equation 3.25.

$$\delta_i = \frac{t_i}{\cos \theta}. \tag{3.25}$$

Where:  $\delta_i$  is the undisturbed path length through the  $i$ th absorbing material.

$t_i$  is the thickness of the  $i$ th absorbing material.

$\theta$  is the angle between the vector  $\vec{TP}$  and the normals of the absorbing surfaces.

The only unknown on the right hand side of Equation 3.25 is the cosine of the angle  $\theta$ . This can be found taking the dot product of the vector  $\vec{TP}$  with a normal which points in the minus  $z$ -direction. Equation 3.26 shows the dot product of these vectors.

$$\vec{TP} \cdot \vec{n}_{-z} = |\vec{TP}| |\vec{n}_{-z}| \cos \theta = |\vec{TP}| \cos \theta = (z_p - z_T)(\hat{z} \cdot -\hat{z}) = (z_T - z_p). \quad (3.26)$$

Where:  $\vec{TP}$  is the vector that points from point  $T$  to point  $P$  of magnitude  $|\vec{TP}|$ .

$\vec{n}_{-z}$  is a unit normal that points in the minus  $z$ -direction of magnitude 1.

$z_p$  is the  $z$ -coordinate of the point  $P$ .

$z_T$  is the  $z$ -coordinate of the point  $T$ .

In the case where we have placed the origin on the top surface of the detector,  $z_p=0$ . Equation 3.26 can thus be rewritten as Equation 3.27.

$$\cos \theta = \frac{z_T}{|\vec{TP}|}. \quad (3.27)$$

Plugging Equation 3.27 into Equation 3.25 yields Equation 3.28.

$$\delta_i = \frac{t_i |TP|}{z_T}. \quad (3.28)$$

The magnitude  $|TP|$  can be remembered from Equations 3.5 and 3.9 in cylindrical coordinates which allows Equation 3.28 to be rewritten as Equation 3.29. This gives the undisturbed path length through the  $i$ th absorber when the absorbers are placed above the detector.

$$\delta_i = \frac{t_i [R^2 - 2Rr \cos \phi + r^2 + z_T^2]}{z_T}. \quad (3.29)$$

Now consider the case where the point  $T$  is placed to the side of the detector, below the plane of the top detector surface, and above the plane of the bottom of the detector surface. The absorbing materials are still outside of, and have greater radii than, the active detector volume. However, the absorbers in this case cannot be treated as flat parallel planes, because they curve in both the  $x$  and  $y$  directions. They are instead treated as infinite concentric cylinders. The path lengths through these absorbers can be found by calculating the intersections of the vector  $\vec{TP}$  with each of these cylinders. This is very similar to the way that path lengths through the detector are found. The equations necessary for calculating the intersections of a vector with a cylinder are discussed later in this section.

It is not entirely straightforward how Equation 3.16 is obtained either. For this derivation, consider the attenuation of gamma-rays through three different materials. Assume that there is a collimated narrow beam of monoenergetic gamma-rays moving in the  $x$ -direction with a fluence,  $I_0$ , as shown in Figure 3.9. Further assume that there is no build-up resulting from secondary radiation interactions in the materials.

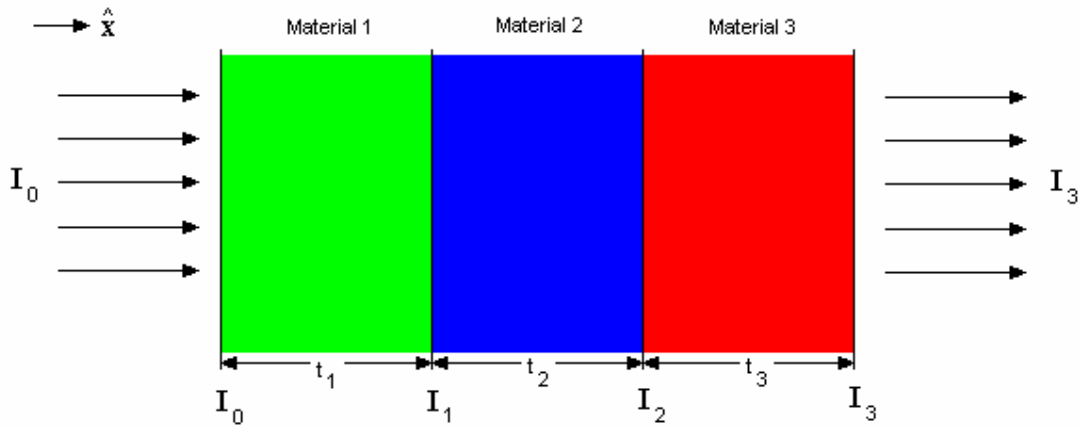


Figure 3.9: Attenuation of Gamma-rays with a Fluence,  $I_0$ , Passing Through Three Different Materials.

The fluences at each interface are the result of simple exponential attenuations of the gamma-rays through each medium (Knoll, 2000). These can easily be found and are shown in Equations 3.30 through 3.32.

$$I_1 = I_0 e^{-\mu_1 t_1} . \quad (3.30)$$

Where:  $I_1$  is the gamma-ray flux at interface 1.

$\mu_1$  is the linear attenuation coefficient of region 1.

$t_1$  is the thickness of material 1.

$$I_2 = I_0 e^{-\mu_1 t_1} e^{-\mu_2 t_2} . \quad (3.31)$$

Where:  $I_2$  is the gamma-ray flux at interface 2.

$\mu_2$  is the linear attenuation coefficient of region 2.

$t_2$  is the thickness of material 2.

$$I_3 = I_0 e^{-\mu_1 t_1} e^{-\mu_2 t_2} e^{-\mu_3 t_3} . \quad (3.32)$$

Where:  $I_3$  is the gamma-ray flux at interface 3.

$\mu_3$  is the linear attenuation coefficient of region 3.

$t_3$  is the thickness of material 3.

The quantity of interest in the  $F_{eff}$  term is the fraction of  $I_0$  that interacted in regions 1 and 3. This is simply Equation 3.33.

$$\left( \frac{I_0}{I_0} - \frac{I_1}{I_0} \right) + \left( \frac{I_2}{I_0} - \frac{I_3}{I_0} \right) = 1 - e^{-\mu_1 t_1} + e^{-\mu_1 t_1} e^{-\mu_2 t_2} - e^{-\mu_1 t_1} e^{-\mu_2 t_2} e^{-\mu_3 t_3} . \quad (3.33)$$

Now assume that materials 1 and 3 are the detector, and that material 2 is the coaxial hole. With these substitutions and a little algebra on Equation 3.33, one can arrive at Equation 3.16. The form of  $F_{eff}$  shown in Equation 3.16 includes attenuation in the coaxial hole. If one assumes that the hole is filled with vacuum, then the linear attenuation coefficient for the coaxial hole is zero. This reduces Equation 3.16 to Equation 3.34. This method can easily be generalized, under the initial assumptions, for gamma-rays passing through any number of absorbing materials.

$$F_{eff} = 1 - e^{-\mu_d \Delta_1} e^{-\mu_d \Delta_2} . \quad (3.34)$$

The intersections of a 3-dimensional line with an infinite cylinder are essential in the calculation of the effective solid angle. Consider a line that passes through two points in Cartesian space, namely  $(x_1, y_1, z_1)$  and  $(x_2, y_2, z_2)$ . An infinite cylinder of radius  $R_0$ , whose primary axis is the  $z$ -axis, can be described by Equation 3.35.

$$x^2 + y^2 - R_0^2 = 0. \quad (3.35)$$

Where:  $R_0$  is the radius of the infinite cylinder.

$x$  is an arbitrary Cartesian  $x$ -coordinate.

$y$  is an arbitrary Cartesian  $y$ -coordinate.

The linear components of the line can be summarized by Equations 3.36, 3.37, and 3.38.

$$x = x_1 + u(x_2 - x_1). \quad (3.36)$$

$$y = y_1 + u(y_2 - y_1). \quad (3.37)$$

$$z = z_1 + u(z_2 - z_1). \quad (3.38)$$

Where:  $u$  is the 3-dimensional analogue of the slope of the line.

$z$  is an arbitrary Cartesian  $z$ -coordinate.

The intersections of the line and cylinder can be found by plugging Equations 3.36 and 3.37 into Equation 3.35 to yield Equation 3.39.

$$\left[ (x_2 - x_1)^2 + (y_2 - y_1)^2 \right] u^2 + [2(x_2 - x_1)x_1 + 2(y_2 - y_1)y_1]u + [x_1^2 + y_1^2 - R_0^2] = 0. \quad (3.39)$$

This is easily recognized as a quadratic equation which can be solved, using the quadratic formula. The two roots of  $u$  can then be plugged back into Equations 3.36, 3.37, and 3.38 to solve for the two intersections.

The final calculation that is important in the determination of the effective solid angle is the intersection of a line with a plane. The equations describing a line in 3-dimensional Cartesian space have already been given as Equations 3.36, 3.37, and 3.38. The most common plane of interest in calculations of effective solid angles is a plane parallel to the  $x$ - $y$  plane. The equation for such a plane intersecting the  $z$ -axis at  $A$  is shown in Equation 3.40.

$$z - A = 0. \quad (3.40)$$

Inserting Equation 3.38 into 3.40 and solving for  $u$  yields Equation 3.41.

$$u = \frac{A - z_1}{z_2 - z_1}. \quad (3.41)$$

Equation 3.41 can be plugged back into Equations 3.36, 3.37, and 3.38 to yield the intersections.



### 3.4.4 Uncertainties

Uncertainties in the mesh-grid method can arise from several different factors. It is important to know each detector specification to a high degree of certainty, because the mesh-grid method uses these values in its effective solid angle calculations. For example, the detector dead layer thickness will be important because it will greatly affect gamma-ray attenuation at low photon energies. However, because the equations use a ratio form, the mesh-grid method should be less sensitive to uncertainties in detector specifications than Monte Carlo methods.

The counting geometry parameters, such as distance from the source to detector, and source shape, should also be known to within a high degree of certainty. With current technology, these factors can be experimentally measured to a high degree of certainty. The source composition (matrix) will need to be known well in order to properly correct for source self-absorption. The gamma-ray attenuation cross-sections should be well known, as they will highly affect both  $F_{att}$  and  $F_{eff}$  terms.

Because this method uses an experimentally obtained reference efficiency curve, any uncertainty in that measured curve will be reflected directly in the calculated efficiency curve. Thus, the reference curve should be measured using NIST traceable, or similar quality, sources with small uncertainties in their known activity. Corrections for experimentally observed summing effects or dead time should be performed when necessary. The measurements should be taken carefully in order to yield results that produce high experimental precision and accuracy to a high degree of confidence.

The equation used to calculate the full-energy peak efficiency was given in Equation 3.14. The uncertainty in the predicted efficiency can be found, using the rules for the multiplication and division of uncertainties, and is shown in Equation 3.42.

$$\frac{\sigma_{e,X}}{\varepsilon_X} = \sqrt{\left(\frac{\sigma_{e,ref}}{\varepsilon_{ref}}\right)^2 + \left(\frac{\sigma_{\Omega,X}}{\Omega_X}\right)^2 + \left(\frac{\sigma_{\Omega,ref}}{\Omega_{ref}}\right)^2}. \quad (3.42)$$

Where:  $\sigma_{e,X}$  is the expected uncertainty in the predicted full-energy peak efficiency.

$\varepsilon_X$  is the predicted full-energy peak efficiency.

$\sigma_{e,ref}$  is the uncertainty in the experimentally measured reference efficiency.

$\varepsilon_{ref}$  is the experimentally measured reference efficiency.

$\sigma_{\Omega,X}$  is the uncertainty in the calculated effective solid angle of the desired geometry.

$\Omega_X$  is the effective solid angle of the desired geometry.

$\sigma_{\Omega,ref}$  is the uncertainty in the calculated effective solid angle of the experimentally measured reference geometry.

$\Omega_{ref}$  is the effective solid angle of the reference geometry.

It should be expected that the dominating term in Equation 3.42 will be the uncertainty in the experimentally measured reference efficiency. However, that uncertainty should also be small if it is the result of a meticulously performed experimental efficiency calibration. The other two terms, the effective solid angle uncertainties, should contain the uncertainties in all of the necessary dimensions, geometrical setup, and constants. The uncertainty in an effective solid angle calculation can be expressed as some complicated function of several variables as shown in Equation 3.43.

$$\frac{\sigma_{\Omega}}{\Omega} = f\left(\frac{\sigma_{\mu,i}}{\mu_i}, \frac{\sigma_{\delta,i}}{\delta_i}, \frac{\sigma_{d,i}}{d_i}, \frac{\sigma_{\Delta,i}}{\Delta_i}, \frac{\sigma_{g,i}}{g_i}\right). \quad (3.43)$$

Where:  $\sigma_{\Omega}$  is the uncertainty in an effective solid angle calculation.

$\Omega$  is the effective solid angle.

$f$  is a function that describes the relationships of the uncertainties.

$\sigma_{\mu,i}$  is the uncertainty in the  $i$ th attenuation coefficient.

$\mu_i$  is the  $i$ th attenuation coefficient.

$\sigma_{\delta,i}$  is the uncertainty in the  $i$ th absorber path length.

$\delta_i$  is the  $i$ th absorber path length.

$\sigma_{d,i}$  is the uncertainty in the  $i$ th detector dimension.

$d_i$  is the  $i$ th detector dimension.

$\sigma_{\Delta,i}$  is the uncertainty in the  $i$ th detector path length.

$\Delta_i$  is the  $i$ th detector path length.

$\sigma_{g,i}$  is the uncertainty in the  $i$ th geometry setup parameter.

$g_i$  is the  $i$ th geometry setup parameter.

The detector dimension parameter used in Equation 3.43 should take into account things like the detector diameter, length, dead-layer, etc... The geometry setup parameter should take into account things like the source-to-detector distance, absorber thickness, etc... Because the uncertainty in the effective solid angle is not a simple function of its variables, the use of partial derivatives is essential. Underlying this use is the assumption that the parameters are independent variables. This is justified because, for example, the measurement of the detector diameter should have no dependence on a separate measurement of a gamma-ray attenuation coefficient. Arguments for the independence

of all the parameters from each other can similarly be made. The effective solid angle function shown in Equation 3.22 is thus partially differentiated with respect to each of the parameters. Estimates of the parameter uncertainties are then used to yield the combined effective solid angle uncertainty as shown in Equation 3.44. These partials are summarized in this shorthand notation, because the derivatives are often excessively complicated and some need to be differentiated numerically.

$$\sigma_{\Omega} = \sqrt{\left(\frac{\partial\Omega}{\partial\mu_i}\right)^2 d\mu_i^2 + \left(\frac{\partial\Omega}{\partial\delta_i}\right)^2 d\delta_i^2 + \dots + \left(\frac{\partial\Omega}{\partial\Delta_i}\right)^2 d\Delta_i^2}. \quad (3.44)$$

Where:  $\Omega$  is the effective solid angle function.

$d\mu_i$  is the estimated error in the  $i$ th attenuation coefficient.

$d\delta_i$  is the estimated error in the  $i$ th absorber path length.

$d\Delta_i$  is the estimated error in the  $i$ th detector path length.

### 3.5 MONTE CARLO

Some of the validation of the mesh-grid assumptions could not easily be performed using experimental or theoretical methods. Therefore Monte Carlo methods were invoked in several cases to justify these assumptions. This purpose of this section is only to familiarize the reader with the basics of Monte Carlo calculations. For a more detailed description of code functionality, or Monte Carlo methods in general, consult the code user manuals or other literature (Jackman, 2004).

Monte Carlo calculations of radiation transport assume that radiation can be treated as stochastic in nature. Because of this, the primary uncertainties that arise are

themselves stochastic. This means that often the method must be used for a large number of particles in order to produce acceptable uncertainty. This can generate a non-trivial amount of computational time, even on a modern PC (Jackman, 2004).

Particle tracks and histories are generated by simulating the random nature of particle interactions in matter. A particle's history is created using probability expressions that describe the particle's most likely interaction types and track lengths. Each particle is initially given a path length, energy, and direction. Once the particle arrives at its destination, the next path length, direction, energy lost, and interaction type are computed using probability. The probabilities are assigned using random or pseudorandom number generators. This process is repeated until the particle loses all of its kinetic energy or escapes the tracking "world" (Shultis *et al.*, 2000).

The two Monte Carlo codes used in this work were MCNP version 5 and GEANT version 4. Each code has their unique advantages and disadvantages, but the main point is that both use the Monte Carlo method. The MCNP (Monte Carlo N-Particle) transport code was developed by Los Alamos National Laboratory and is distributed through the Radiation Safety Information Computation Center at Oak Ridge National Laboratory. GEANT is the European equivalent of MCNP, but is open source and distributed by the Conseil Européen pour la Recherche Nucléaire (CERN). GEANT was primarily designed for high-energy physics and particle accelerators, but has since been adapted to handle almost all types of physics interactions.

## **Chapter 4: KMESS Code Description**

### **4.1 KMESS CODE FORMAT**

#### **4.1.1 Overview of the Code**

KMESS was developed as the computational realization of the mesh-grid method. Its function is to try to simulate, or predict, the full-energy peak efficiencies of a germanium detector. It does so using the basic detector data supplied by the manufacturers and one experimentally measured reference curve. It can predict efficiencies for arbitrary source shapes and counting geometries. As will be shown, if used properly, it can predict these efficiencies quite well.

The main KMESS code was written in the C language. It was coded in this language for two basic reasons, the primary being that writing codes in programming languages closer to machine code tends to allow faster program execution and thus quicker run times. The other reason is so that future generations will be able to easily debug and understand the code.

KMESS, as a stand alone code, is intended to be operated at the command line and uses flags and arguments to control its execution. Descriptions of the various flags and run methods are included in Appendix A.1.1. The code was intended to be compiled and built using the GNU GCC compiler. A “Makefile” was written to accompany the source code so that it can be easily compiled and built using the GNU Make tool. Figure 4.1 shows a brief flow chart of how KMESS runs.

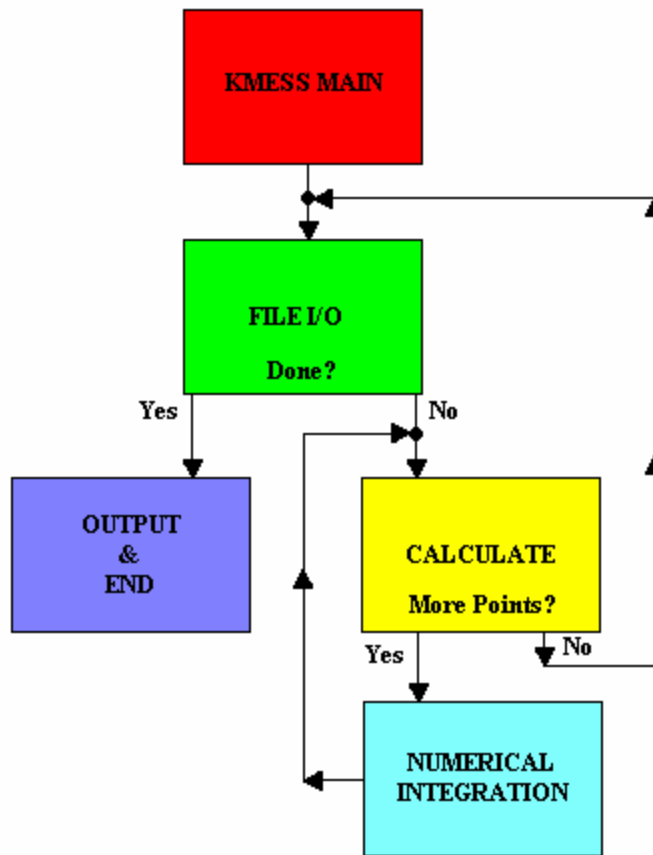


Figure 4.1: Flow Chart for KMESS Code Execution.

Command line execution is not desirable to most modern computer users, who instead prefer a graphical interaction with programs. As a result of this, concurrent with KMESS development, a graphical web interface to KMESS was coded in PHP and JavaScript. This choice of web programming allows the code to be executed across multiple operating system platforms. This also allows the user to have a graphical interaction in controlling KMESS execution through any modern web browser.

KMESS and its graphical web front-end were written to easily interface with the current C-NR group's counting room gamma-ray analysis software at Los Alamos

National Laboratory. That analysis software is often called the Next Generation Web (NGWeb). The NGWeb is a suite of gamma-ray spectroscopy tools that competes with currently available commercial codes, but is distributed open-source under the GPL. Therefore, KMESS was also written with the intent of open-source distribution under the GPL. Figure 4.2 shows the current way that KMESS is intended to be interfaced with the current counting room software.

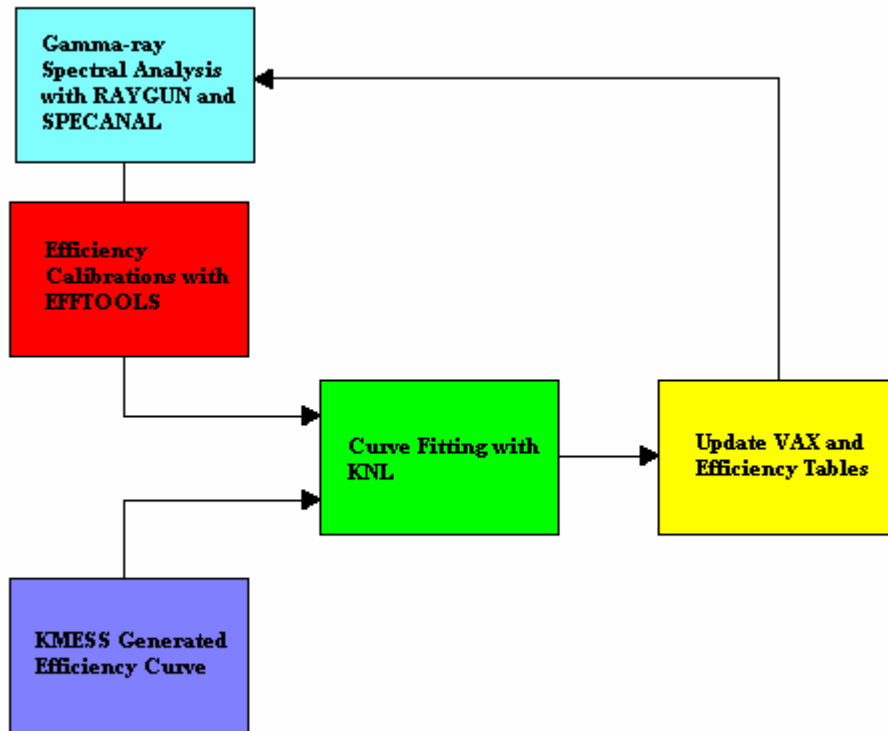


Figure 4.2: How KMESS Fits Into the Current NGWeb Analysis System.



The current numerical integration routine in KMESS uses Romberg integration. For a full description of the Romberg integration procedure, one can consult most common math books on the subject (Press *et al.*, 1990). The numerical integration routines were written separately from the routines that describe the effective solid angle terms. This allows one to easily incorporate various other integration methods, such as Monte Carlo or Gauss-Legendre quadrature, in the calculation of the effective solid angles.

#### **4.1.2 Code Defaults and Limitations**

There are some limitations and defaults in the code that deserve some attention. These can be discovered upon inspection of the source code, but it is better to just mention them here. The first limitation in KMESS is that the code can currently only read the file formats that were developed alongside the code. These files have a keyword-value format to increase readability and ease white space parsing. Descriptions of each allowed file format and keyword are included in Appendix A.1.

Another limitation in the code is that it will not calculate effective solid angles for sources placed below the bottom of the active detector crystal. This is because there is no generally used mounting configuration across different brands of germanium detectors. These mounting mechanisms are often complicated and intricate as well. There was also little need to calculate effective solid angles for sources placed behind the detector.

Many of the detector manufacturers do not provide some of the important detector parameters, such as coaxial hole dimensions, on their specification sheets. These dimensions can usually be obtained by contacting the manufacturer unless the detector is old. To address this, some defaults for germanium detectors needed to be set in KMESS. One of these was the coaxial hole dimensions. Across the coaxial detectors used in the

counting room at LANL, most have a 10 mm diameter coaxial hole. The true coaxial detectors have a depth equal to the length of the crystal, but the closed-ended detectors have a coaxial depth that is around  $\frac{3}{4}$  of the length of the crystal. Therefore, those were set as the defaults. Other detector defaults can be found in the descriptions of the KMESS Detector File (KDF) format in Appendix A.1.4.

## **4.2 KMESS FEATURES**

### **4.2.1 Currently Included**

KMESS currently has several features that can influence its effective solid angle calculations. The code can perform attenuation in both the source and absorber materials placed between the source and active detector crystal. However, the current routines that perform each of these calculations have limited usefulness.

The absorber functionality is currently limited to handle only one absorber. This absorber is specified with a KMESS Absorber File (KAF). The currently allowed KAF format is described in Appendix A.1.2, but only the absorber thickness can be specified in the current format. The absorber is assumed to be uniformly distributed over the detector end-cap. By doing this, the absorber is used for all calculations of the effective solid angle. There is also currently only a limited selection of absorbing materials allowed.

Source self-attenuation can be included in KMESS calculations. The current routine can only approximate the path length through the source. This was done because there is no blanket geometrical parameterization that can be applied to describe arbitrary source shapes. The path length is assumed to be the distance between the current mesh point and some other point in the mesh. The second, or end, mesh point is the one

furthest out in the source mesh and closest to the gamma-ray path. Unfortunately, the routine that finds these source path lengths increases the KMESS run times by a factor of 5 or more. This approximation makes the source self-attenuation calculations more valid for larger collections of point sources. However, it also has the consequence that larger collections of point sources take longer for KMESS to find the correct source path lengths.

The KMESS source description are sets of  $(x, y, z)$  coordinates that describe a source mesh. These coordinates describe the placement of the source points relative to the center of the detector end-cap top. This allows arbitrary source shapes to be described as collections of point sources placed almost anywhere around the detector. The source is input using the KMESS Source File (KSF) format. The currently allowed KSF format is described in Appendix A.1.6. However, the web interface was designed with a conversion tool to allow conversion of commonly used mesh formats, such as GAMBIT, FLUENT, and OpenFOAM, to the KSF format.

Another feature included in KMESS is the ability to weight source mesh points relative to other points in the mesh. This is useful if the distribution of radionuclides in the source is known. This allows for correction of radionuclide inhomogeneity within the source. The weighting factors are input with the source coordinates in the KSF file. The weighting factors of all points should be normalized to 1. The weighting factors are used in the determination of the average effective solid angle as shown in Equation 3.23.

#### **4.2.2 Future Additions**

Future additions to KMESS could improve its ability to predict full-energy peak efficiencies of germanium detectors in a shorter amount of time. Improvements could be made to the source self-attenuation calculations by instead using some sort of polynomial

fit to the external points in the source mesh. This would allow more rapid determination of gamma-ray path lengths through the source. Routines could be written that better describe radionuclide inhomogeneity in the source. These could be just simple routines that describe the source distribution using standard ones, like Gaussian or log-normal. Additional numerical integration engines can be written to improve the speed and accuracy of the effective solid angle calculations. These could incorporate other numerical integration methods such as Monte Carlo or Gauss-Legendre quadrature. Coincidence summing correction routines could also be written to correct the experimentally measured reference curves for those effects. Additional materials could also be added for use as KMESS absorbers or sources. A procedure on how to do this is described in the KMESS Cross-section File (KCF) format guidelines found in Appendix A.1.3. Finally, improvements could be made to KMESS to allow input of additional file formats such as those used by SYNTH, LabSOCS, or other mesh formats.

KMESS could also be easily coupled to a 3D scanner. These scanners typically photograph an object from different angles to produce a 3D computer-aided design (CAD) drawing. The CAD drawing could then be meshed and used as the input for KMESS. This would make producing full-energy peak efficiencies for exotic source shapes quick and easy.

## Chapter 5: Results and Discussion

### 5.1 VALIDATION OF MODEL ASSUMPTIONS

#### 5.1.1 Invariance of Virtual Peak-to-Total Ratio

One primary assumption in the Moens method of effective solid angle calculations is the invariance of the “virtual” peak-to-total ratio. As aforementioned, this ratio refers to a hypothetical bare and isolated detector crystal. Scattering in nearby materials are ignored because they reach the detector with degraded energy. The photons thus contribute to the total area of the spectrum, rather than depositing their full-energy. The initial Moens justification of this invariance was confined to sources in the region above the detector surface and at a radial distance from the  $z$ -axis less than the radius of the detector.

Any change in the amount of active detector material a photon would pass through should be expected to change the virtual peak-to-total ratio. The invariance assumption is supported primarily because the detector is the same for both the desired and reference counting geometries. It is further justified if the reference source is counted under similar conditions to the desired geometry.

In order to validate this invariance, the peak-to-total ratios of a bare isolated crystal in a vacuum were computed using GEANT4. The crystal had a diameter of 59.8 mm and a length of 59.6 mm in the simulations. The crystal was also assumed to have no coaxial hole. Three sets of simulations were conducted for isotropic point sources at twelve different energies corresponding to on-axis, 45 degrees, and 90 degrees source placements. The angles were measured relative to the center of the detector crystal and from the detector primary axis. The source-to-detector distances for each of the three

source placement were allowed to vary to 0, 5, and 10 cm. These source-to-detector distances were measured along a vector pointing in the direction of the given angle, to the intersection of that vector with the outer crystal surface. Tables 5.1, 5.2, and 5.3 show the compiled results and standard deviations of the peak-to-total ratios for these three sets of simulations.

Table 5.1: Results of Peak-to-Total Ratio Simulations for a Source-to-Detector Distance of 0 cm for Three Different Angular Source Placements.

<b>Energy</b>	<b>on-axis</b>	<b>45 deg</b>	<b>90 deg</b>	<b>Standard</b>
<b>[keV]</b>	<b>Peak-to-Total Ratio</b>	<b>Peak-to-Total Ratio</b>	<b>Peak-to-Total Ratio</b>	<b>Deviation [%]</b>
59.54	0.96	0.94	0.96	1.6
88.04	0.95	0.92	0.95	2.1
122.06	0.92	0.86	0.91	3.7
165.86	0.83	0.75	0.82	5.4
279.20	0.57	0.50	0.56	7.3
391.69	0.43	0.37	0.41	8.1
514.00	0.34	0.29	0.33	8.4
661.66	0.27	0.23	0.27	8.5
896.04	0.22	0.19	0.22	8.7
1173.24	0.18	0.16	0.18	8.7
1332.50	0.17	0.14	0.16	8.5
1836.04	0.13	0.11	0.13	8.3

Table 5.2: Results of Peak-to-Total Ratio Simulations for a Source-to-Detector Distance of 5 cm for Three Different Angular Source Placements.

<b>Energy</b>	<b>on-axis</b>	<b>45 deg</b>	<b>90 deg</b>	<b>Standard</b>
<b>[keV]</b>	<b>Peak-to-Total Ratio</b>	<b>Peak-to-Total Ratio</b>	<b>Peak-to-Total Ratio</b>	<b>Deviation [%]</b>
59.54	0.98	0.97	0.98	0.5
88.04	0.97	0.96	0.97	0.6
122.06	0.93	0.91	0.92	0.9
165.86	0.83	0.81	0.83	1.0
279.20	0.57	0.56	0.57	1.2
391.69	0.42	0.42	0.42	1.1
514.00	0.34	0.33	0.34	1.0
661.66	0.27	0.27	0.28	1.1
898.04	0.22	0.22	0.22	1.2
1173.24	0.19	0.18	0.19	0.7
1332.50	0.17	0.17	0.17	0.7
1836.04	0.14	0.13	0.14	0.5

Table 5.3: Results of Peak-to-Total Ratio Simulations for a Source-to-Detector Distance of 10 cm for Three Different Angular Source Placements.

<b>Energy</b>	<b>on-axis</b>	<b>45 deg</b>	<b>90 deg</b>	<b>Standard</b>
<b>[keV]</b>	<b>Peak-to-Total Ratio</b>	<b>Peak-to-Total Ratio</b>	<b>Peak-to-Total Ratio</b>	<b>Deviation [%]</b>
59.54	0.98	0.98	0.98	0.5
88.04	0.97	0.96	0.97	0.6
122.06	0.93	0.91	0.92	0.8
165.86	0.84	0.82	0.83	1.2
279.20	0.58	0.56	0.58	1.6
391.69	0.43	0.42	0.43	1.7
514.00	0.34	0.33	0.34	1.6
661.66	0.28	0.27	0.28	1.7
898.04	0.23	0.22	0.22	1.5
1173.24	0.19	0.18	0.19	1.3
1332.50	0.17	0.17	0.17	1.3
1836.04	0.14	0.13	0.14	1.0

Upon inspection of Tables 5.1 through 5.3, it is evident that the peak-to-total ratios do not vary significantly with angle, at fixed distances, except when the source is placed close to the detector and the gamma-ray energy is high. However, the point source at 0 cm and 45 degrees is skewing the standard deviations. Because the cylinder is not exactly a right circular cylinder, this point is actually located on the top of the detector and just inside its radius. Gamma-rays traveling down and radially outward from this point will only travel through a small amount of detector material. This discrepancy may be attributed to the fact that high energy gamma-rays have a small probability of totally depositing their full-energy in that small amount of detector material. Thus, the higher energy gamma-rays will then tend to contribute more to the total continuum rather than the peak. This results in the reduction of the peak-to-total ratio for high energy gamma-rays as seen for that case. The standard deviations of the peak-to-total ratios for fixed angles and varying distances are shown in Table 5.4.

Table 5.4: Variation of Peak-to-Total Ratio Simulations for Three Fixed Angular Source Placements and Source-to-Detector Distances Varying as 0, 5, and 10 cm.

	<b>on-axis</b>	<b>45 deg</b>	<b>90 deg</b>
<b>Energy</b>	<b>Standard</b>	<b>Standard</b>	<b>Standard</b>
<b>[keV]</b>	<b>Deviation (%)</b>	<b>Deviation (%)</b>	<b>Deviation (%)</b>
59.54	1.1	2.2	1.0
88.04	0.9	2.4	0.9
122.06	0.7	3.7	1.0
165.86	0.5	4.9	1.1
279.20	0.5	6.6	1.3
391.69	0.8	7.5	1.6
514.00	1.0	8.1	1.6
661.66	1.0	8.1	1.4
898.04	1.0	8.5	1.8
1173.24	1.0	8.9	1.7
1332.50	1.1	8.8	2.1
1836.04	1.3	9.1	2.3



As shown in Table 5.4, the ratios do not vary significantly with distance at fixed angles, except when the angle is 45 degrees and the gamma-ray energy is higher. This is also because the point source at 0 cm and 45 degrees is skewing that standard deviation. By similar reasoning to that above, this peak-to-total ratio in that case is smaller. This variation is not seen in the other 45 degrees cases, because gamma-rays are more likely to travel through a larger amount of detector material and deposit their full-energy. However, all of the peak-to-total ratios agree to within less than 10%.

The bare crystal used in the GEANT4 simulations is nearly a right circular cylinder. For detector crystals whose dimensions vary significantly from this, the virtual peak-to-total ratio should be expected to change when the source is moved to other positions around the detector. As proof of this, consider the cases of a large thin disc detector and a long cylinder detector with a small radius. In the case of the large thin disc detector, gamma-rays will have a greater chance of depositing their full-energy when they enter the crystal from the side. Similarly, gamma-rays entering the long cylinder detector will have a greater chance of depositing their full-energy when they enter the crystal from the top. Because of this, the reference source used in an effective solid angle calculation of the full-energy peak efficiency should be placed in as similar location as possible to the geometry of the desired efficiency. Following this guideline will tend to preserve the invariance of the “virtual” peak-to-total ratio. Large differences between the reference and desired geometrical counting setups will tend to break this preservation, and will reduce the validity of the predicted efficiency curve.

Experimentally measured peak-to-total ratios should be expected to depend on the counting geometry. This is because the photons will scatter off nearby materials and reach the detector with degraded energy. This assumption was tested experimentally using an HPGe detector and a Canberra S-PTC source calibration set. The sources were

placed on-axis at distances of 0, 4, 8, and 10 cm. The results of these measurements are compiled in Table 5.5.

Table 5.5: Experimentally Measured Peak-to-Total Ratios for On-axis Sources at Distances of 0, 1, 4, and 10 cm.

Energy	0 cm	4 cm	8 cm	10 cm	Standard
[keV]	Peak-to-Total Ratio	Peak-to-Total Ratio	Peak-to-Total Ratio	Peak-to-Total Ratio	Deviation [%]
59.54	0.33	0.37	0.37	0.34	7.1
88.04	0.53	0.55	0.53	0.49	4.7
122.06	0.59	0.59	0.57	0.53	5.4
391.69	0.33	0.33	0.32	0.31	3.6
661.66	0.22	0.22	0.22	0.21	2.6
834.85	0.19	0.19	0.19	0.18	2.2
1115.55	0.16	0.16	0.16	0.16	1.3

As expected the peak-to-total ratios do differ, however slightly, with varying counting geometry. This difference can primarily be attributed to the differing amounts of gamma-ray scattering on near detector materials. Attempts were made to measure the experimental peak-to-total ratios of off-axis sources. However, the number of available sources with high enough activity inhibited these measurements.

### 5.1.2 Detector Approximated as a Cylinder

In calculations of the effective solid angle, the active detector region is parameterized as a cylinder. The coaxial hole in the detector is also parameterized as a cylinder. In reality however, germanium detectors are typically manufactured as bulletized crystals as shown in Figure 3.2. This is done to improve the charge collection characteristics of the detector. The coaxial hole is also typically rounded off at the tip as well. In an effort to justify this assumption, MCNP5 was used to compare the efficiency curves produced from two different detector models. One detector model treated the

detector and coaxial hole as cylinders. The other model took into account the bulletization of the detector crystal, and the rounding of the tip of the coaxial hole. Pictures of the two different MCNP5 models are shown in Figures 5.1 and 5.2.

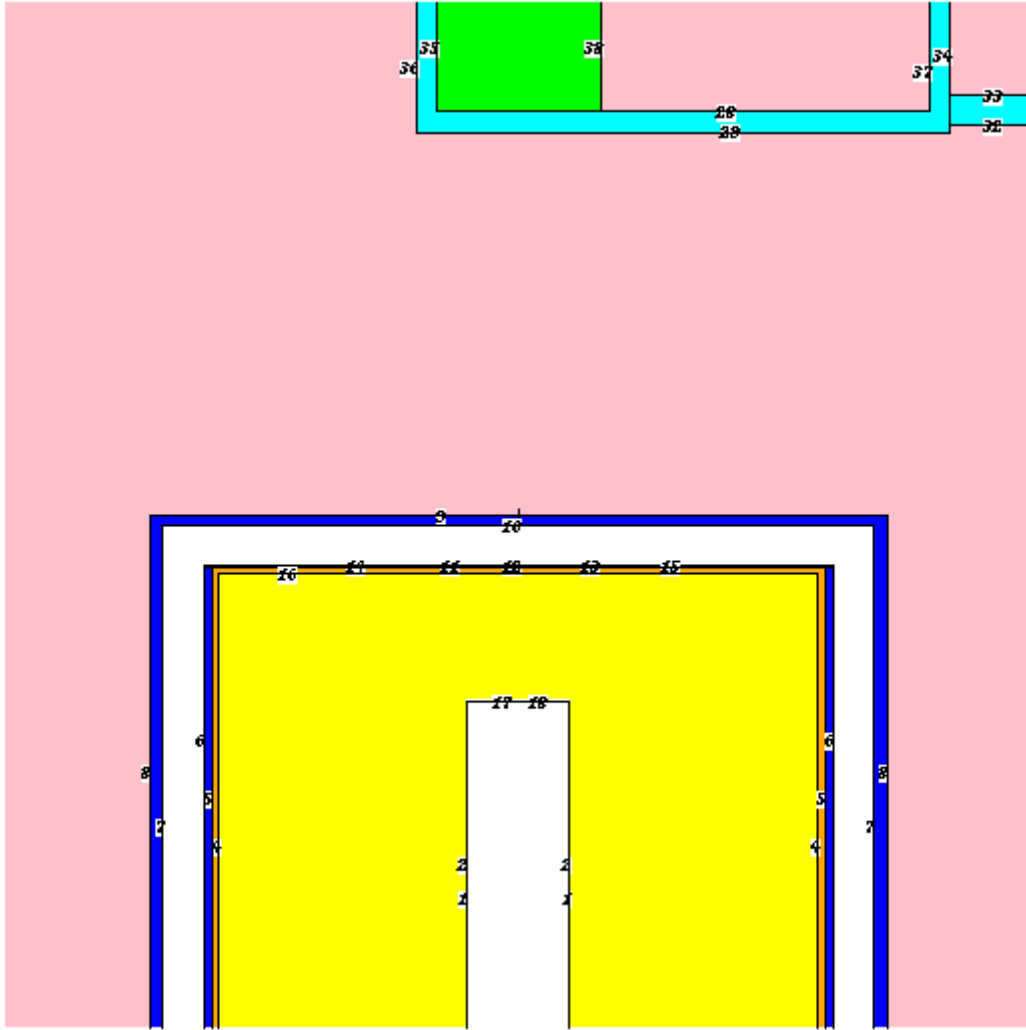


Figure 5.1: Picture of MCNP5 Model with the Detector Crystal and Coaxial Hole Approximated as Cylinders.

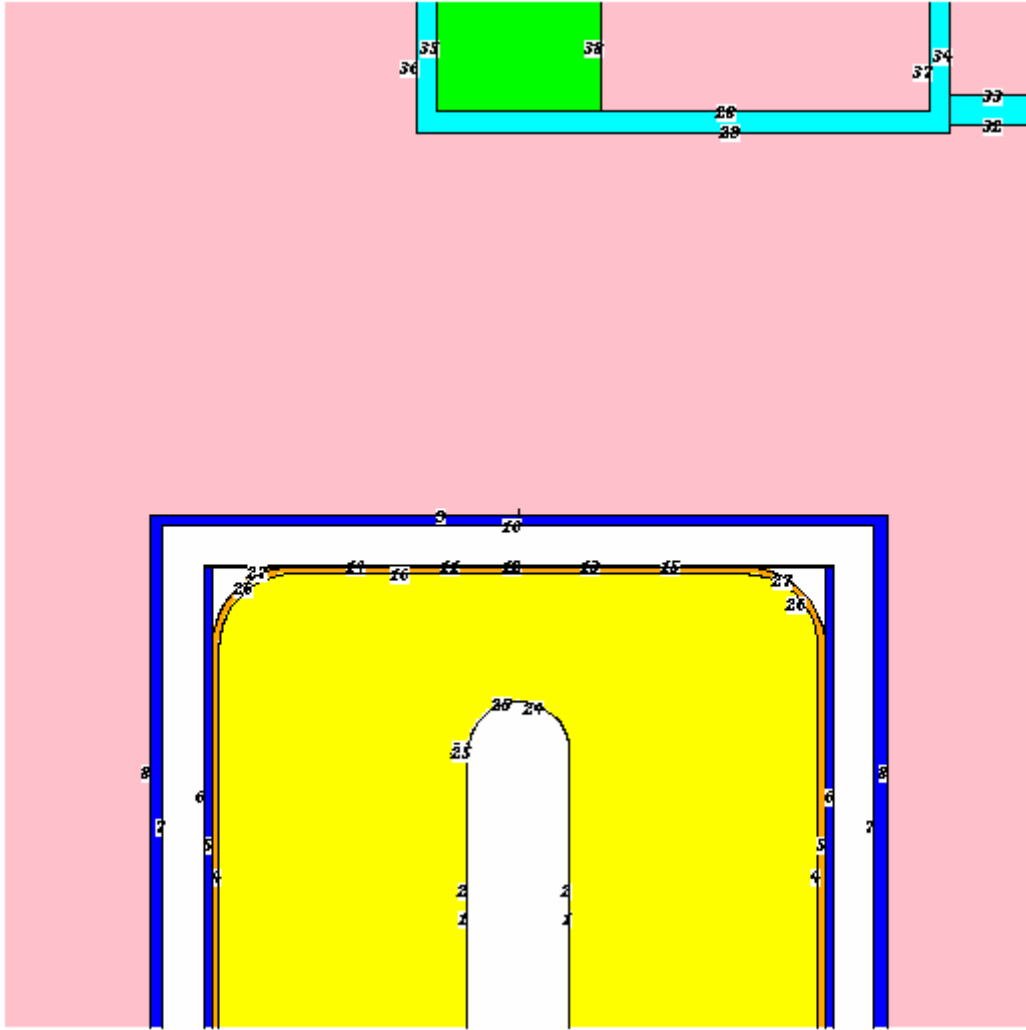


Figure 5.2: Picture of MCNP5 Model that Includes the Detector Crystal and Coaxial Hole Bulletization.

Both models simulated a mixed radionuclide source placed in a plastic liquid scintillation vial for 11 different gamma-ray energies. Simulations were run for both models with the source placed on-axis at source-to-detector distances of 0, 1, 2, 3, 4, 5, 6, and 12 inches. The efficiencies from the simulations were then computed. The differences observed between the two models are compiled in Tables 5.6 and 5.7. The two models are henceforth called the cylinder model and the bullet model in order to differentiate between the two.

Table 5.6: Percent Differences Between the Cylinder and Bullet MCNP5 Models at Source-to-Detector Distances of 0, 1, 2, and 3 inches.

<b>ENERGY</b>	<b>0" Percent Peak</b>	<b>1" Percent Peak</b>	<b>2" Percent Peak</b>	<b>3" Percent Peak</b>
<b>[keV]</b>	<b>Efficiency Difference</b>	<b>Efficiency Difference</b>	<b>Efficiency Difference</b>	<b>Efficiency Difference</b>
59.54	10.7	14.1	14.0	14.2
88.04	8.6	10.2	9.4	9.8
122.06	5.9	6.4	5.7	6.8
165.86	4.0	4.1	3.4	4.6
279.20	2.4	2.2	1.5	3.0
391.69	2.0	1.7	0.8	2.6
661.66	1.6	1.0	0.5	2.0
898.04	1.3	0.8	0.2	1.8
1173.24	1.2	0.8	0.0	1.8
1332.50	1.3	0.8	-0.2	1.6
1836.06	1.1	0.6	-0.2	1.5

Table 5.7: Percent Differences Between the Cylinder and Bullet MCNP5 Models at Source-to-Detector Distances of 4, 5, 6, and 12 inches.

<b>ENERGY</b>	<b>4" Percent Peak</b>	<b>5" Percent Peak</b>	<b>6" Percent Peak</b>	<b>12" Percent Peak</b>
<b>[keV]</b>	<b>Efficiency Difference</b>	<b>Efficiency Difference</b>	<b>Efficiency Difference</b>	<b>Efficiency Difference</b>
59.54	12.4	11.9	10.5	6.4
88.04	7.8	7.7	7.2	3.2
122.06	5.0	5.1	4.4	1.9
165.86	3.6	3.7	3.7	1.5
279.20	2.1	2.5	2.3	0.4
391.69	1.6	2.0	1.9	0.2
661.66	1.3	1.9	0.7	-0.4
898.04	1.1	1.4	1.5	-0.1
1173.24	0.9	1.5	1.6	-0.3
1332.50	0.8	1.0	1.5	0.1
1836.06	0.7	1.2	1.2	-0.5

The models both agree well with each other for gamma-rays with energies greater than about 100 keV. For gamma-rays with energies below that threshold, the amount of variation increases significantly. One important thing not shown in the tables is that the percent differences were calculated relative to the cylinder model. Most of the percent differences in the tables are positive, indicating that the efficiencies of the cylinder model were typically greater than the efficiencies of the bullet model.

Disagreement at low energy may primarily be caused by the loss of the detector cylinder corners. Low energy photons typically deposit their full-energy within the first few millimeters of the active crystal. A reduction in the amount of active material presented to the low-energy gamma-rays in these first few millimeters, would therefore lower the efficiency. However, this did not affect higher energy gamma-rays traveling through the detector corners. This is because high energy gamma-rays have a low probability of depositing their full-energy in that small amount of active material. Thus, rounding off the corners of the detector should tend to reduce the number of high energy gamma-rays that only partially deposit energy. This, however, does not significantly reduce the number of high energy gamma-rays that deposit their full-energy under the peak. This means that effective solid angle calculations are more valid for energies above 100 keV. Care should therefore be taken in using the mesh-grid method for energies much below that threshold. The discrepancy may also mean that MCNP has poor cross-section data or does not properly treat the physics.

The rounding of the coaxial hole has the effect of adding back a small amount of active material. This should tend to increase the number of events that occur in the detector, because there is a larger active detector volume. However, the amount of active material added back in these simulations was small. Therefore, it does not appear to significantly affect the detector efficiency.

### 5.1.3 Coaxial Hole Considerations

Initially, it was the intent of the mesh-grid method to treat a detector as a true cylinder detector minus a “coaxial hole” detector. The amount of energy deposited in the real detector would be then have been calculated from the amount deposited in the true cylinder minus the amount deposited in the coaxial hole detector. This is similar to the assumption made in other work (Ugletveit *et al.*, 1989). The advantage to this method is that the path length calculations in the detector, necessary for the determination of the  $F_{eff}$  term in the effective solid angle equation, would be much easier.

This assumption was quickly abandoned in favor of using logical loops to determine the path lengths through the detector. In this case, there is no need to justify the true cylinder minus the coaxial hole detector assumption. The path lengths through the detector and coaxial hole are directly determined using the intersections of the gamma-ray path with important detector cylinders and planes.

The assumption was abandoned for three reasons. First, the determination of the path lengths through the detector and coaxial hole required only a minimal amount of extra work to use logical loops. Second, the assumption proved difficult to justify. The primary avenue explored in this justification was the use of Monte Carlo methods. The simulations of the coaxial hole detector required a significant amount, on the order of weeks, of computation time to produce enough statistics to justify only one geometrical counting setup. Last, the assumption requires numerical integration of the effective solid angle equations twice. This means that for each effective solid angle calculation, the amount of work done by the computer is essentially doubled. Thus, using logical loops takes a small amount of extra work during the integration process, but the overall runtime of the code is less.



#### **5.1.4 Weighting Factors and Homogeneity**

The exact distribution of radionuclides within a source is rarely ever known. Because of this, the calculations performed here all assumed that the radionuclides were distributed homogeneously in the source. This is a good assumption for point sources, because they only have one place to exist, namely the point. For all of the simulations and experiments involving volumetric sources, the radionuclides were treated as being suspended in 4M HCl. This strong acid tends to help distribute the radionuclides homogeneously within the solution. Aside from painfully difficult experiments to attempt to prove this assumption, this assumption was taken *a priori*. The KMESS code and the mesh-grid model allow for the introduction of weighting factors in the averaging of the point source efficiencies. This allows one to correct for source inhomogeneity, if the source distribution happens to be known. All of the weighting factors were fixed to 1 for all of the effective solid angle calculations in this work.

### **5.2 VALIDATION OF CODE CALCULATIONS**

#### **5.2.1 KMESS vs. Experimental**

Validation of the mesh-grid method, as a means of predicting the full-energy peak efficiency of a germanium detector, was done through comparison with experimental results. The detector used for validation was a lithium-drifted germanium detector that has a long history, 30+ years, of efficiency calibration data associated with it. This detector is known at LANL as counter 76. This means there is an archive of efficiency curves that are well known and documented for this detector. This made it the optimal choice for comparison to KMESS simulations.

Several simulations were performed using KMESS for both point sources and cylindrical sources. The point source was assumed to be made from a NIST traceable mixed radionuclide solution, model number QCY48, from AEA Technologies, Inc. The cylindrical sources were 5 mL of this mixed radionuclide solution, in 4M HCl, in a 20 mL polyethylene liquid scintillation vial. The source-to-detector distances for these measurements are set by the automatic sample changer shelf heights. The shelf height distances for the sample changer associated with counter 76 are shown in Table 5.8.

Table 5.8: Shelf Height Distances (in cm) for Point Source and Vial Source Counting Geometries for Counter 76.

<b>Shelf #</b>	<b>Point Source Height (cm)</b>	<b>Vial Source Height (cm)</b>
1	0.150	0.474
2	0.450	0.774
3	0.750	1.074
4	1.250	1.574
5	1.750	2.074
6	2.250	2.574
7	2.750	3.074
8	3.750	4.074
9	4.750	5.074
10	5.750	6.074
11	7.750	8.074
12	9.750	10.074
13	11.750	12.074
14	13.750	14.074
15	16.750	17.074
16	19.750	20.074
17	24.750	25.074
18	29.750	30.074
19	39.750	40.074
20	49.750	50.074
21	59.750	60.074
22	79.750	80.074
23	84.150	84.474

The distances shown in Table 5.8 for point sources, are the exact distance from the source to the detector end-cap. However, the distances shown in Table 5.8 for the vial source are the distances from the lid of the liquid scintillation vial to the detector end-cap. Thus, to get the distance from the top of the solution, one has to add 4.95 cm to the vial source distances shown in Table 5.8.

The first set of simulations performed were for point sources with the most recent experimental efficiency calibration data. These happened to be shelf numbers 1, 2, 5, 10, 12, and 22. Using shelf 10 as the reference geometry, the effective solid angles were computed for the other shelves. The results of these calculations are shown in Tables 5.9 through 5.13.

Table 5.9: Experimentally Measured Efficiencies and KMESS Effective Solid Angle Calculated Efficiencies for a Point Source on Shelf 1 of Counter 76.

<b>Energy</b>	<b>Experimental</b>	<b>Effective Solid Angle</b>	<b>Difference</b>
<b>[keV]</b>	<b>Efficiency</b>	<b>Efficiency</b>	<b>[%]</b>
88.04	1.261E-01	1.210E-01	4.00
122.06	1.715E-01	1.626E-01	5.17
165.86	1.556E-01	1.504E-01	3.35
279.20	9.431E-02	9.250E-02	1.92
391.69	6.408E-02	6.376E-02	0.50
514.00	4.689E-02	4.745E-02	-1.20
661.66	3.513E-02	3.622E-02	-3.12
898.04	2.483E-02	2.631E-02	-5.96
1173.24	1.839E-02	2.001E-02	-8.81
1332.50	1.595E-02	1.763E-02	-10.53
1836.06	1.121E-02	1.294E-02	-15.43

Table 5.10: Experimentally Measured Efficiencies and KMESS Effective Solid Angle Calculated Efficiencies for a Point Source on Shelf 2 of Counter 76.

<b>Energy</b>	<b>Experimental</b>	<b>Effective Solid Angle</b>	<b>Difference</b>
<b>[keV]</b>	<b>Efficiency</b>	<b>Efficiency</b>	<b>[%]</b>
88.04	1.093E-01	1.062E-01	2.85
122.06	1.423E-01	1.377E-01	3.25
165.86	1.276E-01	1.242E-01	2.64
279.20	7.684E-02	7.601E-02	1.09
391.69	5.213E-02	5.229E-02	-0.31
514.00	3.817E-02	3.888E-02	-1.87
661.66	2.865E-02	2.967E-02	-3.56
898.04	2.035E-02	2.149E-02	-5.59
1173.24	1.518E-02	1.634E-02	-7.62
1332.50	1.323E-02	1.439E-02	-8.77
1836.06	9.453E-03	1.056E-02	-11.71

Table 5.11: Experimentally Measured Efficiencies and KMESS Effective Solid Angle Calculated Efficiencies for a Point Source on Shelf 5 of Counter 76.

<b>Energy</b>	<b>Experimental</b>	<b>Effective Solid Angle</b>	<b>Difference</b>
<b>[keV]</b>	<b>Efficiency</b>	<b>Efficiency</b>	<b>[%]</b>
88.04	5.735E-02	5.531E-02	3.56
122.06	6.923E-02	6.770E-02	2.21
165.86	6.053E-02	5.979E-02	1.22
279.20	3.655E-02	3.652E-02	0.09
391.69	2.517E-02	2.519E-02	-0.06
514.00	1.867E-02	1.876E-02	-0.49
661.66	1.419E-02	1.434E-02	-1.04
898.04	1.024E-02	1.042E-02	-1.78
1173.24	7.746E-03	7.939E-03	-2.49
1332.50	6.799E-03	6.999E-03	-2.94
1836.06	4.942E-03	5.146E-03	-4.13

Table 5.12: Experimentally Measured Efficiencies and KMESS Effective Solid Angle Calculated Efficiencies for a Point Source on Shelf 12 of Counter 76.

<b>Energy</b>	<b>Experimental</b>	<b>Effective Solid Angle</b>	<b>Difference</b>
<b>[keV]</b>	<b>Efficiency</b>	<b>Efficiency</b>	<b>[%]</b>
59.54	1.923E-03	1.181E-03	38.58
88.04	5.299E-03	5.209E-03	1.71
122.06	6.271E-03	6.460E-03	-3.02
165.86	5.919E-03	6.018E-03	-1.67
391.69	2.661E-03	2.770E-03	-4.10
661.66	1.604E-03	1.617E-03	-0.83
898.04	1.199E-03	1.191E-03	0.68
1173.24	9.181E-04	9.167E-04	0.16
1332.50	8.265E-04	8.118E-04	1.78
1836.06	6.062E-04	6.026E-04	0.59

Table 5.13: Experimentally Measured Efficiencies and KMESS Effective Solid Angle Calculated Efficiencies for a Point Source on Shelf 22 of Counter 76.

<b>Energy</b>	<b>Experimental</b>	<b>Effective Solid Angle</b>	<b>Difference</b>
<b>[keV]</b>	<b>Efficiency</b>	<b>Efficiency</b>	<b>[%]</b>
88.04	1.091E-04	9.374E-05	14.08
122.06	1.056E-04	1.198E-04	-13.40
279.20	7.861E-05	7.998E-05	-1.74
391.69	5.889E-05	5.784E-05	1.79
514.00	4.517E-05	4.408E-05	2.42
661.66	3.503E-05	3.434E-05	1.98
898.04	2.576E-05	2.563E-05	0.50
1173.24	1.973E-05	1.989E-05	-0.82
1332.50	1.739E-05	1.768E-05	-1.67
1836.06	1.269E-05	1.322E-05	-4.19

The experimental and KMESS calculated full-energy peak efficiencies agree quite well except at the energy extremes or when the source is placed close to the detector. This could be due to improper treatment of the low-energy peaks during the experimental analysis. The choice of  $^{241}\text{Am}$  for the low-energy calibration was also probably a poor one, because it tends to have some calibration difficulties associated with it. The differences at low gamma-ray energy could also be attributed to the improper treatment by KMESS of the detector bulletization. The exact dead-layer thickness and distribution for counter 76 is also not known. KMESS assumes that the dead-layer is uniform and that the thickness supplied by the manufacturer is correct. These assumptions were shown elsewhere to not always necessarily be true (Jackman, 2004). Because of this, low-energy differences may arise from the KMESS treatment of the dead-layer.

The disagreements at high gamma-ray energies tend to increase with shorter source-to-detector distances. This disagreement is primarily because the experimental efficiencies were not properly corrected for coincidence summing. The isotopes used to calibrate the four highest energy points were  $^{88}\text{Y}$  and  $^{60}\text{Co}$ . These two isotopes are well-known to emit multiple cascade gamma-rays, with high intensities, in their decay. The cascade summing losses increase for shorter source-to-detector distances, and thus reduce the experimentally observed full-energy peak efficiencies.

The next set of simulations performed were for the vial source with the most recent experimental efficiency calibration data. These happened to be shelf numbers 1, 5, 10, 12, 13, and 22. Using shelf 10 as the reference geometry, the effective solid angles were computed for the other shelves. The results of these calculations are shown in Tables 5.14 through 5.18. These calculations were done without source self-attenuation, but included attenuation through the polyethylene liquid scintillation vial.

Table 5.14: Experimentally Measured Efficiencies and KMESS Effective Solid Angle Calculated Efficiencies for a Vial Source on Shelf 1 of Counter 76.

<b>Energy</b> <b>[keV]</b>	<b>Experimental</b> <b>Efficiency</b>	<b>Effective Solid Angle</b> <b>Efficiency</b>	<b>Difference</b> <b>[%]</b>
59.54	3.472E-03	3.050E-03	12.16
88.04	9.409E-03	9.054E-03	3.78
122.06	1.154E-02	1.146E-02	0.74
165.86	1.083E-02	1.085E-02	-0.17
279.20	7.147E-03	7.237E-03	-1.26
391.69	5.069E-03	5.145E-03	-1.51
661.66	2.982E-03	3.054E-03	-2.42
898.04	2.215E-03	2.288E-03	-3.28
1173.24	1.724E-03	1.796E-03	-4.16
1332.50	1.536E-03	1.607E-03	-4.65
1836.06	1.164E-03	1.235E-03	-6.09

Table 5.15: Experimentally Measured Efficiencies and KMESS Effective Solid Angle Calculated Efficiencies for a Vial Source on Shelf 5 of Counter 76.

<b>Energy</b> <b>[keV]</b>	<b>Experimental</b> <b>Efficiency</b>	<b>Effective Solid Angle</b> <b>Efficiency</b>	<b>Difference</b> <b>[%]</b>
59.54	2.379E-03	2.074E-03	12.81
88.04	6.532E-03	6.149E-03	5.87
122.06	7.960E-03	7.820E-03	1.76
165.86	7.462E-03	7.476E-03	-0.19
279.20	4.971E-03	5.037E-03	-1.33
391.69	3.559E-03	3.595E-03	-1.02
661.66	2.120E-03	2.143E-03	-1.07
898.04	1.580E-03	1.608E-03	-1.78
1173.24	1.231E-03	1.264E-03	-2.71
1332.50	1.096E-03	1.133E-03	-3.33
1836.06	8.266E-04	8.714E-04	-5.42

Table 5.16: Experimentally Measured Efficiencies and KMESS Effective Solid Angle Calculated Efficiencies for a Vial Source on Shelf 12 of Counter 76.

<b>Energy</b>	<b>Experimental</b>	<b>Effective Solid Angle</b>	<b>Difference</b>
<b>[keV]</b>	<b>Efficiency</b>	<b>Efficiency</b>	<b>[%]</b>
59.54	7.034E-04	5.746E-04	18.31
88.04	1.796E-03	1.711E-03	4.76
122.06	2.281E-03	2.209E-03	3.16
165.86	2.225E-03	2.169E-03	2.53
279.20	1.542E-03	1.502E-03	2.60
391.69	1.111E-03	1.084E-03	2.41
661.66	6.624E-04	6.525E-04	1.49
898.04	4.941E-04	4.924E-04	0.35
1173.24	3.850E-04	3.888E-04	-0.98
1332.50	3.429E-04	3.489E-04	-1.74
1836.06	2.586E-04	2.695E-04	-4.20

Table 5.17: Experimentally Measured Efficiencies and KMESS Effective Solid Angle Calculated Efficiencies for a Vial Source on Shelf 13 of Counter 76.

<b>Energy</b>	<b>Experimental</b>	<b>Effective Solid Angle</b>	<b>Difference</b>
<b>[keV]</b>	<b>Efficiency</b>	<b>Efficiency</b>	<b>[%]</b>
59.54	7.298E-04	4.583E-04	37.20
122.06	1.877E-03	1.768E-03	5.82
165.86	1.776E-03	1.742E-03	1.93
391.69	8.850E-04	8.751E-04	1.12
661.66	5.377E-04	5.277E-04	1.87
898.04	4.048E-04	3.984E-04	1.57
1173.24	3.176E-04	3.148E-04	0.88
1332.50	2.835E-04	2.826E-04	0.32
1836.06	2.148E-04	2.184E-04	-1.66



Table 5.18: Experimentally Measured Efficiencies and KMESS Effective Solid Angle Calculated Efficiencies for a Vial Source on Shelf 22 of Counter 76.

<b>Energy</b>	<b>Experimental</b>	<b>Effective Solid Angle</b>	<b>Difference</b>
<b>[keV]</b>	<b>Efficiency</b>	<b>Efficiency</b>	<b>[%]</b>
59.54	2.205E-05	2.085E-05	5.45
88.04	6.389E-05	6.288E-05	1.58
122.06	8.278E-05	8.277E-05	0.01
165.86	8.177E-05	8.387E-05	-2.57
279.20	5.795E-05	6.012E-05	-3.74
391.69	4.245E-05	4.403E-05	-3.72
661.66	2.602E-05	2.684E-05	-3.16
898.04	1.974E-05	2.038E-05	-3.26
1173.24	1.564E-05	1.620E-05	-3.58
1332.50	1.404E-05	1.458E-05	-3.82
1836.06	1.081E-05	1.132E-05	-4.73

The experimental and KMESS calculated full-energy peak efficiencies agree quite well except at low gamma-ray energies for all shelves. The disagreement at low gamma-ray energies could be attributed to poor experimental treatment of the  $^{241}\text{Am}$  peak. They also could be attributed to detector bulletization or a non-uniform dead-layer. The run time on these simulations was on the order of  $\sim 10$  minutes. This was because the source was meshed to a high order that produced around 4,900 points.

The final KMESS simulations performed were for a vial source, but done using a point source at shelf 10 as the reference geometry. This tested how well KMESS was able to convert between different source geometries. The results of shelves 1 and 22 are shown in Tables 5.19 and 5.20. These simulations included source self-attenuation and attenuation through the polyethylene scintillation vial for the vial source.

Table 5.19: Experimentally Measured Efficiencies and KMESS Effective Solid Angle Calculated Efficiencies for a Vial Source on Shelf 1 of Counter 76 Using a Point Source on Shelf 10 as the Reference Curve.

<b>Energy</b> <b>[keV]</b>	<b>Experimental</b> <b>Efficiency</b>	<b>Effective Solid Angle</b> <b>Efficiency</b>	<b>Difference</b> <b>[%]</b>
59.54	3.472E-03	2.101E-03	39.50
88.04	9.409E-03	9.623E-03	-2.28
122.06	1.154E-02	1.205E-02	-4.38
165.86	1.083E-02	1.119E-02	-3.29
279.20	7.147E-03	7.311E-03	-2.29
391.69	5.069E-03	5.220E-03	-2.98
661.66	2.982E-03	3.094E-03	-3.75
898.04	2.215E-03	2.298E-03	-3.75
1173.24	1.724E-03	1.782E-03	-3.34
1332.50	1.536E-03	1.583E-03	-3.06
1836.06	1.164E-03	1.184E-03	-1.70

Table 5.20: Experimentally Measured Efficiencies and KMESS Effective Solid Angle Calculated Efficiencies for a Vial Source on Shelf 22 of Counter 76 Using a Point Source on Shelf 10 as the Reference Curve.

<b>Energy</b> <b>[keV]</b>	<b>Experimental</b> <b>Efficiency</b>	<b>Effective Solid Angle</b> <b>Efficiency</b>	<b>Difference</b> <b>[%]</b>
59.54	2.205E-05	1.438E-05	34.81
88.04	6.389E-05	6.689E-05	-4.69
122.06	8.278E-05	8.710E-05	-5.21
165.86	8.177E-05	8.651E-05	-5.80
279.20	5.795E-05	6.076E-05	-4.85
391.69	4.245E-05	4.468E-05	-5.24
661.66	2.602E-05	2.720E-05	-4.55
898.04	1.974E-05	2.047E-05	-3.72
1173.24	1.564E-05	1.608E-05	-2.80
1332.50	1.404E-05	1.436E-05	-2.26
1836.06	1.081E-05	1.086E-05	-0.44

The results for shelves 1 and 22, using a point source on shelf 10 as the reference efficiency curve, seem to have fairly good agreement with experimental measurements except at low gamma-ray energies. This could be due to improper treatment by KMESS of the detector bulletization or lack of knowledge of exact detector dimensions, such as the dead layer. The differences at low gamma-ray energy may also be attributed to poor experimental treatment of the  $^{241}\text{Am}$  peak. The simulations took significantly longer to run using the current source self-attenuation routines. This however, serves as a testament that KMESS works well at converting between different sample shapes and counting geometries.

### 5.2.2 KMESS vs. Other Codes

One of the reasons for the development of KMESS was that no code currently available could make quick and accurate calculations of detector efficiencies. To demonstrate this, the results of several codes were compared to those obtained by KMESS. The cases considered were the same as those above in Section 5.2.1. The codes used to compare with KMESS were SYNTH and EFFIC. Both of these codes use the same underlying principle of effective interaction depth (Gunnink *et al.*, 1992). EFFIC was the code developed by Ray Gunnink to predict and fit efficiency curves for the GAMANAL program. The documentation on SYNTH claims that it uses the same algorithms as EFFIC, but as will be shown, this is not the case. The results of SYNTH and EFFIC for the point source cases of counter 76 considered above are compiled in Tables 5.21 through 5.25. EFFIC was run with the same reference curve as KMESS, namely a point source on shelf 10.

Table 5.21: Experimentally Measured, SYNTH, and EFFIC Efficiencies for a Point Source on Shelf 1 of Counter 76.

<b>Energy</b>	<b>Experimental</b>	<b>SYNTH</b>	<b>EFFIC</b>	<b>SYNTH Diff.</b>	<b>EFFIC Diff.</b>
<b>[keV]</b>	<b>Efficiency</b>	<b>Efficiency</b>	<b>Efficiency</b>	<b>[%]</b>	<b>[%]</b>
88.04	1.261E-01	1.695E-01	2.220E-01	-34.44	-76.03
122.06	1.715E-01	2.156E-01	2.657E-01	-25.71	-54.95
165.86	1.556E-01	2.136E-01	2.278E-01	-37.28	-46.40
279.20	9.431E-02	1.526E-01	1.308E-01	-61.84	-38.69
391.69	6.408E-02	1.111E-01	8.623E-02	-73.33	-34.57
514.00	4.689E-02	8.482E-02	6.213E-02	-80.89	-32.51
661.66	3.513E-02	6.571E-02	4.634E-02	-87.05	-31.90
898.04	2.483E-02	4.797E-02	3.314E-02	-93.19	-33.46
1173.24	1.839E-02	3.616E-02	2.526E-02	-96.62	-37.37
1332.50	1.595E-02	3.151E-02	2.239E-02	-97.55	-40.39
1836.06	1.121E-02	2.200E-02	1.698E-02	-96.21	-51.49

Table 5.22: Experimentally Measured, SYNTH, and EFFIC Efficiencies for a Point Source on Shelf 2 of Counter 76.

<b>Energy</b>	<b>Experimental</b>	<b>SYNTH</b>	<b>EFFIC</b>	<b>SYNTH Diff.</b>	<b>EFFIC Diff.</b>
<b>[keV]</b>	<b>Efficiency</b>	<b>Efficiency</b>	<b>Efficiency</b>	<b>[%]</b>	<b>[%]</b>
88.04	1.093E-01	1.465E-01	1.670E-01	-34.04	-52.82
122.06	1.423E-01	1.863E-01	1.991E-01	-30.92	-39.88
165.86	1.276E-01	1.846E-01	1.739E-01	-44.66	-36.26
279.20	7.684E-02	1.319E-01	1.007E-01	-71.65	-31.12
391.69	5.213E-02	9.598E-02	6.670E-02	-84.12	-27.95
514.00	3.817E-02	7.330E-02	4.820E-02	-92.03	-26.28
661.66	2.865E-02	5.678E-02	3.603E-02	-98.20	-25.77
898.04	2.035E-02	4.145E-02	2.583E-02	-103.71	-26.94
1173.24	1.518E-02	3.125E-02	1.972E-02	-105.86	-29.93
1332.50	1.323E-02	2.723E-02	1.749E-02	-105.84	-32.21
1836.06	9.453E-03	1.901E-02	1.327E-02	-101.13	-40.40

Table 5.23: Experimentally Measured, SYNTH, and EFFIC Efficiencies for a Point Source on Shelf 5 of Counter 76.

Energy [keV]	Experimental Efficiency	SYNTH Efficiency	EFFIC Efficiency	SYNTH Diff. [%]	EFFIC Diff. [%]
88.04	5.735E-02	7.152E-02	6.389E-02	-24.72	-11.40
122.06	6.923E-02	9.095E-02	7.810E-02	-31.38	-12.81
165.86	6.053E-02	9.011E-02	6.994E-02	-48.87	-15.54
279.20	3.655E-02	6.439E-02	4.197E-02	-76.17	-14.83
391.69	2.517E-02	4.659E-02	2.825E-02	-85.08	-12.22
514.00	1.867E-02	3.578E-02	2.064E-02	-91.67	-10.57
661.66	1.419E-02	2.772E-02	1.557E-02	-95.37	-9.74
898.04	1.024E-02	2.024E-02	1.126E-02	-97.64	-9.97
1173.24	7.746E-03	1.526E-02	8.641E-03	-96.95	-11.55
1332.50	6.799E-03	1.329E-02	7.673E-03	-95.54	-12.86
1836.06	4.942E-03	9.281E-03	5.825E-03	-87.80	-17.86

Table 5.24: Experimentally Measured, SYNTH, and EFFIC Efficiencies for a Point Source on Shelf 12 of Counter 76.

Energy [keV]	Experimental Efficiency	SYNTH Efficiency	EFFIC Efficiency	SYNTH Diff. [%]	EFFIC Diff. [%]
59.54	1.923E-03	2.048E-03	1.108E-03	-6.49	42.37
88.04	5.299E-03	4.844E-03	4.893E-03	8.59	7.67
122.06	6.271E-03	6.160E-03	6.387E-03	1.78	-1.85
165.86	5.919E-03	6.103E-03	6.079E-03	-3.10	-2.70
391.69	2.661E-03	3.173E-03	2.751E-03	-19.25	-3.39
661.66	1.604E-03	1.877E-03	1.577E-03	-17.04	1.68
898.04	1.199E-03	1.371E-03	1.160E-03	-14.31	3.29
1173.24	9.181E-04	1.033E-03	8.985E-04	-12.53	2.14
1332.50	8.265E-04	9.004E-04	8.001E-04	-8.94	3.19
1836.06	6.062E-04	6.286E-04	6.081E-04	-3.70	-0.31

Table 5.25: Experimentally Measured, SYNTH, and EFFIC Efficiencies for a Point Source on Shelf 22 of Counter 76.

<b>Energy</b>	<b>Experimental</b>	<b>SYNTH</b>	<b>EFFIC</b>	<b>SYNTH Diff.</b>	<b>EFFIC Diff.</b>
<b>[keV]</b>	<b>Efficiency</b>	<b>Efficiency</b>	<b>Efficiency</b>	<b>[%]</b>	<b>[%]</b>
88.04	1.091E-04	7.536E-05	8.670E-05	30.93	20.54
122.06	1.056E-04	9.583E-05	1.171E-04	9.25	-10.93
279.20	7.861E-05	6.784E-05	7.828E-05	13.70	0.43
391.69	5.889E-05	4.937E-05	5.544E-05	16.16	5.85
514.00	4.517E-05	3.770E-05	4.183E-05	16.53	7.39
661.66	3.503E-05	2.921E-05	3.235E-05	16.62	7.65
898.04	2.576E-05	2.132E-05	2.393E-05	17.22	7.11
1173.24	1.973E-05	1.607E-05	1.858E-05	18.53	5.84
1332.50	1.739E-05	1.401E-05	1.654E-05	19.45	4.89
1836.06	1.269E-05	9.779E-06	1.251E-05	22.94	1.45

The point source calculations of detector efficiencies by SYNTH for almost all cases have poor agreement with the experimental curves. The only exception to this is on shelf 12, where the SYNTH results seem to agree slightly better for high and low gamma-ray energies. The EFFIC results seem to agree poorly for short source-to-detector distances, but agree fairly well for larger distances. This may be because the experimental efficiencies at short source-to-detector distances were not corrected for coincidence summing. In all cases, it is evident that there is a distinct difference between SYNTH and EFFIC. The KMESS results previously shown in Section 5.2.1 show much better agreement with experimental efficiencies at short source-to-detector distances. For all shelf heights, it can be argued that the KMESS results have comparable or better experimental agreement than EFFIC. The run times for all the codes are also comparable, because they predict point source efficiencies in fractions of a second.

The results of SYNTH and EFFIC for the vial source cases of counter 76 considered above are compiled in Tables 5.26 through 5.30. EFFIC was run with the same reference curve as KMESS, namely a vial source on shelf 10. SYNTH was also allowed to correct for source self-attenuation and the attenuation in the polyethylene

liquid scintillation vial. Unfortunately, the available version of EFFIC would not run if source or scintillation vial attenuation was used.

Table 5.26: Experimentally Measured, SYNTH, and EFFIC Efficiencies for a Vial Source on Shelf 1 of Counter 76.

<b>Energy</b>	<b>Experimental</b>	<b>SYNTH</b>	<b>EFFIC</b>	<b>SYNTH Diff.</b>	<b>EFFIC Diff.</b>
<b>[keV]</b>	<b>Efficiency</b>	<b>Efficiency</b>	<b>Efficiency</b>	<b>[%]</b>	<b>[%]</b>
59.54	3.472E-03	6.294E-03	3.437E-03	-81.29	1.00
88.04	9.409E-03	1.473E-02	1.011E-02	-56.60	-7.48
122.06	1.154E-02	1.865E-02	1.264E-02	-61.63	-9.54
165.86	1.083E-02	1.842E-02	1.199E-02	-70.11	-10.67
279.20	7.147E-03	1.312E-02	7.989E-03	-83.56	-11.78
391.69	5.069E-03	9.537E-03	5.687E-03	-88.14	-12.20
514.00	3.841E-03	7.278E-03	4.323E-03	-89.49	-12.54
661.66	2.982E-03	5.635E-03	3.368E-03	-88.96	-12.94
898.04	2.215E-03	4.110E-03	2.515E-03	-85.55	-13.55
1173.24	1.724E-03	3.095E-03	1.970E-03	-79.53	-14.25
1332.50	1.536E-03	2.696E-03	1.761E-03	-75.51	-14.65
1836.06	1.164E-03	1.879E-03	1.347E-03	-61.42	-15.69

Table 5.27: Experimentally Measured, SYNTH, and EFFIC Efficiencies for a Vial Source on Shelf 5 of Counter 76.

<b>Energy</b>	<b>Experimental</b>	<b>SYNTH</b>	<b>EFFIC</b>	<b>SYNTH Diff.</b>	<b>EFFIC Diff.</b>
<b>[keV]</b>	<b>Efficiency</b>	<b>Efficiency</b>	<b>Efficiency</b>	<b>[%]</b>	<b>[%]</b>
59.54	2.379E-03	3.806E-03	2.177E-03	-59.98	8.48
88.04	6.532E-03	9.002E-03	6.624E-03	-37.81	-1.41
122.06	7.960E-03	1.145E-02	8.220E-03	-43.81	-3.26
165.86	7.462E-03	1.134E-02	7.828E-03	-52.00	-4.91
279.20	4.971E-03	8.105E-03	5.356E-03	-63.05	-7.75
391.69	3.559E-03	5.898E-03	3.880E-03	-65.73	-9.01
514.00	2.716E-03	4.504E-03	2.971E-03	-65.85	-9.37
661.66	2.120E-03	3.490E-03	2.311E-03	-64.60	-9.03
898.04	1.580E-03	2.547E-03	1.701E-03	-61.23	-7.63
1173.24	1.231E-03	1.920E-03	1.294E-03	-55.98	-5.14
1332.50	1.096E-03	1.673E-03	1.135E-03	-52.67	-3.52
1836.06	8.266E-04	1.168E-03	8.079E-04	-41.30	2.26

Table 5.28: Experimentally Measured, SYNTH, and EFFIC Efficiencies for a Vial Source on Shelf 12 of Counter 76.

Energy	Experimental	SYNTH	EFFIC	SYNTH Diff.	EFFIC Diff.
[keV]	Efficiency	Efficiency	Efficiency	[%]	[%]
59.54	7.034E-04	8.826E-04	5.520E-04	-25.48	21.52
88.04	1.796E-03	2.088E-03	1.669E-03	-16.26	7.08
122.06	2.281E-03	2.655E-03	2.156E-03	-16.40	5.49
165.86	2.225E-03	2.631E-03	2.108E-03	-18.23	5.26
279.20	1.542E-03	1.880E-03	1.464E-03	-21.90	5.05
391.69	1.111E-03	1.368E-03	1.060E-03	-23.12	4.63
514.00	8.484E-04	1.045E-03	8.135E-04	-23.13	4.11
661.66	6.624E-04	8.093E-04	6.389E-04	-22.18	3.55
898.04	4.941E-04	5.908E-04	4.809E-04	-19.58	2.68
1173.24	3.850E-04	4.454E-04	3.784E-04	-15.69	1.72
1332.50	3.429E-04	3.881E-04	3.388E-04	-13.20	1.21
1836.06	2.586E-04	2.710E-04	2.593E-04	-4.80	-0.27

Table 5.29: Experimentally Measured, SYNTH, and EFFIC Efficiencies for a Vial Source on Shelf 13 of Counter 76.

Energy	Experimental	SYNTH	EFFIC	SYNTH Diff.	EFFIC Diff.
[keV]	Efficiency	Efficiency	Efficiency	[%]	[%]
59.54	7.298E-04	6.901E-04	4.352E-04	5.44	40.36
122.06	1.877E-03	2.076E-03	1.710E-03	-10.59	8.90
165.86	1.776E-03	2.057E-03	1.676E-03	-15.80	5.61
391.69	8.850E-04	1.069E-03	8.467E-04	-20.84	4.33
514.00	6.827E-04	8.167E-04	6.506E-04	-19.63	4.70
661.66	5.377E-04	6.327E-04	5.113E-04	-17.67	4.91
898.04	4.048E-04	4.619E-04	3.851E-04	-14.11	4.87
1173.24	3.176E-04	3.482E-04	3.031E-04	-9.65	4.55
1332.50	2.835E-04	3.035E-04	2.715E-04	-7.05	4.25
1836.06	2.148E-04	2.119E-04	2.078E-04	1.35	3.24



Table 5.30: Experimentally Measured, SYNTH, and EFFIC Efficiencies for a Vial Source on Shelf 22 of Counter 76.

<b>Energy</b>	<b>Experimental</b>	<b>SYNTH</b>	<b>EFFIC</b>	<b>SYNTH Diff.</b>	<b>EFFIC Diff.</b>
<b>[keV]</b>	<b>Efficiency</b>	<b>Efficiency</b>	<b>Efficiency</b>	<b>[%]</b>	<b>[%]</b>
59.54	2.205E-05	2.803E-05	1.899E-05	-27.11	13.86
88.04	6.389E-05	6.631E-05	5.785E-05	-3.78	9.46
122.06	8.278E-05	8.432E-05	7.646E-05	-1.86	7.63
165.86	8.177E-05	8.354E-05	7.638E-05	-2.17	6.59
279.20	5.795E-05	5.970E-05	5.455E-05	-3.01	5.87
391.69	4.245E-05	4.344E-05	3.989E-05	-2.33	6.03
661.66	2.602E-05	2.570E-05	2.434E-05	1.23	6.47
898.04	1.974E-05	1.876E-05	1.843E-05	4.95	6.65
1173.24	1.564E-05	1.414E-05	1.457E-05	9.57	6.85
1332.50	1.404E-05	1.233E-05	1.307E-05	12.21	6.91
1836.06	1.081E-05	8.605E-06	1.005E-05	20.40	7.05

The vial source calculations of detector efficiencies by SYNTH for almost all cases have poor agreement with experimental data. The only exceptions to this are on shelves 13 and 22. At shelf 13 the SYNTH results seem to agree slightly better for high and low gamma-ray energies. At shelf 22, the SYNTH results agree slightly better for the middle energy gamma-rays. The EFFIC results seem to agree poorly for shelf 1, but agree fairly well for all other shelves. This may again be due to coincidence summing issues in the experimental data at shorter distances. The KMESS results previously shown in Section 5.2.1 show much better agreement than SYNTH and EFFIC for shelf 1. For all other shelf heights, it can be argued that the KMESS results show experimental agreement that is comparable to the results obtained with EFFIC. The run times for KMESS were slightly longer, ~10 minutes, whereas the run times for SYNTH and EFFIC were still fractions of a second.

### 5.2.3 Grid Sensitivity Tests

One of the main techniques employed by the mesh-grid method is to treat distributed sources as large collections of point sources. In order to quantify what “large” collection of point sources means to KMESS, it is necessary to perform tests of the mesh-grid sensitivity. This also allows one to determine the highest degree of accuracy produced by KMESS in the smallest amount of computation time. The detector used in these tests was counter 76.

The first test performed was using two line sources placed above the surface of the detector at a source-to-detector distance of 1 cm. The lines were drawn parallel to the  $x$ -axis and placed at  $y = -1$  cm and  $y = 1$  cm. The lines had lengths of 2 cm and the endpoints were placed at  $x = -1$  cm and  $x = 1$  cm. The lines were then divided into smaller grids by including more points on the lines between the endpoints. The average effective solid angles for different numbers of grid were then calculated using KMESS. The results of this test are shown in Figure 5.3. Because of the cylindrical symmetry of the situation, it was deemed unnecessary to perform this test for the  $y$ -dimension.

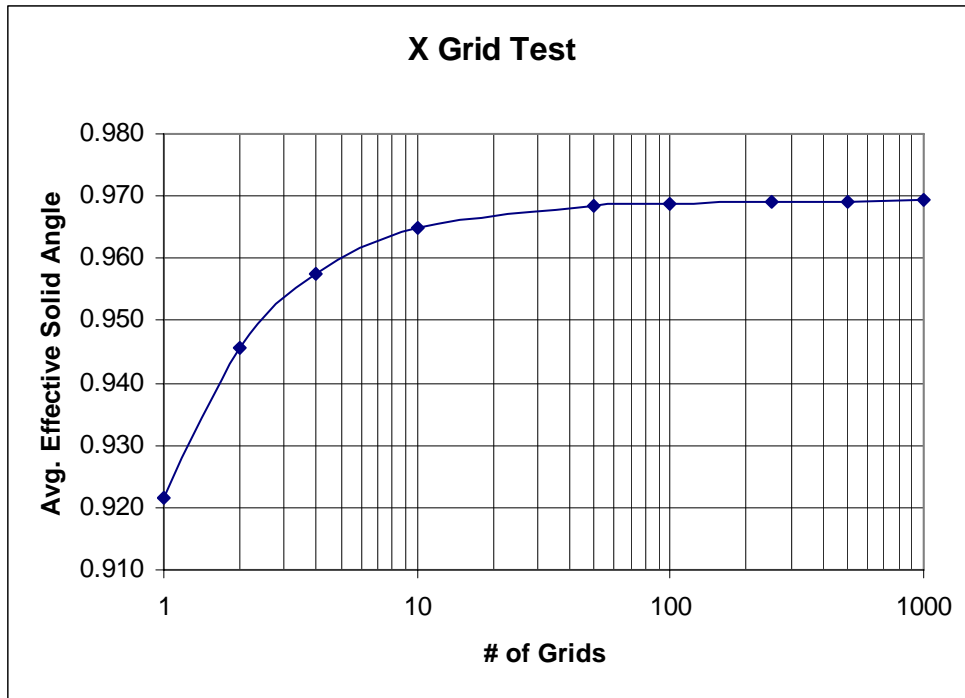


Figure 5.3: Average Effective Solid Angle, as a Function of the Number of Points on the Line, for Two Line Sources Pointing in the  $X$ -direction.

The next test performed was using four line sources placed above the detector surface. However, this time the lines were drawn parallel to the  $z$ -axis and placed at  $xy$ -coordinates of  $(-1,-1)$ ,  $(-1, 1)$ ,  $(1, -1)$ , and  $(1, 1)$ . The lines had lengths of 10 cm and the endpoints were placed at  $z = 1$  cm and  $z = 11$  cm. The lines were then divided into smaller grids and the average effective solid angles calculated using KMESS. The results of this test are shown in Figure 5.4.

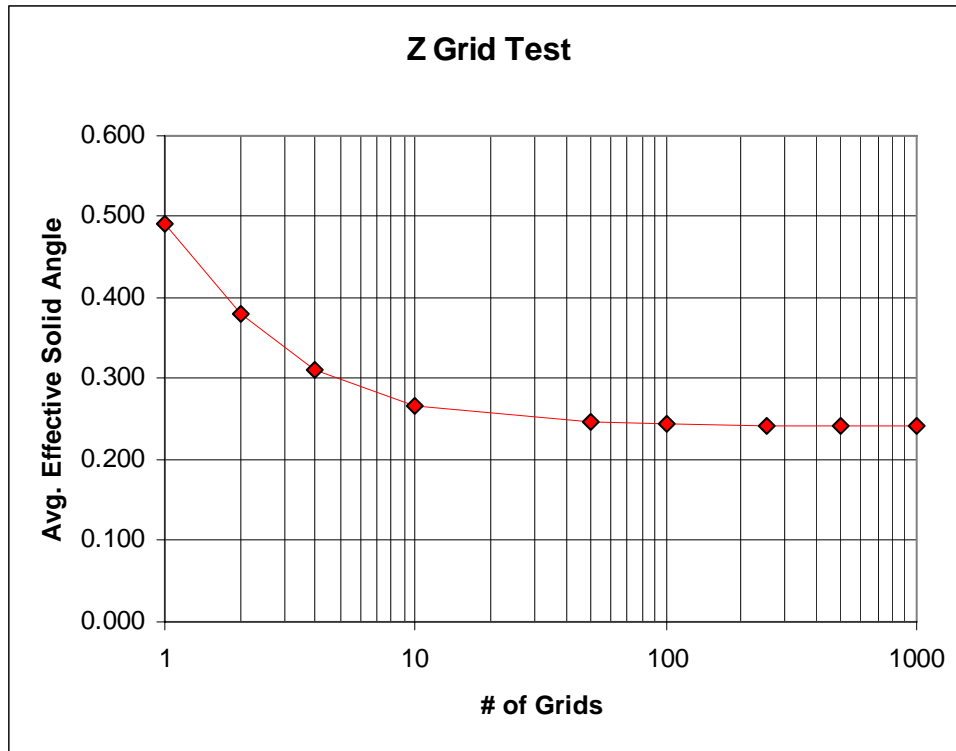


Figure 5.4: Average Effective Solid Angle, as a Function of the Number of Points on the Line, for Four Line Sources Pointing in the Z-direction.

The final test performed was using a disc source placed above the surface of the detector at a source-to-detector distance of 0.5 cm. In this test, the disc was modeled in cylindrical coordinates and had a radius of 1.2 cm. The disc was placed so that its axis coincided with the primary axis of the detector and it was parallel to the detector surface. The disc was then divided into grids using the same number of grids for both the  $r$  and  $\theta$  directions. One limitation to this test was that the number of grids in both directions was only allowed to go to 70. This limitation was necessary because the number of points began to reach the maximum number of points allowed, ~5000, by KMESS. The results of this test are shown in Figure 5.5.

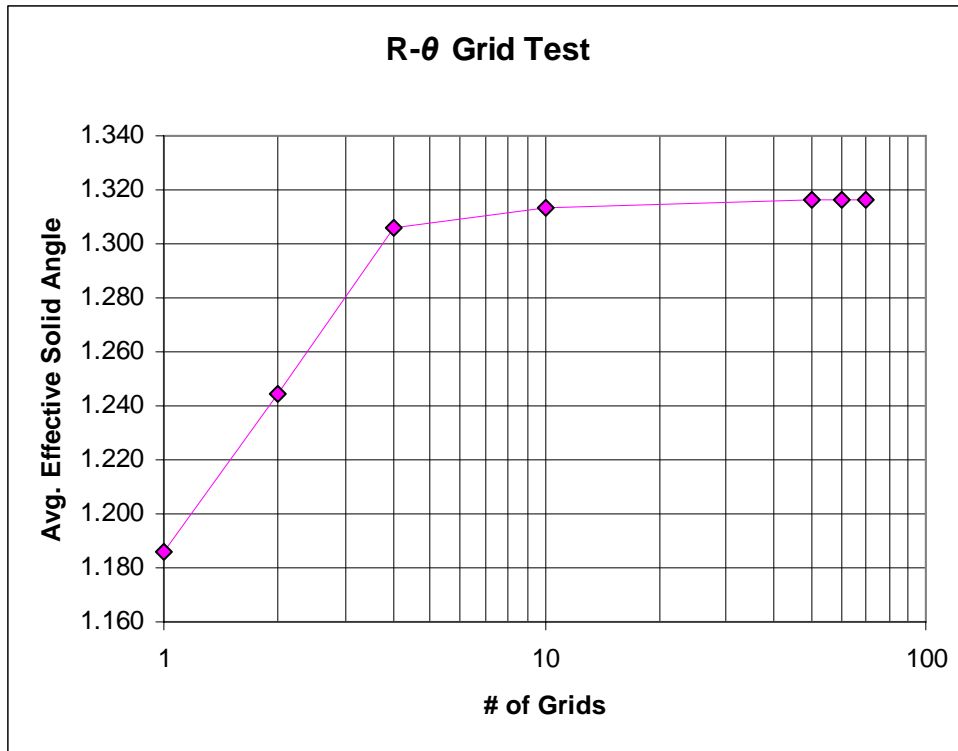


Figure 5.5: Average Effective Solid Angle, as a Function of the Number of Points in the  $R$  and  $\theta$  Directions, for a Disc Source.

All of these tests seem to hint at the same end result. This is that the average effective solid angle begins to level off after grid sizes between about 0.1 to 1 mm per grid in any given direction. This is despite changes in source-to-detector distance. Based on these results, the current limitation on the number of allowed points in KMESS should probably be increased in the future.

## Chapter 6: Conclusions

The results reported in this work appear promising for using KMESS to predict the full-energy peak efficiencies of high-purity germanium detectors. As was shown, KMESS can predict the absolute full-energy peak efficiencies of germanium detectors to within an accuracy of less than 10% on average, and in most cases much less than 10%, for the energy range 100–1800 keV. This energy range covers the gamma-rays from most fission products. The code performed slightly better when the reference geometry was the same as the desired geometry. However, even when the reference geometry was changed, the predicted efficiencies still had good agreement with experimental results. The KMESS results tended to disagree more for high and low gamma-ray energies and for close source-to-detector distances.

KMESS performed much better at predicting efficiencies than SYNTH. It performed just as well, if not better, at predicting efficiencies than EFFIC. The run times of KMESS were comparable to EFFIC and SYNTH. However, the run times are significantly less for KMESS than required when using Monte Carlo techniques. KMESS ran on the order of a fraction of a second for point sources. Large source meshes, ~5000 points, ran on the order of 10 minutes. However, KMESS ran significantly longer when the current source self-attenuation routine was used.

Further improvements to KMESS could be made in several ways. The code could be made to run faster by including a better source self-attenuation calculation routine. Other numerical integration methods should be explored to improve code run times and accuracy. Corrections for summing, non-uniform dead-layers, and detector bulletization may help improve results for low and high energy gamma-rays. Additional source and absorber materials should also be added to improve code versatility.

KMESS is currently being prepared for open-source distribution under the GNU Public License. The web interface for KMESS is intended for open-source distribution as well. This software will be incorporated into the NGWeb software of the Nuclear and Radiochemistry group's counting room at Los Alamos National Laboratory. A copy of the source code may be obtained by contacting this group at Los Alamos National Laboratory.

## Appendix

### A.1 ADDITIONAL KMESS DOCUMENTATION

#### A.1.1 KMESS README FILE

##### KMESS README FILE

Kevin Jackman  
June, 2007.

##### I. Description of KMESS

KMESS is a C language program that uses a semi-empirical method to calculate the full-energy peak efficiencies of a germanium detector. The basic idea behind KMESS is built around the concept of the Moen's effective solid angle. For information on the effective solid angle concept, see the following journal article:

L. Moens et al., Nuclear Instruments & Methods, Vol. 187 (1981) pgs 451-472.

The methods used by both KMESS and Moen's are based on using an experimentally determined reference measurement to predict the full-energy peak efficiency for a different desired counting geometry. Moen's (as well as others) typically described the gamma-ray source shape analytically, using standard geometrical shapes (cylinders, discs, etc...). Their methods became extremely difficult to use for source shapes that could not be easily parametrized using analytic functions. Thus, their methods are highly undesirable for oddly shaped sources.

Enter KMESS.

KMESS treats the gamma-ray source as a collection of point sources. It determines the full-energy peak efficiency for each point source and then averages them together. Weighted averaging is possible, but is currently disabled. This makes it easy to predict efficiencies for anything from simple to very complex source shapes. In KMESS, both a reference source shape and a desired source shape are specified with a mesh. This mesh is a collection of points that describes both the source shape, and location of the source relative to the germanium detector. For a description on the required mesh coordinate system, see the README file on source files. In short, assume the



center of the outer surface of the detector end cap is the origin. In addition to a mesh, the user must supply a table of energy-efficiency point pairs in order to convert effective solid angle into full-energy peak efficiency. At a minimum then, KMESS needs a reference source file (.ksf), a desired geometry source file (.ksf), a detector file (.kdf), and a reference energy-efficiency curve file (.krf) to calculate a full-energy peak efficiency. KMESS can also be run to account for any additional absorbing materials between the source and detector. At the time of writing this document, absorber use is limited to one absorber. KMESS also assumes that the absorber covers the entire detector end cap. See the README me on absorber files for more information. The number of available materials is also limited to those currently in the materials/ directory. For help in adding new materials see the README on cross-section files. KMESS output defaults to the screen unless the -o <filename> option is used to tell it to output the results to <filename>.

## II. Compiling and Building of KMESS

Included with the KMESS source code should have been a Makefile. Thus, to build KMESS, all you have to do is go to the directory where the source files were unpacked and type "make" at a command prompt to compile and build KMESS. The GNU GCC compiler (version > 4.0) should be used and the GNU Make utility must be installed.

If the Makefile is not there or if you are attempting to build on a non-Unix /Linux platform, you need to first have a C compiler. Then each of the source files needs to be compiled using a command similar to:

```
#gcc -c kmesscalc.c
```

Then the whole package can be put together with a command similar to:

```
#gcc -o kmess kmess.c kmesscalc.o kmessnumrec.o kmessfileio.o
```

## III. Available KMESS Run Methods

1. ./kmess -t

DESCRIPTION: Runs a test set of data through KMESS. Output is to screen.

2. ./kmess -d <det-filename> -s <rsrc-filename>

DESCRIPTION: Calculates the average effective solid angles of the points in the source file <rsrc-filename> using the detector file <det-filename>.

Output is to screen.

3. `./kmess -d <det-filename> -s <rsrc-filename> -g <gsrc-filename>`  
DESCRIPTION: Calculates the average effective solid angles of the points in the source files, `<rsrc-filename>` and `<gsrc-filename>`, using the detector file `<det-filename>`. Output is to screen.
  
4. `./kmess -d <det-filename> -s <rsrc-filename> -g <gsrc-filename> -r <ref-filename>`  
DESCRIPTION: Calculates the full-energy peak efficiency of the desired source geometry file `<gsrc-filename>`, using `<rsrc-filename>` as the reference source geometry file and reference curve file `<ref-filename>`. This is done using the detector file `<det-filename>`. Output is to screen.
  
5. `./kmess -d <det-filename> -s <rsrc-filename> -a <abs-filename>`  
DESCRIPTION: Calculates the average effective solid angles of the points in the source file `<rsrc-filename>` using the detector file `<det-filename>`. Uses an absorber file `<abs-filename>` to correct for an absorber placed between the source and detector. Output is to screen.
  
6. `./kmess -d <det-filename> -s <rsrc-filename> -g <gsrc-filename> -a <abs-filename>`  
DESCRIPTION: Calculates the average effective solid angles of the points in the source files, `<rsrc-filename>` and `<gsrc-filename>`, using the detector file `<det-filename>`. Uses an absorber file `<abs-filename>` to correct for an absorber placed between the source and detector. Output is to screen.
  
7. `./kmess -d <det-filename> -s <rsrc-filename> -g <gsrc-filename> -r <ref-filename> -a <abs-filename>`  
DESCRIPTION: Calculates the full-energy peak efficiency of the desired source geometry file `<gsrc-filename>`, using `<rsrc-filename>` as the reference source geometry file and reference curve file `<ref-filename>`. This is done using the detector file `<det-filename>`. Uses an absorber file `<abs-filename>` to correct for an absorber placed between the source and detector. Output is to screen.
  
8. `./kmess -d <det-filename> -s <rsrc-filename> -o <out-filename>`  
DESCRIPTION: Same as run method 2, but output is to file `<out-filename>` instead of to screen.
  
9. `./kmess -d <det-filename> -s <rsrc-filename> -g <gsrc-filename> -o <out-filename>`  
DESCRIPTION: Same as run method 3, but output is to file `<out-filename>` instead of to screen.

10. `./kmess -d <det-filename> -s <rsrc-filename> -g <gsrc-filename> -r <ref-filename> -o <out-filename>`

DESCRIPTION: Same as run method 4, but output is to file <out-filename> instead of to screen.

11. `./kmess -d <det-filename> -s <rsrc-filename> -a <abs-filename> -o <out-filename>`

DESCRIPTION: Same as run method 5, but output is to file <out-filename> instead of to screen.

12. `./kmess -d <det-filename> -s <rsrc-filename> -g <gsrc-filename> -a <abs-filename> -o <out-filename>`

DESCRIPTION: Same as run method 6, but output is to file <out-filename> instead of to screen.

13. `./kmess -d <det-filename> -s <rsrc-filename> -g <gsrc-filename> -r <ref-filename> -a <abs-filename> -o <out-filename>`

DESCRIPTION: Same as run method 7, but output is to file <out-filename> instead of to screen.

## **A.1.2 KMESS Absorber File (KAF) README**

### **KMESS ABSORBER FILE FORMAT DESCRIPTION (.KAF)**

Kevin R. Jackman  
Los Alamos National Laboratory  
05/08/2007

#### **I. INTRODUCTION**

This file contains the primary description on how to create an absorber file (.KAF) for use with KMESS (Kevin's Mesh Efficiency Simulator Software). The primary information contained in a KMESS absorber file is the absorber material and thickness. At present, the absorber is assumed to surround the entire detector end cap, both top and sides, with the specified thickness of the specified material. In other words, an absorber in KMESS is like an additional detector end cap that surrounds the real detector end cap

with the specified thickness of the specified material. This may, to some, seem like a limiting assumption for simulations involving absorbers. However, because of the rarity of absorber measurements at LANL, this assumption was chosen. In future versions of KMESS and the .KAF file format, it may be more useful to specify the absorber as a mesh, as an absorber that surrounds the source, or an absorber based on a standard geometrical shape. Another limitation is that KMESS currently allows for only one absorber. This means that there can be only one absorber material of one thickness. Future releases of KMESS should allow for multiple materials of multiple thicknesses. There is also only a small amount of materials to choose from for the absorbing material. A new material can be added by making a KMESS photon cross-section file for that material and adding that material name and file name into the KMESS source code in the appropriate places. See the KMESS source code and photon cross-section README files for how to do that.

The format for a KMESS absorber file follows a keyword-value format. This allows one to be able to tell what is contained within the file simply by looking at it in a text file viewer. The files should be written such that they are white space (spaces or tabs) delimited. It should be mentioned that the C routine written to read in the file only cares that it finds the keyword identifier followed by white space followed by values that are delimited by white space up until the end of the line. The current file reading routine can only handle 200 characters per line. However, this can be easily increased in the "kmess.h" file. For help doing that, see the comments contained in that file. The keyword identifiers and values needed to make a successful absorber file are described below as well as the units that are expected for such values. The keyword identifier can be no longer than 30 characters. This can be easily adjusted in the kmess source files.

## II. KEYWORD IDENTIFIERS, THEIR ASSOCIATED VALUES, AND DESCRIPTIONS

The following is a complete list of the currently recognized keyword identifiers contained in a KMESS absorber file, followed by a brief description of each. The order of the keyword identifiers in the file is unimportant. However, the minimum keyword identifiers and values necessary for specifying an absorber in a KMESS absorber file are an absorber name, an absorber material, and an absorber thickness in units of centimeters (see descriptions of identifiers II.1 through II.3 below). Future additions to KMESS may be to include a "unit" value after the absorber thickness, so that the input is more flexible with respect to the system of units allowed. Comments are kept if and only if they are specified with the keyword identifier shown in II.4. Any other comments, stray lines/characters, are ignored.

## II.1. Absorber Name

usage:  
ABS\_NAME <value>

ex.  
ABS\_NAME 3/4"-Al

Description: This keyword identifier is used to specify the name of the absorber used in the simulation. The <value> is a "string" C data type (a string of characters). The string case is unimportant, but the name needs to be all one word (underscores or hyphens may help to do this). This keyword identifier and value are one of the three that are absolutely necessary.

## II.2. Absorber Material

usage:  
ABS\_MAT <value>

ex.  
ABS\_MAT Al

ex.  
ABS\_MAT Ge

ex.  
ABS\_MAT B

ex.  
ABS\_MAT Li

ex.  
ABS\_MAT Be

ex.  
ABS\_MAT Polyethylene

Description: This keyword identifier is used to specify the material of the absorber used in the simulation. Currently there are only six available materials for use as an absorber. These are elemental aluminum, germanium, boron, lithium, beryllium, and polyethylene. All allowed uses are shown in the examples above. The <value> is a "string" C data type (a string of

characters). The string value is case sensitive and must be entered as shown in the examples above. This keyword identifier and value are one of the three that are absolutely necessary.

### II.3. Absorber Thickness

usage:  
ABS\_THICKNESS <value>

ex.  
ABS\_THICKNESS 2.0

Description: This keyword identifier is used to specify the thickness of the absorber (in centimeters) used in the simulation. The <value> is a "float" C data type (a floating point number). This keyword identifier and value are one of the three that are absolutely necessary.

### II.4. Absorber File Comments

usage:  
ABS\_COMMENT <value>

ex.  
ABS\_COMMENT this is a comment haha

Description: This keyword identifier is used to specify that it is an absorber comment line. This comment is stored in an array of strings and is reported in KMESS output.

## III. FUTURE ADDITIONS

Some of the future additions to this file format could be to include support for the following features:

- "units" as an additional <value> after floating point values
- multiple absorbing materials
- multiple absorbing thickness
- simple geometric absorber shapes
- additional absorbing materials
- mesh absorber specification
- an absorber surrounding source

### A.1.3 KMESS Cross-section File (KCF) README

#### KMESS CROSS-SECTION FILE FORMAT DESCRIPTION (.KCF)

Kevin R. Jackman  
Los Alamos National Laboratory  
05/09/2007

##### i. PREFACE ON UNITS AND PHOTON "CROSS-SECTIONS"

It should be mentioned here that I use the word "cross-section" very loosely in this README. It SHOULD be used in this case to imply the linear, narrow-beam energy-dependent photon absorption coefficient ( $\mu$  in commonly used Greek symbols). That has units of  $\text{cm}^{-1}$ , and thus strictly speaking is a "cross-section". However, in photon attenuation calculations, the "cross-section" is commonly reported in tables as the MASS interaction coefficient ( $\mu/\rho$  in commonly used Greek symbols) that is in units of  $(\text{cm}^2/\text{g})$ . To convert between the two, one needs only the density ( $\rho$ ) of the material in  $(\text{g}/\text{cm}^3)$ . The source of the "cross-sections" used in KMESS comes from NIST. See the NIST X-COM Photon Cross-section page:

<http://physics.nist.gov/PhysRefData/Xcom/Text/XCOM.html>

NIST reports their data as mass interaction coefficients, in units of  $(\text{cm}^2/\text{g})$ . In order to make it easier to create new material "cross-section" files, I designed the KCF file format to accept the NIST data as is (in their units), and have the person creating the KCF file just specify the density of the material. Therefore, all calculations to convert the mass interaction coefficients into "cross-sections" are just handled in KMESS.

##### I. INTRODUCTION

This file contains the primary description on how to create a cross-section file (.KCF) for use with KMESS (Kevin's Mesh Efficiency Simulator Software). Most common uses of the KMESS code will not require creation of new cross-section files. However, this README was developed along-side the code to allow future developers of the code to be more familiar with what I've done. This file also contains a brief description on how to add additional elements to the allowed materials for absorbers. Adding additional materials to the list of available detector materials can be accomplished in a similar way. The primary information contained in a KMESS cross-section file is the density of the material, and then a point wise table of energy and photon

mass interaction coefficients (henceforth called  $\mu$  for the Greek symbols commonly used to represent that value). See section i above if you don't follow what I mean. The mass interaction coefficients ( $\mu$ ) used should be the total minus coherent scattering. The reasons behind excluding coherent scattering are beyond the scope of this README. However, an explanation can be found in the following journal article:

L. Moens et al., Nuclear Instruments & Methods, Vol. 187 (1981) pgs 451-472.

The format for a KMESS cross-section file follows a keyword-value format. This allows one to be able to tell what is contained within the file simply by looking at it in a text file viewer. The files should be written such that they are white space (spaces or tabs) delimited. It should be mentioned that the C routine written to read in the file only cares that it finds the keyword identifier followed by white space followed by values that are delimited by white space up until the end of the line. The current file reading routine can only handle 200 characters per line. However, this can be easily increased in the "kmess.h" file. For help doing that, see the comments contained in that file. The keyword identifiers and values needed to make a successful absorber file are described below as well as the units that are expected for such values. No more than 1000 energy- $\mu$  point pairs are allowed either. The keyword identifier can be no longer than 30 characters. These both can also be easily adjusted in the kmess source files.

## II. KEYWORD IDENTIFIERS, THEIR ASSOCIATED VALUES, AND DESCRIPTIONS

The following is a complete list of the currently recognized keyword identifiers contained in a KMESS cross-section file, followed by a brief description of each. The order of the keyword identifiers in the file is unimportant. However, the minimum keyword identifiers and values necessary for specifying a new material with a KMESS cross-section file are a material name, a density for that material (in  $\text{g}/\text{cm}^3$ ), and at least one pair of energy (in MeV) /  $\mu$  (in  $\text{cm}^2/\text{g}$ ) points (see descriptions of identifiers II.1 through II.3 below). Future additions to KMESS may be to include a "unit" value after the density, energies, and  $\mu$  values so that the input is more flexible with respect to the system of units allowed. Comments are kept if and only if they are specified with the keyword identifier shown in II.4. Any other comments, stray lines/characters, are ignored.

### II.1. Material Name



usage:  
MAT\_NAME <value>

ex.  
MAT\_NAME Al

ex.  
MAT\_NAME Air

Description: This keyword identifier is used to specify the name of the material to be added to KMESS. The name should be something representative of the material, like its elemental symbol, or a description like "Air" (see the examples above). The <value> is a "string" C data type (a string of characters). The string case is unimportant, but the name needs to be all one word (underscores or hyphens may help to do this). This keyword identifier and value are one of the three that are absolutely necessary.

## II.2. Material Density

usage:  
MAT\_DENSITY <value>

ex.  
MAT\_DENSITY 5.323

Description: This keyword identifier is used to specify the density of the material to be used by KMESS in units of grams per centimeter<sup>3</sup> (g/cm<sup>3</sup>). The <value> is a "float" C data type (a floating point number). This keyword identifier and value are one of the three that are absolutely necessary.

## II.3. Material's Energy Dependent Mass Interaction Coefficients (MuOverRho)

usage:  
MAT\_ENERGY\_MUOVERRHO <value> <value>

ex.  
MAT\_ENERGY\_MUOVERRHO 4.000E-03 2.92E+00

Description: This keyword identifier is used to specify that the two values following it are an energy-MuOverRho point pair that describes the total mass interaction coefficient (MuOverRho) minus coherent scattering of the material at that given energy to be used by KMESS. The energy should be quoted in units of Mega electron Volts (MeV), and MuOverRho in units of

centimeters<sup>2</sup> per gram (cm<sup>2</sup>/g). The <value> is a "float" C data type (a floating point number). Exponential formatting is allowed as well. This keyword identifier and value are one of the three that are absolutely necessary.

#### II.4. Cross-section File Comments

usage:  
MAT\_COMMENT <value>

ex.  
MAT\_COMMENT this is a comment haha

Description: This keyword identifier is used to specify that it is a material cross-section comment line. This comment is stored in an array of strings and is NOT reported in any KMESS output.

#### III. FUTURE ADDITIONS

Some of the future additions to this file format could be to include support for the following features:

- "units" as an additional <value> after floating point values
- other material properties?

#### IV. HOWTO ADD A NEW MATERIAL IN KMESS

A new material can be fairly easily interfaced into KMESS. That was the point right? First, the material needs a "cross-section" file. Lastly, one needs to edit the KMESS source code in the proper place to add it as an available material.

To create the cross file, one only needs to have the proper keyword identifiers and values as described in section II above. As an example let's say I wanted to create a new material of elemental Magnesium. In the cross-section file I would put something like:

```
MAT_NAME Mg
MAT_DENSITY 1.738
MAT_ENERGY_MUOVERRHO 1.000E-03 9.20E+02
...(other energy-MuOverRho points here)...
MAT_ENERGY_MUOVERRHO 1.000E+05 3.05E-02
```

Lets, step back. How did I get the energy-MuOverRho data you ask? Here's how I do it (though you could hand copy from a book somewhere but why?). Go to the NIST X-COM Photon Cross-section page:

<http://physics.nist.gov/PhysRefData/Xcom/Text/XCOM.html>

Then, do a database search for the material you are interested in. One thing that is neat about the NIST website, is that you can specify a mixture and it will calculate the cross-section for you. That saves a lot of time trying to do it on your own. Also, it allows you to specify the energy range, so you can tone it down from 10000 MeV if you'd like.

Once you've found the material, you should see a table, you can select a little check box next to the mass interaction coefficients you want. You want total minus coherent scattering. Then, choose some identifier (say space) and click the Download Data button. Copy these data points into separate columns in a spreadsheet. Add a column with the identifier MAT\_ENERGY\_MUOVERRHO in front of all the data points. Save this file as a text file, and rename to <whatever you want>.kcf. Then, you only have to add the MAT\_NAME and MAT\_DENSITY keyword identifiers and values and ...bingo, you're done.

Now, changing the KMESS code to recognize your new material is fairly easy too. Say you wanted to add this new material as a new kind of absorber. Find the cross-section read file section in the source code. Add your material to be available by entering in a few lines of code (to read in the correct .kcf file just like the others). Then, find the part of the code that reads in the ABS\_MAT keyword identifier. Add some code there (just like the others), recompile, build, and you're done. A similar process can be repeated to change the available materials for any other keyword identifier from other types of files too.

#### **A.1.4 KMESS Detector File (KDF) README**

##### KMESS DETECTOR FILE FORMAT DESCRIPTION (.KDF)

Kevin R. Jackman  
Los Alamos National Laboratory  
05/07/2007

## I. INTRODUCTION

This file contains the primary description on how to create a detector file (.KDF) for use with KMESS (Kevin's Mesh Efficiency Simulator Software). It should be mentioned that the terms "crystal" and "detector" are used loosely here, but refer to the actual germanium crystal and everything inside the detector end cap respectively.

The format for a KMESS detector file follows a keyword-value format. This allows one to be able to tell what is contained within the file simply by looking at it in a text file viewer. The files should be written such that they are white space (spaces or tabs) delimited. It should be mentioned that the C routine written to read in the file only cares that it finds the keyword identifier followed by white space followed by values that are delimited by white space up until the end of the line. The current file reading routine can only handle 200 characters per line. However, this can be easily increased in the "kmess.h" file. For help doing that, see the comments contained in that file. The keyword identifiers and values needed to make a successful detector file are described below as well as the units that are expected for such values. The keyword identifier can be no longer than 30 characters. This can be easily adjusted in the kmess source files.

## II. KEYWORD IDENTIFIERS, THEIR ASSOCIATED VALUES, AND DESCRIPTIONS

The following is a complete list of the currently recognized keyword identifiers contained in a KMESS detector file, followed by a brief description of each. The order of the keyword identifiers in the file is unimportant. However, the minimum keyword identifiers and values necessary for specifying a detector in a KMESS detector file are the detector name, detector type, coaxial configuration, detector diameter, and detector length (see descriptions of keyword identifiers II.1 through II.5 below). Future additions to KMESS may be to include a "unit" value after all of the numerical values, so that the input is more flexible in respect to the system of units allowed. Comments are kept if and only if they are specified with the keyword identifier shown in II.16. Any other comments, stray lines/characters, are ignored.

### II.1. Detector Name

usage:  
DET\_NAME <value>

ex.  
DET\_NAME 76

ex.

DET\_NAME Cow

Description: This keyword identifier is used to specify the name of the germanium detector to be simulated. In LANL use, it should be the counter number. The <value> is a "string" C data type (a string of characters). The string case is unimportant, but the name needs to be all one word. This keyword identifier and value are one of the five that are absolutely necessary.

## II.2. Detector Type

usage:

DET\_TYPE <value>

ex.

DET\_TYPE P

ex.

DET\_TYPE n

Description: This keyword identifier is used to specify the type of germanium detector to be simulated. Simply put, it is whether the detector is a p-type or an n-type. It is important because it determines whether the outer contact of the crystal is assumed to be ion-implanted boron (as in an n-type) or diffused lithium (as in a p-type). It also determines whether the inner contact of the crystal is assumed to be ion-implanted boron (as in an p-type) or diffused lithium (as in a n-type). There are currently only two allowed values for this keyword identifier (P or N). Both uses are listed in the examples above. The <value> is a "char" C data type (a single character). The character can be either upper or lower case. This keyword identifier and value are one of the five that are absolutely necessary.

## II.3. Detector Coaxial Configuration

usage:

DET\_COAXTYPE <value>

ex.

DET\_COAXTYPE TRUE

ex.

## DET\_COAXTYPE closed-ended

Description: This keyword identifier is used to specify the coaxial configuration of the germanium crystal to be simulated. There are currently only two allowed types for the value of this keyword identifier (true or closed-ended). Both uses are listed in the examples above. A "true" coaxial detector has a hole in the crystal that goes all the way through it. A "closed-ended" coaxial detector has a crystal that goes partially through it. Consult any book on germanium detectors, if you still are unclear about what this means (ex. Glenn F. Knoll's "Radiation Detection and Measurement"). Future additions to KMESS may be to include well and planar detectors here. But for now, there are only two available. The <value> is a "string" C data type (a string of characters). The string needs to be either all upper case or all lower case. This keyword identifier and value are one of the five that are absolutely necessary.

## II.4. Detector Diameter

usage:

```
DET_DIAMETER <value>
```

ex.

```
DET_DIAMETER 59.8
```

Description: This keyword identifier is used to specify the diameter of the detector (in millimeters) to be simulated. This is the diameter quoted on a typical germanium detector specification sheet. More precisely, it is the diameter of the germanium crystal. The <value> is a "float" C data type (a floating point number). This keyword identifier and value are one of the five that are absolutely necessary.

## II.5. Detector Length

usage:

```
DET_LENGTH <value>
```

ex.

```
DET_LENGTH 59.6
```

Description: This keyword identifier is used to specify the length of the detector (in millimeters) to be simulated. This is the length quoted on a typical germanium detector specification sheet. More precisely, it is the length of the germanium crystal. The <value> is a "float" C data type (a

floating point number). This keyword identifier and value are one of the five that are absolutely necessary.

## II.6. Detector Outer Contact Layer Thickness (Dead Layer)

usage:

```
DET_OUTERCONTACT <value>
```

ex.

```
DET_OUTERCONTACT 700.0
```

Description: This keyword identifier is used to specify the thickness of the outer contact layer (in micrometers) of the detector crystal to be simulated. This is the absorbing layer (or so-called dead layer) quoted on a typical germanium detector specification sheet. More precisely, it is the thickness of inactive material between the inner-most extent of the outer contact layer and the physical outer surface of the crystal on the top and sides of the germanium crystal. The dead layer is assumed to be uniform, even though this has been proven to be only a fair assumption. Future additions to KMESS may include separate specifications for top and side dead layers and possibly a point wise table of thicknesses. The <value> is a "float" C data type (a floating point number). This keyword identifier and value are not necessary, but they are highly recommended for accurate simulations. If a value is not specified, a dead layer of 700 micrometers is assumed for p-type detectors and 0.3 micrometers for n-type detectors. The material composition of this layer is dependent upon the DET\_TYPE specified above (see section II.2 for more details).

## II.7. Detector Inner Contact Layer Thickness

usage:

```
DET_INNERCONTACT <value>
```

ex.

```
DET_INNERCONTACT 0.3
```

Description: This keyword identifier is used to specify the thickness of the inner contact layer (in micrometers) surrounding the coaxial hole in the detector crystal to be simulated. The inner contact layer thickness is rarely quoted on germanium detector specification sheets. It is the thickness of inactive material between the inner-most extent of the inner contact layer surrounding the crystal coaxial hole and the physical edge of the crystal surface within the coaxial hole. The inner contact is assumed to be uniform,

even though this may be only a fair assumption. Future additions to KMESS may include separate specifications for top and side inner contact thicknesses and possibly a point wise table of thicknesses. The <value> is a "float" C data type (a floating point number). This keyword identifier and value are not necessary, but they are highly recommended for accurate simulations. If a value is not specified, an inner contact of 0.3 micrometers is assumed for p-type detectors and 700 micrometers for n-type detectors. The material composition of this layer is dependent upon the DET\_TYPE specified above (see section II.2 for more details).

## II.8. Detector Coaxial Hole Diameter

usage:

DET\_HOLEDIAMETER <value>

ex.

DET\_HOLEDIAMETER 10.0

Description: This keyword identifier is used to specify the diameter of the coaxial hole (in millimeters) in the detector crystal to be simulated. The hole diameter is rarely quoted on germanium detector specification sheets, and usually must be obtained from the detector manufacturer. The <value> is a "float" C data type (a floating point number). This keyword identifier and value are not necessary, but they are highly recommended for accurate simulations. If they are not specified, a hole diameter of 10.0 millimeters is assumed.

## II.9. Detector Coaxial Hole Depth

usage:

DET\_HOLEDEPTH <value>

ex.

DET\_HOLEDEPTH 46.4

Description: This keyword identifier is used to specify the depth of the coaxial hole (in millimeters) in the detector crystal to be simulated. The hole depth is rarely quoted on germanium detector specification sheets, and usually must be obtained from the detector manufacturer. The "depth" is the distance from the bottom of the crystal to the top of the coaxial hole. The <value> is a "float" C data type (a floating point number). This keyword identifier and value are not necessary, but they are highly recommended for accurate simulations. If they are not specified, a hole depth of 3/4 of the



detector length (as specified with the DET\_LENGTH keyword identifier as above) is assumed for closed-ended coax configurations. The hole depth defaults to the entire detector length for true coax configurations. The coax configuration is specified with the DET\_COAXTYPE keyword identifier listed above.

## II.10. End Cap Window Material

usage:

```
DET_ENDCAPWINDOWMAT <value>
```

ex.

```
DET_ENDCAPWINDOWMAT Be
```

ex.

```
DET_ENDCAPWINDOWMAT Al
```

Description: This keyword identifier is used to specify the material of the end cap window above of the detector crystal to be simulated. This end cap material will be used in any gamma-ray attenuation calculations where the gamma-ray enters the end cap from above the end cap window surface. There are only two currently available values for the end cap material (Al or Be). The <value> is a "string" C data type (a string of characters). The string value is case sensitive and must be entered as shown in the examples above. This keyword identifier and value are not necessary, but they are highly recommended for accurate simulations. If no material is specified, an aluminum (Al) end cap window material is assumed.

## II.11. End Cap Window Thickness

usage:

```
DET_ENDCAPWINDOWTHICK <value>
```

ex.

```
DET_ENDCAPWINDOWTHICK 1.0
```

Description: This keyword identifier is used to specify the thickness of the end cap window (in millimeters) above of the detector crystal to be simulated. The <value> is a "float" C data type (a floating point number). This keyword identifier and value are not necessary, but they are highly recommended for accurate simulations. If no thickness is specified, an end cap window thickness of 1.0 millimeters is assumed.

## II.12. End Cap To Crystal Gap Thickness

usage:

```
DET_ENDCAPTOCRYSTALGAP <value>
```

ex.

```
DET_ENDCAPTOCRYSTALGAP 4.0
```

Description: This keyword identifier is used to specify the distance of the end cap window (in millimeters) from the top of the detector crystal to be simulated. This is the "end cap to detector" or "distance from window" that is quoted on a typical germanium detector specification sheet. More precisely, it is the distance from the top of the crystal to the inner bottom of the end cap window. Loosely defined, it is the thickness of empty space between the crystal and the end cap window. The <value> is a "float" C data type (a floating point number). This keyword identifier and value are not necessary, but they are highly recommended for accurate simulations. If no thickness is specified, an end cap to crystal gap of 4.0 millimeters is assumed.

## II.13. End Cap Side Wall Material

usage:

```
DET_ENDCAPWALLMAT <value>
```

ex.

```
DET_ENDCAPWALLMAT Al
```

Description: This keyword identifier is used to specify the material of the end cap wall on the side of the detector crystal to be simulated. This end cap material will be used in any gamma-ray attenuation calculations where the gamma-ray enters the end cap from the side of the end cap surface. There is only one currently available value for the end cap material (Al). The <value> is a "string" C data type (a string of characters). The string value is case sensitive and must be entered as shown in the example above. This keyword identifier and value are not necessary, but they are highly recommended for accurate simulations. If no material is specified, an aluminum (Al) end cap wall is assumed. Future additions to KMESS may be to allow for different end cap side wall materials.

## II.14. End Cap Side Wall Thickness

usage:

DET\_ENDCAPWALLTHICK <value>

ex.

DET\_ENDCAPWALLTHICK 1.0

Description: This keyword identifier is used to specify the thickness of the side wall of end cap (in millimeters) on the side of the detector to be simulated. The <value> is a "float" C data type (a floating point number). This keyword identifier and value are not necessary, but they are highly recommended for accurate simulations. If no thickness is specified, an end cap wall thickness of 1.0 millimeters is assumed.

## II.15. Mounting Cup Wall Thickness

usage:

DET\_MOUNTCUPWALLTHICK <value>

ex.

DET\_MOUNTCUPWALLTHICK 1.0

Description: This keyword identifier is used to specify the thickness of the side wall of the aluminum mounting cup (in millimeters) that holds the detector crystal to be simulated. The <value> is a "float" C data type (a floating point number). This keyword identifier and value are not necessary, but they are highly recommended for accurate simulations. If no thickness is specified, a mounting cup wall thickness of 1.0 millimeters is assumed.

## II.16. Detector File Comments

usage:

DET\_COMMENT <value>

ex.

DET\_COMMENT this is a comment haha

Description: This keyword identifier is used to specify that it is a detector comment line. This comment is stored in an array of strings and is reported in KMESS output.

## III. FUTURE ADDITIONS

Some of the future additions to this file format could be to include support for the following features:

- "units" as an additional <value> after floating point values
- multi-string detector name support
- well and planar detectors
- non-uniform inner and outer contact layers
- different end cap window and wall materials
- different mounting cup wall materials
- include mylar shields and insulators around the crystal
- include bulletization parameters for the crystal and coaxial hole

### **A.1.5 KMESS Reference File (KRF) REAME**

#### KMESS REFERENCE CURVE FILE FORMAT DESCRIPTION (.KRF)

Kevin R. Jackman  
Los Alamos National Laboratory  
05/09/2007

#### I. INTRODUCTION

This file contains the primary description on how to create a reference curve file (.KRF) for use with KMESS (Kevin's Mesh Efficiency Simulator Software). The primary information contained in a KMESS reference curve file is a set of energy-efficiency-uncertainty point pairs. The file format of this type of file differs dramatically from all the other standard KMESS file formats. This is because KMESS was originally designed to interface with the efficiency calibrations tool available on Russ Gritzo's NGWeb. One of the resulting files from performing an efficiency calibration is called a VAX file. This is a legacy format that is used to supply our VAX run gamma-ray analysis software with energy-efficiency-uncertainty point pairs. Because of this, it made sense to just allow KMESS to read VAX files. This means that if the VAX computers ever go away, and we hope they do, the KRF file format should probably be re-designed to follow formats that more closely resemble the other standard KMESS file formats. This README is less useful than the others because I only supply an example VAX file and tell you it has to be exactly like that. This reference curve will be used by KMESS to convert the effective solid angle of some desired counting geometry into a full-energy peak efficiency for that desired counting geometry. It will also use the uncertainties, if supplied, in the propagation of uncertainty. The

number of allowed reference curve points is 5000, but this can be easily changed in the KMESS source code.

## II. EXAMPLE VAX FILE

The following is an example of the VAX efficiency file format. The first line is just a comment line. The data points are energy (in keV) in the first column, the absolute full-energy peak efficiency in the second, and the efficiency uncertainty (in percent) in the third. The -1.00 is just a signal for the end of file. It has to be exactly in this format, same number of columns, number of decimal places, exponent sign, exponent format, etc...

```
0760210 1.00000 NGW78 07-26-06
 59.50 9.905e-4 8.841e-1
 88.04 2.941e-3 7.665e-1
122.06 3.775e-3 4.979e-1
165.86 3.667e-3 5.237e-1
279.20 2.515e-3 4.939e-1
391.70 1.808e-3 4.394e-1
661.70 1.084e-3 4.880e-1
898.00 8.158e-4 4.595e-1
1173.20 6.431e-4 4.234e-1
1332.50 5.767e-4 4.562e-1
1836.10 4.447e-4 8.300e-1
-1.00 0.000e+00
```

## III. FUTURE ADDITIONS

Some of the future additions to this file format could be to include support for the following features:

- re-design entire format

### **A.1.6 KMESS Source File (KSF) README**

#### KMESS SOURCE FILE FORMAT DESCRIPTION (.KSF)

Kevin R. Jackman  
Los Alamos National Laboratory

05/08/2007

## I. INTRODUCTION

This file contains the primary description on how to create a source file (.KSF) for use with KMESS (Kevin's Mesh Efficiency Simulator Software). The primary information contained in a KMESS source file are the (x,y,z) coordinates (in units of centimeters) of a source mesh. These source coordinates should be prepared before hand, in whatever meshing software is your flavor, to be in a Cartesian coordinate system with the origin set on the primary detector axis at the center of the outer surface of the germanium detector end cap window. Furthermore, the positive z-axis should point along the primary detector axis, away from the detector.

The format for a KMESS source file follows a keyword-value format. This allows one to be able to tell what is contained within the file simply by looking at it in a text file viewer. The files should be written such that they are white space (spaces or tabs) delimited. It should be mentioned that the C routine written to read in the file only cares that it finds the keyword identifier followed by white space followed by values that are delimited by white space up until the end of the line. The current file reading routine can only handle 200 characters per line. However, this can be easily increased in the "kmess.h" file. For help doing that, see the comments contained in that file. The keyword identifiers and values needed to make a successful source file are described below as well as the units that are expected for such values. The keyword identifier can be no longer than 30 characters. This can be easily adjusted in the kmess source files.

## II. KEYWORD IDENTIFIERS, THEIR ASSOCIATED VALUES, AND DESCRIPTIONS

The following is a complete list of the currently recognized keyword identifiers contained in a KMESS source file, followed by a brief description of each. The order of the keyword identifiers in the file is unimportant. However, the minimum keyword identifiers and values necessary for specifying a source in a KMESS source file are a source name and at least one set of (x,y,z) source coordinates, in units of centimeters (see descriptions of identifiers II.1 and II.2 below). Future additions to KMESS may be to include a "unit" value after all of the (x,y,z) source coordinate values, so that the input is more flexible with respect to the system of units allowed. Comments are kept if and only if they are specified with the keyword identifier shown in II.5. Any other comments, stray lines/characters, are ignored.

## II.1. Source Name

usage:

SRC\_NAME <value>

ex.

SRC\_NAME QCY48

ex.

SRC\_NAME 9991-06-123

Description: This keyword identifier is used to specify the name of the source used in the simulation. In LANL use, it should be the name of the solution or the SHOT-JUG-MASS. The <value> is a "string" C data type (a string of characters). The string case is unimportant, but the name needs to be all one word (underscores or hyphens may help to do this). This keyword identifier and value are one of the two that are absolutely necessary.

## II.2. Source (X,Y,Z) Coordinates without Weights

usage:

SRC\_XYZ <value> <value> <value>

ex.

SRC\_XYZ 1.03 -2.5001 5.43529

Description: This keyword identifier is used to specify the (x,y,z) coordinates of the source mesh. These can be either vertices or the centers of the source mesh, because really only the mesh order is critical for good simulations of complex source descriptions. The three values are entered as <X-coordinate> <Y-coordinate> <Z-coordinate> and must be in that specific order. Negative values are allowed, but negative Z coordinate values imply that the source is below the plane of the detector end cap window. KMESS will thus adjust the calculations accordingly. Read section I above if you are confused by what this means. The <value> arguments are "float" C data types (floating point numbers). Exponential formatting of the coordinates is allowed. This keyword identifier and value are one of the two that are absolutely necessary. KMESS currently allows only up to 5000 source coordinates to be entered. However, this number is arbitrary and can easily be changed to accommodate more source coordinates in the "kmess.h" file. This identifier is used when weighting the source points is not desired. This makes all of the weights used in averaging default to 1.0. This identifier should not be mixed with that in section II.3.

### II.3. Source (X,Y,Z) Coordinates with Weights

usage:

```
SRC_XYZW <value> <value> <value> <value>
```

ex.

```
SRC_XYZW 1.03 -2.5001 5.43529 0.89
```

Description: This keyword identifier is used to specify the (x,y,z) coordinates of the source mesh. These can be either vertices or the centers of the source mesh, because really only the mesh order is critical for good simulations of complex source descriptions. The three values are entered as <X-coordinate> <Y-coordinate> <Z-coordinate> and must be in that specific order. Negative values are allowed, but negative Z coordinate values imply that the source is below the plane of the detector end cap window. KMESS will thus adjust the calculations accordingly. Read section I above if you are confused by what this means. The <value> arguments are "float" C data types (floating point numbers). Exponential formatting of the coordinates is allowed. This keyword identifier and value are one of the two that are absolutely necessary. KMESS currently allows only up to 5000 source coordinates to be entered. However, this number is arbitrary and can easily be changed to accommodate more source coordinates in the "kmess.h" file. This identifier is used when weighting the source points is desired. This weights of all the points should be normalized such that they add up to equal 1.0. These weights will control the contribution to the average of each point. This identifier should not be mixed with that in section II.2.

### II.4. Source Material

usage:

```
SRC_MAT <value>
```

ex.

```
SRC_MAT 4MHCl
```

Description: This keyword identifier is used to specify the material of the source used in the simulation. Currently there is only one available material for use as a source. This is a 4M HCl solution. All allowed uses are shown in the examples above. The <value> is a "string" C data type (a string of characters). The string value is case sensitive and must be entered as shown in the example above. This keyword identifier is optional,



but not specifying a source material will make KMESS not correct for source self attenuation.

## II.5. Source Type

usage:  
SRC\_TYPE <value>

ex.  
SRC\_TYPE 2

Description: This keyword identifier is used to specify the "type" of the source to be simulated. This "type" is one of the many types that are commonly used at LANL and refer to a specific source geometry. This keyword identifier and value are not necessary, and have no affect on how KMESS runs. They are included merely for book keeping purposes. If not specified, a source type of 666 is assumed. The <value> argument is an "int" C data type (integer number).

## II.6. Source Shelf Height

usage:  
SRC\_SHELFHEIGHT <value>

ex.  
SRC\_SHELFHEIGHT 12

Description: This keyword identifier is used to specify the counting system's shelf height that the source is placed at for the simulation. This corresponds to a specific counting geometry for LANL counting systems. However, the shelf height number itself is just a reference number, and the actual source-to-detector distances are recorded in tables elsewhere. This keyword identifier and value are not necessary, and have no affect on how KMESS runs. They are included merely for book keeping purposes. If not specified, a shelf height of 666 is assumed. The <value> argument is an "int" C data type (integer number).

## II.7. Source File Comments

usage:  
SRC\_COMMENT <value>

ex.

SRC\_COMMENT this is a comment haha

Description: This keyword identifier is used to specify that it is a source comment line. This comment is stored in an array of strings and is reported in KMESS output.

### III. FUTURE ADDITIONS

Some of the future additions to this file format could be to include support for the following features:

- "units" in (x,y,z) source coordinate values
- multi-string source name support
- different (x,y,z) source coordinate orders ex. (z,y,x)
- cylindrical (r,theta,z) source coordinates
- spherical (r,theta,phi) source coordinates
- a translation factor for X, Y, Z source translations
- a rotation factor for X, Y, Z source rotations

## A.2 PROCEDURE FOR USING KMESS TO DETERMINE EFFICIENCIES

This part of the Appendix describes a systematic procedure for using KMESS to predict the full-energy peak efficiency of a high-purity germanium detector. This section is divided into steps to further simplify the determination process.

### A.2.1 Determination of an Experimental Reference Curve

This step is one of the most important of all of the procedures in using KMESS. This is because any uncertainty in the measured reference curve is directly reflected as an increased uncertainty in the predicted efficiencies. The steps described below serve to help in the determination of a proper source and counting geometry.

First, a careful choice of a reference source should be made. This source should first and foremost have a well-known activity. NIST traceable sources or equivalent are highly encouraged. The source should be chosen such that it has gamma-ray energies in the region that efficiencies are desired. The radionuclides in the source will primarily determine the gamma-ray energy range that is covered. If at all possible, a wide range of gamma-ray energies should be preferred. If the source has a high activity, there may be problems with coincidence summing or dead-time. The source shape, or geometry, should be chosen such that it is as close to the other desired geometry as possible. This serves to help preserve the invariance of the “virtual” peak-to-total ratio.

Second, a desired reference counting geometry should be chosen for the reference curve. This is initially done through selection of the proper type of detector. If very low-energy gamma-rays are desired to be studied, it may be desirable to use an *n*-type detector with a thin end-cap window. Proper shielding, such as lead, may also help to reduce the background in the detector and increase its detection capabilities. The counting geometry should be selected such that coincidence summing effects are minimized. Typically a source-to-detector distance of greater than 10 cm is enough to reduce these effects (Knoll, 2000). Reducing summing effects serves to primarily reduce the uncertainties that will arise later in the net peak area determination. However, depending upon the activity of the source, reducing summing effects may be abandoned in favor of determining the curve in a shorter amount of time. This is done by simply placing the source close to the detector. If at all possible, the source should be counted with its center coinciding with the primary detector axis. This is done in order to increase reproducibility of the counting geometry, and typically yields a greater overall counting efficiency than other counting geometries. The counting length should then be selected to be long enough so that the statistical in the spectra are optimized.

Last, a careful analysis of the resulting spectrum and the determination of the full-energy peak efficiencies are performed. This is first and foremost done by using good gamma-ray analysis software. The software should be able to fit peaks and determine their net peak areas, even for multiplets and strong low-energy tails. Corrections for coincidence summing should also be performed here if necessary. Dead-time corrections may also need to be applied. The isotopes in the source should be corrected for decay from the zero-time to the count time. The full-energy peak efficiencies at the energies of interest should then be determined. These energy-efficiency pairs may then be fit using some semi-empirical function or equivalent in order to evaluate the efficiencies at other energies. The result of these careful measurements will result in a good full-energy peak reference curve.

### **A.2.2 Setting up and Running KMESS**

At this point, the reference geometry should have been chosen and its efficiency curve determined. The next step is to prepare the necessary files for use with KMESS. If an absorber was used in the measurements, KMESS will need an absorber file. Both the reference and desired source geometries should be meshed into a large collection of points using some standard meshing software. These points should be the  $(x, y, z)$  coordinates of the points relative to the center of the detector end-cap top. Then a KMESS source file is generated using either the conversion tools or the proper keyword-value identifiers. If source self-attenuation is desired to be corrected for, the proper choice of source material should be specified in the source file. A detector file should be made that includes as much of the detector data as can be obtained from the detector manufacturer. This detector file will include things like the crystal diameter, length, and dead-layer. A KMESS reference curve file should also be created that contains the

energy-efficiency point pairs of the experimentally determined reference curve. Finally, the desired run method of KMESS should be selected from the list of available choices shown in Appendix A.1.1. Descriptions of the allowed KMESS file formats are also shown in Appendix A.1. Then KMESS should be executed and the predicted efficiencies will be output.

## References

- Baba, H., Yokoyama, A., Sakuraba, Y., Nitani, N., Saito, T., and Baba, S., "Systematic Treatment of the Photopeak Efficiency," *Nuclear Instruments and Methods in Physics Research A*, Volume 309 (1991) 236-247.
- Berger, M.J., Hubbell, J.H., Seltzer, S.M., Chang, J., Coursey, J.S., Sukumar, R., and Zucker, D.S., "X-COM: Photon Cross-sections Database," *NIST X-COM web-site*. <<http://physics.nist.gov/PhysRefData/Xcom/Text/XCOM.html>>, 2007.
- Bossus, D.A.W., Swagten, J.J.J.M., Kleinjans, P.A.M., "Experience with a Factory-calibrated HPGe Detector," *Nuclear Instruments and Methods in Physics Research A*, Volume 564 (2006) 650-654.
- Camp, D.C. and Van Lehn, A.L., "Finite Solid-Angle Corrections for Ge(Li) Detectors," *Nuclear Instruments and Methods*, Volume 76 (1969) 192-240.
- Carchon, R., Van Camp, E., Knuyt, G., Van De Vyver, R., Devos, J., and Ferdinande, H., "A General Solid Angle Calculation By a Monte Carlo Method," *Nuclear Instruments and Methods*, Volume 128 (1975) 195-199.
- Cejnar, F., and Kovar, I., "Experimental and Calculated Photopeak Efficiency Values for Well-type NaI(Tl) Detectors," *International Journal of Applied Radiation and Isotopes*, Volume 31 (1980) 79-84.
- Chatani, H., "Systemization of Efficiency Correction for Gamma-ray Disk Sources with Semiconductor Detectors," *Nuclear Instruments and Methods in Physics Research A*, Volume 425 (1999) 291-301.
- Cline, J.E., "A Technique of Gamma-ray Detector Absolute Efficiency Calibration for Extended Sources," *Proceedings American Nuclear Society Topical Conference Computers Activation Analysis Gamma-ray Spectroscopy*, Mayaguez, Puerto Rico, April 30-May 4, 1978, CONF-780421, (published 1979), 185-196.
- Cornejo Diaz, N. and Perez Sanchez, D., "Validacion Teorica y Experimental del Codigo DETEFF para el Calculo de la Eficiencia de Sistemas Gamma Espectrometricos," *IV Congreso Regional IRPA sobre Seguridad Radiologica y Nuclear*. Habana, Cuba, 19-23 Octubre, 1998, Tomo 2, Seccion 6, pg. 99.

- Crisler, D.F., Jarmer, J.J., and Eldridge, H.B., "A Method for Absolute Calibration of Ge(Li) Detectors Using Effective Interaction Depth," *Nuclear Instruments and Methods*, Volume 94, Number 2 (1971) 285-288.
- Debertin, K. and Helmer, R., Gamma- and X-ray Spectrometry with Semiconductor Detectors. Amsterdam: North-Holland, 1988.
- Ewa, I.O.B., Bodizs, D., Czifrus, Sz., and Molnar, Zs., "Monte Carlo Determination of Full Energy Peak Efficiency for HPGe Detector," *Applied Radiation and Isotopes*, Volume 55 (2001) 103-108.
- Gilmore, G., and Hemmingway, J., Practical Gamma-ray Spectrometry, Chichester: John Wiley & Sons, 1995.
- Graudynya, L.Ya., Kalnyn, Yu.R.H., and Pelekis, L.L., "Total Efficiency of Gamma-ray Detection by Germanium Semiconductor Detectors," *Journal of Radioanalytic Chemistry*, Volume 9 (1971) 341-386.
- Griffiths, R., "Calculated Total Efficiencies of Coaxial Ge(Li) Detectors," *Nuclear Instruments and Methods*, Volume 91 (1971) 377-379.
- Grosjean, C.C., "On the Absolute Detection Efficiency of a Cylindrical Scintillation Phosphor in the Case of an Extended Plane Gamma-ray Source," *Nuclear Instruments and Methods*, Volume 17 (1962) 289-309.
- Gunnink, R. and Niday, J.B., "Computerized Quantitative Analysis by Gamma-ray Spectrometry. Vol. 1. Description of the GAMANAL Program," *USAEC Report*, UCRL-51061, Volume 1, University of California, NTIS (1972).
- Gunnink, R., "New Method for Calibrating a Ge Detector by Using Only Zero to Four Efficiency Points," *Nuclear Instruments and Methods in Physics Research A*, Volume 299 (1990) 372-376.
- Gunnink, R. and Prindle, A.L., "Nonconventional Methods for Accurately Calibrating Germanium Detectors," *Journal of Radioanalytical and Nuclear Chemistry*, Volume 160, Number 2, (1992) 305-314.
- Heath, R.L., "Scintillation Spectrometry Gamma-ray Spectrum Catalogue," 1<sup>st</sup> Ed., *USAEC Research and Development Report*, IDO-16408 (1957).
- Heath, R.L., "Scintillation Spectrometry Gamma-ray Spectrum Catalogue," 2<sup>nd</sup> Ed., *USAEC Research and Development Report*, IDO-16880 (1964).

- Hurtado, S., Garcia-Leon, M., and Garcia-Tenorio, R., "GEANT4 Code for Simulation of A Germanium Gamma-ray Detector and its Application to Efficiency Calibration," *Nuclear Instruments and Methods in Physics Research A*, Volume 518 (2004) 764-774.
- Jackman, K.R., "Monte Carlo Simulations of Germanium Detector Efficiency Curves," Masters Thesis, University of Texas at Austin, Austin, TX 2004.
- Jiang, S.H., Liang, J.H., Chou, J.T., Lin, U.T., and Yeh, W.W., "A Hybrid Method for Calculating Absolute Peak Efficiency of Germanium Detectors," *Nuclear Instruments and Methods in Physics Research A*, Volume 413 (1998) 281-292.
- Jovanovic, S., Dlabac, A., Mihaljevic, N., and Vukotic, P., "ANGLE: A PC-code for Semiconductor Detector Efficiency Calculations," *Journal of Radioanalytical and Nuclear Chemistry*, Volume 218, Number 1 (1997) 13-20.
- Kahn, B. and Lyon, W.S., "Scintillation Spectrometer in Radiochemical Analysis," *Nucleonics*, Volume 11, No. 11, (November 1953) 61-63.
- Kaplanis, S.N., "Efficiency Variations of Cylindrical Detectors for Non-Axial Point-Sources," *International Journal of Applied Radiation and Isotopes*, Volume 29 (1978) 543-544.
- Karamanis, D., "Efficiency Simulation of HPGe and Si(Li) Detectors in Gamma- and X-ray Spectroscopy," *Nuclear Instruments and Methods in Physics Research A*, Volume 505 (2003) 282-285.
- Keyser, R., "Resolution and Sensitivity as a Function of Energy and Incident Geometry for Germanium Detectors," *IRRMA Meeting*, Bologna, Italy, June 2002.
- Kippen, R.M., "The GEANT Low Energy Compton Scattering (G4LECS) Package for use in Simulating Advanced Compton Telescopes," *New Astronomy Reviews*, Volume 48 (2004) 221-225.
- Knoll, G., Radiation Detection and Measurement, 3<sup>rd</sup> Edition. New Jersey: John Wiley & Sons, 2000.
- Kushelevski, A.P., and Alfassi, Z.B., "Off Center Gamma-ray Detection Efficiencies of Cylindrical Single Open Ended (SOE) Ge(Li) Detectors," *Nuclear Instruments and Methods in Physics*, Volume 131 (1975) 93-95.
- Lippert, Jorgen., "Detector-Efficiency Calculation Based on Point-Source Measurement," *International Journal of Applied Radiation and Isotopes*, Volume 34, Number 8 (1983) 1097-1103.



- Moens, L., De Donder, J., Lin, Xi-lei, De Corte, F., De Wispelaere, A., Simonits, A., and Hoste, J., "Calculation of the Absolute Peak Efficiency of Gamma-ray Detectors for Different Counting Geometries," *Nuclear Instruments and Methods*, Volume 187 (1981) 451-472.
- Noguchi, M., Takeda, K., and Higuchi, H., "Semi-empirical Gamma-ray Peak Efficiency Determination Including Self-absorption Correction Based on Numerical Integration," *International Journal of Applied Radiation and Isotopes*, Volume 32 (1981) 17-22.
- Notea, A., "The Ge(Li) Spectrometer as a Point Detector," *Nuclear Instruments and Methods*, Volume 91, Number 3 (1971) 513-515.
- Press, W.H., Flannery, B.P., Teukolsky, S.A., and Vetterling, W.T., Numerical Recipes in C: The Art of Scientific Computing, Cambridge: Cambridge University Press, 1990.
- Rodenas, J., Pascual, A. Zarza, I., Serradell, V., Ortiz, J., and Ballesteros, L., "Analysis of the Influence of Germanium Dead Layer on Detector Calibration Simulation for Environmental Radioactive Samples Using the Monte Carlo Method," *Nuclear Instruments and Methods in Physics Research A*, Volume 496 (2003) 390-399.
- Rohlf, J., Modern Physics from  $\alpha$  to Zo, New York: John Wiley & Sons, 1994.
- Shultis, J.K., and Faw, R.E., Radiation Shielding, 2<sup>nd</sup> Edition. Illinois: American Nuclear Society, 2000.
- Simpson, R.E., Introductory Electronics for Scientists and Engineers, 2<sup>nd</sup> Edition. Massachusetts: Allyn and Bacon, 1987.
- Sima, O., Arnold, D., and Dovlete, C., "GESPECOR: A Versatile Tool in Gamma-ray Spectrometry," *Journal of Radioanalytical and Nuclear Chemistry*, Volume 248, Number 2 (2001) 359-364.
- Ugletveit, F., Sinkko, K., Aaltonen, H., and Feldt, W., "A Simple Method for Efficiency Calibration of Germanium Detectors," *Regional Conference of the International Radiation Protection Association (IRPA) on the Radioecology of Natural and Artificial Radionuclides*, September 10-14, 1989: Visby Sweden, Publisher: Koeln: Germany, 474-479.
- Vargas, M.J., Timon, A.F., Diaz, N.C., and Sanchez, D.P., "Influence of the Geometrical Characteristics of an HPGe Detector on its Efficiency," *Journal of Radioanalytical and Nuclear Chemistry*, Volume 253, Number 3 (2002) 439-443.

- Vegors, S.H., Marsden, L.L., and Heath, R.L., "Calculated Efficiencies of Cylindrical Radiation Detectors," *USAEC Research and Development Report*, IDO-16370 (1958).
- Venkataraman, R., Bronson, F., Atrashkevich, V., Field, M., and Young, B.M., "Improved Detector Response Characterization Method in ISOCS and LabSOCS," *Journal of Radioanalytical and Nuclear Chemistry*, Volume 264, Number 1 (2005) 213-219.
- Venkataraman, R., Croft, S., and Russ, W.S., "Calculation of Peak-to-Total Ratios for High Purity Germanium Detectors Using Monte-Carlo Modeling," *Journal of Radioanalytical and Nuclear Chemistry*, Volume 264 (2005) 183-191.
- Vidmar, T., "EFFTRAN-A Monte Carlo efficiency transfer code for gamma-ray spectrometry," *Nuclear Instruments and Methods in Physics Research A*. Volume 550 (2005) 603-608.
- Vukotic, P., Mihaljevic, N. Jovanovic, S., Dapcevic, S., and Boreli, F., "On the Applicability of the Effective Solid Angle Concept in Activity Determination of Large Cylindrical Sources," *Journal of Radioanalytical and Nuclear Chemistry*, Volume 218 (1997) 21-26.
- Wielopolski, L., "The Monte Carlo Calculation of the Average Solid Angle Subtended by a Right Circular Cylinder From Distributed Sources," *Nuclear Instruments and Methods*, Volume 143 (1977) 577-581.
- Yucel, H., Atif Cetiner, M., and Demirel, H., "Dependence of Photon Interaction Depth on Linear Attenuation Coefficient in High Pure Germanium Detectors," *Applied Radiation and Isotopes*, Volume 47 (1996) 535-541.

## **Vita**

Kevin Richard Jackman was born on July 9, 1980 in Bryan, Texas to Dr. John Alfred Jackman and Linda Josephine Jackman (maiden name, Hamilton). Kevin was raised in College Station, Texas and attended A&M Consolidated High School where he graduated in the top 5% of his class in 1998. Kevin then attended The University of North Texas for one year. He quickly transferred to The University of Texas at Austin, where he obtained a Bachelor of Science in Physics and a Bachelor of Arts in Astronomy in 2003. He immediately began attending graduate school at The University of Texas at Austin in Mechanical Engineering. He received his Master of Science in Engineering in late 2004. He has since been researching for the Chemistry division and Nuclear and Radiochemistry group at Los Alamos National Laboratory. As of the writing of this dissertation, he resides in Santa Fe, NM.

Permanent address: 3934 Oriole Court, College Station, TX 77845

This dissertation was typed by Kevin Richard Jackman.